Positron Annihilation Studies of Model Fe-Cr Alloys and Ferritic/Martensitic Steels

by

HARI BABU SATA
(Enrollment No: PHYS02200704021)

Indira Gandhi Center for Atomic Research, Kalpakkam

A thesis submitted to the
Board of Studies in Physical Sciences
In partial fulfillment of requirements
For the degree of

DOCTOR OF PHILOSOPHY

of

HOMI BHABHA NATIONAL INSTITUTE

FEBRUARY, 2013

Homi Bhabha National Institute

Recommendations of the Viva Voce Board

As members of the Viva Voce Board, we certify that we have read the dissertation prepared by **Hari Babu Sata** entitled **"Positron Annihilation Studies of Model Fe-Cr Alloys and Ferritic/Martensitic Steels"** and recommend that it may be accepted as fulfilling the dissertation requirement for the Degree of Doctor of Philosophy.

____Date:
Chairman – C. S. Sundar

____Date:
Convener/Guide – G. Amarendra

____Date:
Member – T. Jayakumar

____Date:
Member – S. Saroja

Final approval and acceptance of this dissertation is contingent upon the candidate's submission of the final copies of the dissertation to HBNI.

Date:
Place:

CERTIFICATE

I hereby certify that I have read this dissertation prepared under my direction and recommend that it may be accepted as fulfilling the dissertation requirement.

Date:

Place: **(G. Amarendra)**

Thesis Supervisor

STATEMENT BY AUTHOR

This dissertation has been submitted in partial fulfillment of requirements for an advanced degree at Homi Bhabha National Institute (HBNI) and is deposited in the library to be made available to borrowers under rules of the HBNI.

Brief quotations from this dissertation are allowable without special permission, provided that accurate acknowledgement of source is made. Requests for permission for extended quotation from or reproduction of this manuscript in whole or in part may be granted by the Competent Authority of HBNI when in his or her judgment the proposed use of the material is in the interests of scholarship. In all other instances, however, permission must be obtained from the author.

(Hari Babu Sata)
Ph.D Candidate

DECLARATION

I, hereby declare that the investigation presented in the thesis has been carried out by me. The work is original and has not been submitted earlier as a whole or in part for a degree / diploma at this or any other Institution / University.

(Hari Babu Sata)

Ph.D Candidate

To My Mother

Late Smt. Venkata Ramana Sata

ACKNOWLEDGEMENTS

I express my gratitude to my research supervisor Dr. G. Amarendra, Head, Materials Physics Division for his guidance and for providing freedom to do quite a lot of mistakes. He extended his helping hand as and when it is necessary to make me feel comfortable. I also thank him for his useful suggestions and careful but painstaking efforts in correcting this thesis.

I thank my doctoral committee members, Dr. C. S. Sundar, Director, Materials Science Group for useful discussions and suggestions to present the results better. I learnt from him how to look at things from a different perspective. I thank Dr. T. Jayakumar, Director, Metallurgy & Materials Group for useful discussions and encouragement. I enjoyed talking to him which is refreshing and positive, always. I thank Dr. S. Saroja, Head, Microscopy & Thermo-physical Property Division for discussions and useful criticism. I am indebted for her concern regarding timely completion of my thesis.

I thank Dr. Baldev Raj, former Director, IGCAR for encouragement and for providing freedom to take a project that interests me. I am grateful to his commitment to provide best facilities for students. I also thank Shri S. C. Chetal, former Director, IGCAR for the support. I am grateful to Dr. P. R. Vasudeva Rao, Director, IGCAR for his support and encouragement. I thank Shri M. C. Valsakumar, former Head, Materials Physics Division for motivation and his keen interest in studies of Fe-Cr model alloys. I thank Dr. M. Sai Baba, Associate Director, Resource Management Group for his support in choosing the project and for providing best facilities at hostel.

I thank Dr. R. Rajaraman for introducing me to positron annihilation spectroscopy and for useful discussions. I thank Shri Varghese Anto for useful discussions and writing Matlab program for extracting CDB data. I thank Dr. S. Abhaya for thoroughly reading the manuscript and for AES measurements. I thank Dr. R. Govindaraj, for discussions and help in preparation of binary alloys. I thank Dr. G. Venugopal Rao, Shri. V. Ragunathan, Ms. J. Parimala, Ms. Premila, Dr. Sairam, Shri. Herojit and Shri. Renjith for help at various stages of my work. I thank Dr. Mythili, Dr. N. P. Lalla (UGC-DAE-CSR, Indore), Dr. S. Amrithapandian, Dr. Arup Dasgupta, Dr. Gopal Bahlerao for TEM measurements and useful discussions. I thank Ms. S. Kalavathi for XRD measurements and useful discussions. I thank Ms. O. Annalakshmi for careful reading of the manuscript and encouragement. I thank Ms. Radhika and Dr. Shamima Hussain for SEM measurements and useful discussions. I thank Dr. K. V. Rajkumar and Dr. Anish Kumar for ultrasonic measurements and discussions. I thank Dr. C. Sudha, Dr. K. S. Viswanathan, Dr. V. Chandramouli, Ms. T. N. Prasanthi and Dr. Trinadha Raja for chemical analysis. I thank Dr. P. Ch. Sahu and Shri L. M. Sundaram for help in arc-melting of Fe-Cr binary alloy. I thank Dr. Ana Alamo, CEA, France for providing EUROFER97 steel samples. I thank Dr. K. Laha for providing Mod. 9Cr-1Mo steel samples. I thank Dr. Dr. Shaju K. Albert for providing plain 9Cr-1Mo steel samples. I thank Shri Ravikirana, Ms. Madhusmita, Ms. Preeti Mahajan (UGC-DAE-CSR, Indore) and Ms. Sumita for help in TEM sample preparation. I thank Dr. Feby Jose, Dr. Baban P D, Ms. Shabana, Shri Pradyumna, Shri Manmath for help at various stages of sample preparation. I thank all the STIP students of batches 2009 to 2012 for their interaction and Shri V. Sridhar and Dr. H. K. Sahu for giving me an opportunity to interact with the students.

I thank DAE, India for the fellowship during August-2007 and July-2012. I thank my friend Bala Krishna for financial assistance beyond August-2012.

I thank all my friends and well wishers at IGCAR and UGC-DAE-CSR, Indore. In particular, I thank Krishna, Girish, Lakshmi Prasanna, Raghu, Ridhi, Ranjana, Sulata, Aga Shahee, Dhirendra, Shilpam, Sree Rama Murthy, Mahendra, Sagar, Balu, Subbarao, Karthick, Rajendra, Bishnu, Prasana, Karunakar, Kalpataru, Saravana, Deepak, Dharshan, Bhairavi, Pradeep Ch, Krishnan, Manas, Sudahnshu, Pradeep, Shashwat, Subhra, Rajini, Nithila, Kuheli, Maneesha, Debasmita Das, Sudipta, Soumee, Pravati, Rahul, Sorb, Kamali, Anbu, Kalyan, Shrihari, Jagadeesh, Avinash, Bhubathi, Vishnu, Laksmoji, Mariyappa, Srinivas, Ilayaraja, Vipin, Santhosh, Raghavendra, Thangam, Shravnthi, Sumathi, Usha, Molly and Debasmita for their support and care at various parts of this period.

I thank my brother Ravi and sister Gayatri for being buffers for me all the time. I thank my parents Prabhakara Rao, Sambasiva Rao, Mangamma for their support.

Hari Babu Sata

CONTENTS

5. Cr Segregation in Fe-Cr Alloys 96-133

6. Summary and Future Scope 134-137

Chapter - 1

Introduction

1.0 PREAMBLE

This thesis presents and discusses results and the scope of positron annihilation spectroscopy relating to microstructural changes in two different ferritic/martensitic steels i.e. EUROFER97, Mod. 9Cr-1Mo and their model Fe-Cr binary alloys. Results of other corroborating techniques will be presented so as to obtain comprehensive information. This chapter briefs about ferritic/martensitic steels, their typical microstructure and interest in studying the dependence of positron annihilation characteristics on microstructure. Some of the open problems regarding Cr precipitation in Fe-rich portion of Fe-Cr phase diagram and the effect of this precipitation on mechanical properties of ferritic/martensitic steels will be highlighted.

1.1 SCOPE OF FERRITIC/MARTENSITIC STEELS

Ferritic/martensitic steels are the prospective candidate materials as structural components of first wall and breeding blanket in fusion reactors [1] and in future fast reactors for clad, ducts and fuel sub-assembly applications, which envisage high operating temperatures and intensive high energy neutron irradiation [2]. They are also considered to be a potential structural material for spallation targets of Accelerator Driven Systems (ADS), which envisage intensive neutron fluxes produced by proton beams operating at GeV energy with MW range power. They are potential candidates due to their high swelling resistance, impressive thermal conductivity and flexibility to attain reduced activation by appropriate choice of alloying elements and their compositions.

1.2 COMPARISON TO AUSTENITIC STEELS

For ferritic steels, having relatively high thermal conductivity, thermal stress factor is about three times larger than austenitic steels below 600 K (Figure-1.1). For a given heat flux of 0.6 MW/m^2 (ITER conditions) and thermal stress factors for respective steels, the possible maximum wall thickness is estimated to be 2 and 10 mm for austenitic and ferritic steels, respectively. The minimum wall thickness estimated for Steady State Tokamak Reactor (SSTR) is 5 mm for flux of 1 MW/m^2 (References 12-14 of [3]). As an example, in ferritic steels a significant decrease in propagation length of thermal fatigue crack found as compared to SS316 [4]. Hence, from thermal stress point of view ferritic steels are advantageous over austenitic steels.

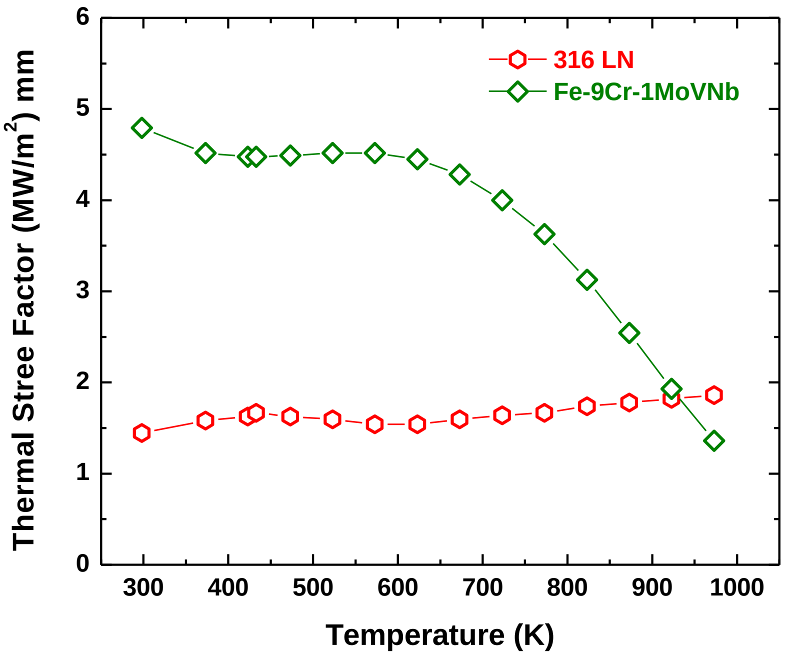

Figure-1.1: Thermal stress factor comparison between a typical ferritic steel (Fe-9Cr-1MoVNb) and an austenitic steel (316(N)). Below 600 K the ferritic steel shows thermal stress factor three time larger than 316L(N) [5].

Figure-1.2 shows relative change in volume fraction of austenitic and ferritic steels as a function of fluence. As compared to austenitic (SS316) steels, ferritic steels have higher resistance to swelling caused by irradiation. Void swelling in ferritic steels is around 1%, while for the austenitic stainless steels it is 10-28% for the same fluence of neutron irradiation (18 x 10^{22} n/cm^2, E > 0.1 MeV) at 693 K [6]. Ferritic steels are expected to swell only 1% per 100 dpa against 1% per 10 dpa in austenitic stainless steel [7]. Less than 2% swelling observed in modified 9Cr-1Mo steel due to 200 dpa neutron irradiation, in the range of maximum swelling temperatures i.e. 673 – 693 K [8]. In the case of F82H (Fe-8Cr-2W-0.2V-0.04Ta-0.1C) steel, the yield strength increases after irradiation at temperatures below 650 K with maximum value for irradiation around 523 K. However, about 8% total elongation is observed even at 523 K indicating the suitable nature of ferritic steels for irradiation conditions [3].

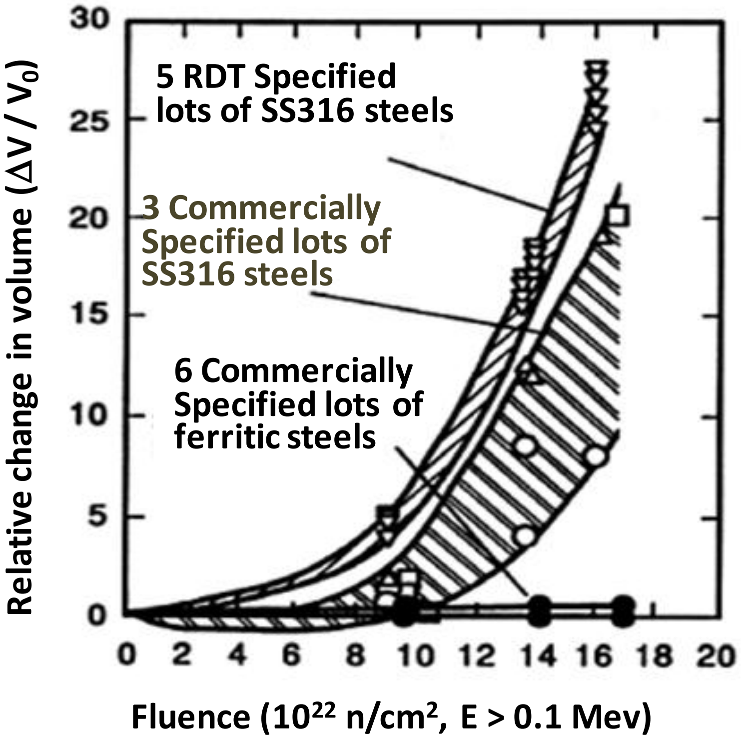

Figure-1.2: Comparison of neutron irradiation behaviour of ferritic steels with austenitic steels. One order less swelling observed in ferritic steels as compared to austenitic steels [9].

Even though, ferritic steels are highly resistant to swelling caused by neutron irradiation, He irradiation is expected to cause increase in swelling in high He/dpa ratio conditions envisaged in fusion reactors [10]. Nevertheless, it should be noticed that even for He irradiation ferritic steels exhibit less swelling as compared to austenitic steels.

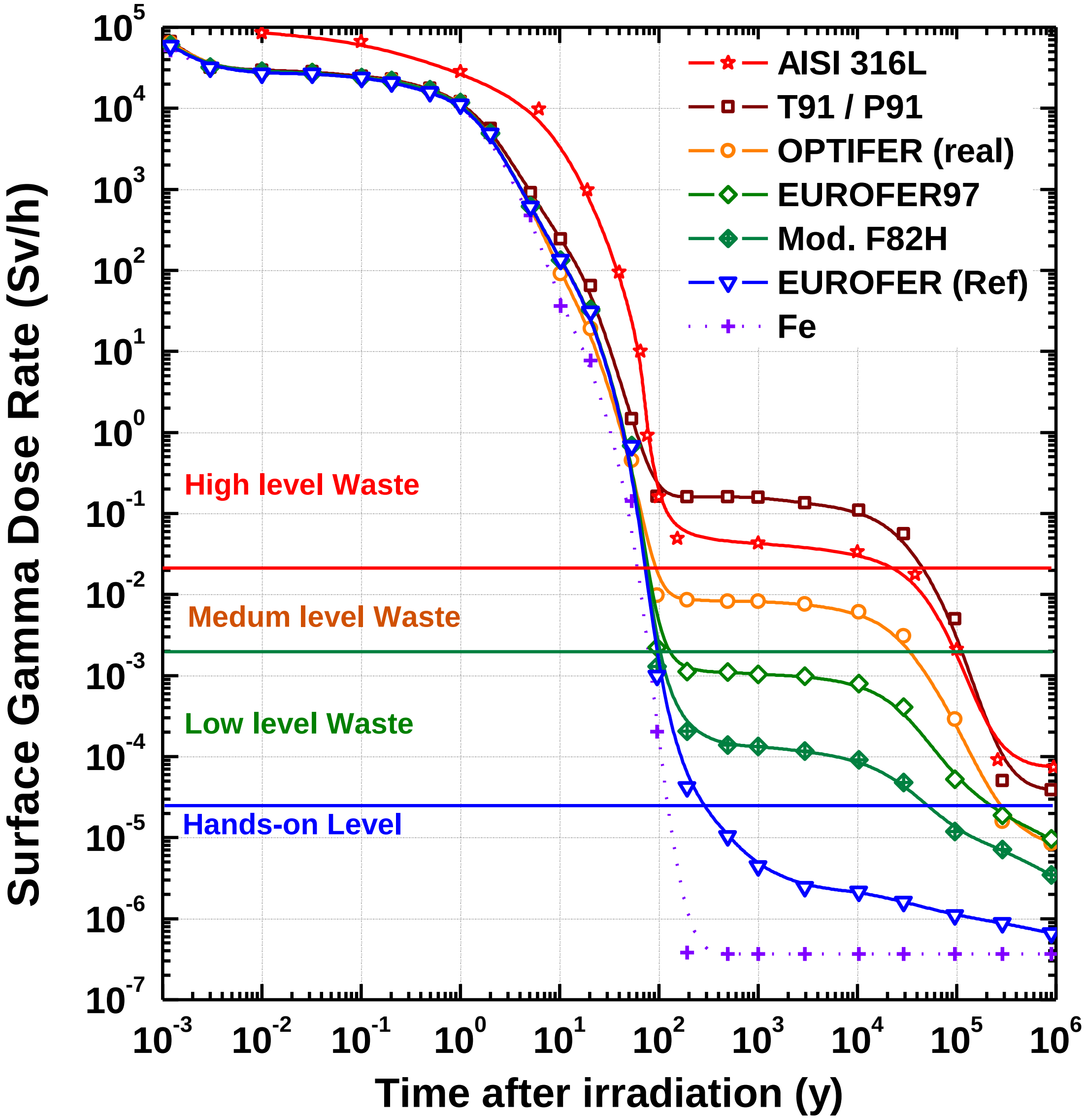

Figure-1.3: Comparison of radiation dose of different activated materials as a function of time after irradiation [11]. Compared to SS316 and T91/P91, reduced activation steels reach recyclable limits early in time by two orders.

Upon neutron irradiation, the transmutation reactions of some of the alloying elements (such as Mo, Nb, Ni, Cu and N) produce radioactive isotopes of higher lifetime. In SS316, Mo and Ni contribute to produce isotopes of Nb and Co, respectively [12]. These isotopes hold responsibility for maximum activity for longer periods. It may be noted that Ni is a major alloying element in SS316. In the case of ferritic steels, some of the alloying elements could be replaced or reduced to attain lower activation. Tungsten stabilized ferritic/martensitic steels seem to have appropriate properties for fusion applications, which will retain upto an irradiation dose as high as 200 dpa [13]. EUROFER97 steel is one such reduced activation steel, which is derived from modified 9Cr-1Mo (T91) steel by replacing Mo, Nb with W, Ta, respectively and reducing N [12, 14]. Figure-1.3 shows the comparison of gamma radiation dose rates of SS316, T91 and EUROFER97 steels as a function of time after irradiation [11]. Low dose levels of irradiated EUROFER97 steel, allowable for remote recycling, will be attained in 100 years as against more than 10^4 years in the case of SS316 and modified 9Cr-1Mo steel.

Some of the high Cr (~9 wt%) ferritic steels are found to be having superior ultimate tensile strength and yield strength (Figure-1.4) over a wide range of temperatures, 300-973 K [15]. Figure-1.4 shows the comparison of average stress for rupture, upto 10^5 hours of aging, between a few commercial ferritic steels and 304 stainless steel. The modified 9Cr-1Mo steel found to be having better strength than SS304 below 873 K. Having known this, subsequently developed reduced activation ferritic steels used modified 9Cr-1Mo as reference composition to maintain the superior mechanical properties. A general similarity observed in tensile properties of modified 9Cr-1Mo and EUROFER97, observed at room temperature and at 623 – 723 K in both unirradiated and irradiated (up to 20 dpa) conditions [16]. However, the softening of ferritic steels at higher temperatures is a concern as materials are exposed to higher temperatures in transient conditions (during failure of pumps, uncontrolled withdrawal of control rod etc.) [2].

The stability of as-prepared microstructure will determine the strength of the steel in long term operation. Hence, improvements in ferritic steels are anticipated for stability of microstructure at high temperature irradiation conditions. One of the important contributions to stabilization of microstructure, in ferritic/martensitic steels, is distribution of precipitates along grains, lath boundaries and inside laths.

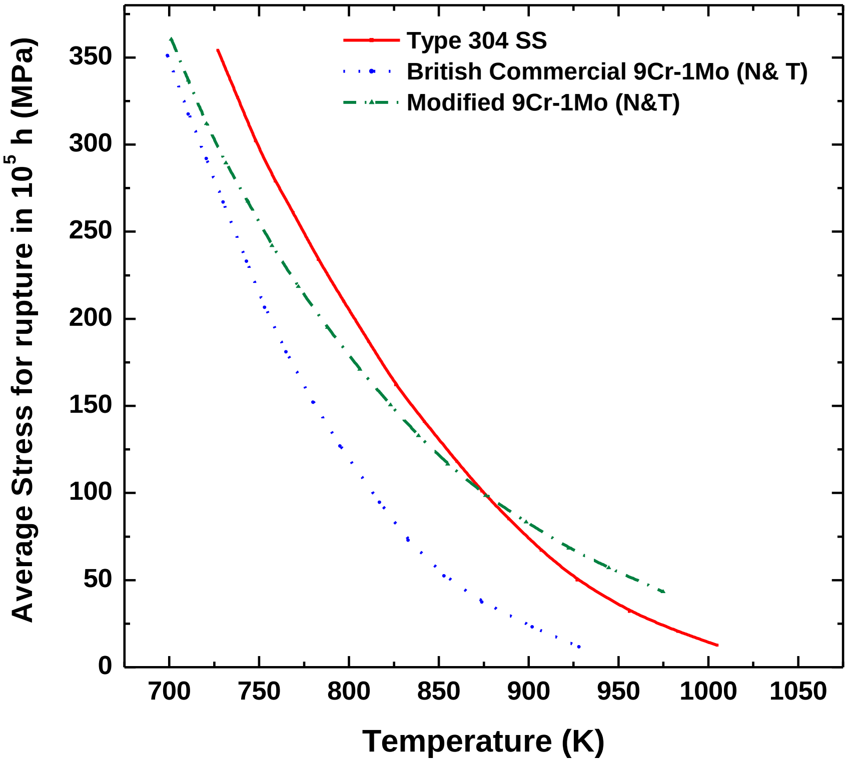

Figure-1.4: Comparison of strengths of ferritic steels with SS304 austenitic steel. Below 873 K, the modified 9Cr-1Mo steel is seen to have higher strength [17].

1.3 IMPORTANCE OF 9% CHROMIUM STEELS

Importance of ferritic steels with Cr concentration around 9%, for irradiation conditions, is a resultant of optimization of strength and its favourable Ductile to Brittle Transition Temperature (DBTT). Relation between creep strength and DBTT with varying

Cr concentration (2-15%) is shown in Figure-1.5, with other elements 2% W and 0.1% C fixed [18, 19]. The creep strength increases first and then decreases as Cr concentration is increased. The low strength of steels with less than 7% Cr is due to greater coarsening of carbides and sub-grains from their initial bainitic structure. Low strength at higher Cr (> 10%) is due to formation of dual phase, martensite and δ-ferrite.

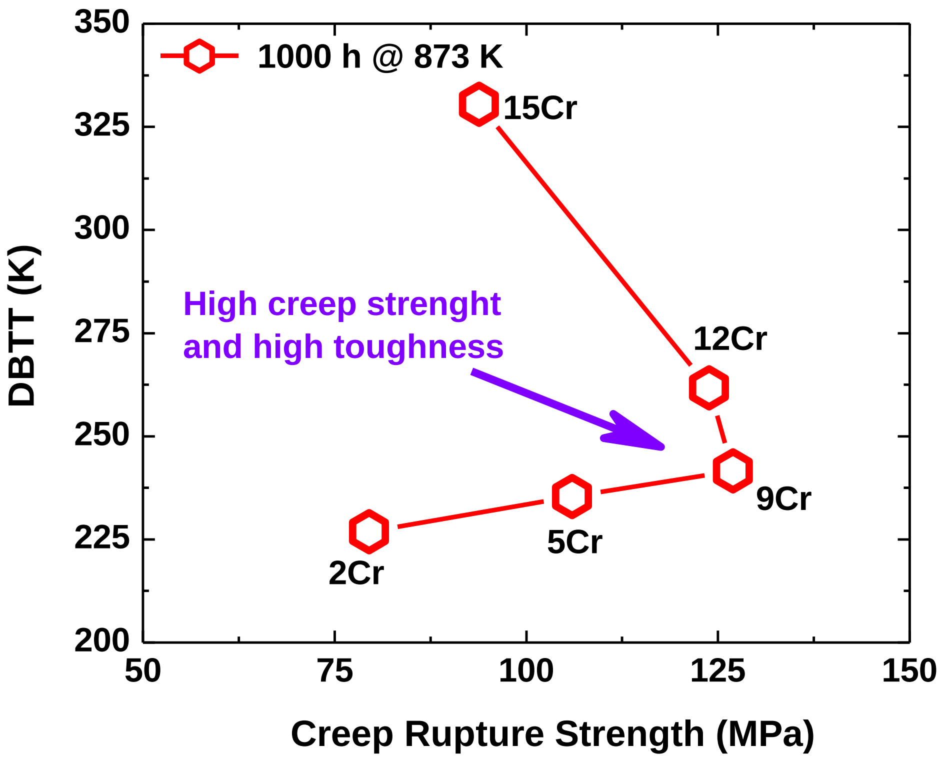

Figure-1.5: Relation between DBTT and creep rupture strength after 1000 h aging at 873 K for (2-15)Cr-2W-0.1C steels [19].

Though it is seen that DBTT is increasing with Cr concentration, upon irradiation there is a shift in DBTT and hence, DBTT of irradiated materials is lowest for 9% Cr steels [20, 21]. The shift in DBTT as a function of Cr concentration is shown in Figure-1.6, for a range of ferritic steels, with minimum value around 9% Cr. It is to be noted that for a given class of steels with similar composition, the minimum DBTT shift is found around 9%. Replacement of Mo and addition of Ta also seems to saturate shift in DBTT with lower fluence, about 1 dpa [21].

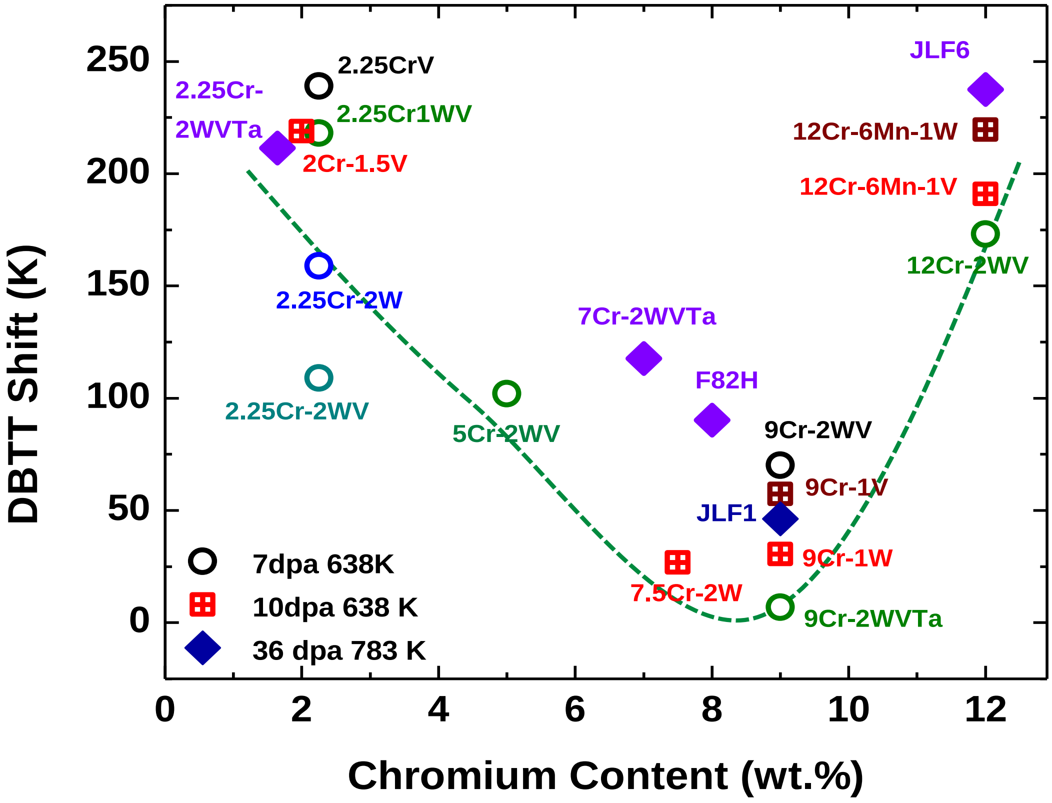

Figure-1.6: Effect of Cr concentration on shift in DBTT upon neutron irradiation in a broad range of ferritic steels. Minimum shift in DBTT seen around 9 wt% Cr [21]. The open symbols are data after 7 dpa and squares are after 10 dpa at 638 K. The diamond symbols correspond to 36 dpa at 783 K. The compositions are mentioned as wt%. If not mentioned with any number Ta and V minor alloying elements.

1.4 MICROSTRUCTURE

In normalized condition, 7-12% Cr steels exhibit body-centered-tetragonal martensitic structure. The normalized samples consist of lath structure within prior-austenite grains. They also contain high number density (~10^{16} m^{-2}) of dislocations within lath matrix and at lath boundaries.

To increase toughness and ductility, normalized martensitic steel needs to be tempered at an appropriate temperature below lower critical temperature. The tempering causes structural change to tempered martensite, a ferritic structure [22] with sub-grains formed from initial laths. The resultant lath/sub-grain width is around of 0.5 ± 0.2 μm [23, 24]. In the process, the number density of dislocations decreases to a range 1-10 x 10^{14} m^{-2} [25, 26, 27], which is still considered higher than undefected pure solid solutions. During tempering, metal carbides and nitrides ($M_{23}C_6$ and MX) precipitate resulting in a ferrite matrix. Here, M refers to metal (generally Cr, W/Mo rich in $M_{23}C_6$ and V/Ta/Nb/Ti rich in MX, depending on alloying elements of the steel [19, 22, 23, 24, 27, 28, 29, 30, 31]) and X refers to C or/and N. It is known that $M_{23}C_6$ precipitates form during tempering above 823 K. Tempering below 823 K also causes formation of M_2C precipitates. However, VC precipitates are not known to form, at least up to 1 h, for tempering below 973 K [32]. $M_{23}C_6$ carbides mainly precipitate on prior-austenite grain boundaries and lath interfaces and their size depend on their location. On prior-austenite grain boundaries, their size is noted to be up to 300 nm and between 25 – 200 nm at lath interfaces [23, 28, 29] while a few precipitates grow inside sub-grains up to a size of 500 nm [28]. The chemical composition is found to be (66 ± 5)% Cr – (30 ± 1)% Fe and also with W and V enrichment [28, 31]. The MX type precipitates form mainly inside laths but considerable number of them also precipitate on lath interfaces [28]. In 9% Cr ferritic steels, the concentration of $M_{23}C_6$ and MX precipitates are found to be of the order of 10^{19} and 10^{18} m^{-3}, respectively [27]. The schematic diagram of microstructure of normalized and tempered 9Cr – (1)Mo/W – (0.10 ± 0.02)C – (0.2)V - (0.10 ± 0.10)Nb/Ta ferritic steels is shown in Figure-1.7. It contains lath substructure within prior-austenite grain. The prior-austenite grain boundaries and lath boundaries are decorated with metal carbide and nitride precipitates ($M_{23}C_6$ and MX) and MX precipitates are also present within the laths.

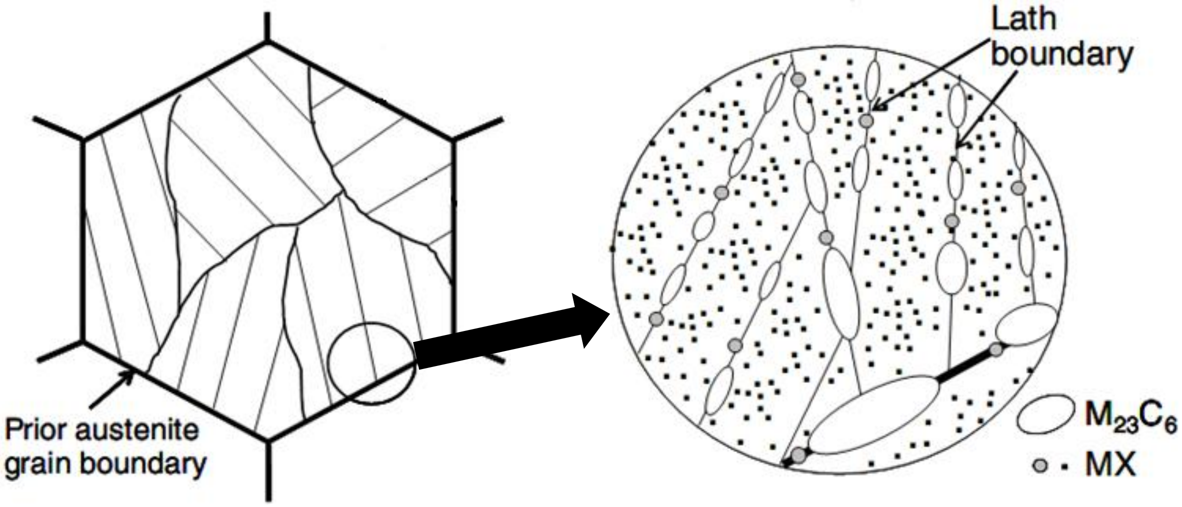

Figure-1.7: Schematic diagram of normalized and tempered 9Cr ferritic/martensitic steel with lath structure and dispersed precipitates [19].

The microstructural factors that affect hardness and strength of ferritic/martensitic steels are (a) solid solution (b) dislocation density (c) lath width and (d) inter-particle spacing [19]. According to Hume-Rothery size effect, solid solution strengthening occurs due to addition of Mo/W and it will be the base strength upon which other strengthening mechanisms superimpose. The contribution from free dislocation density to strengthening is given by [33]

$$\sigma_p = 0.5\, MGb\, (\rho_f)^{1/2} \qquad \text{-------------}\ 1.1$$

Where M is the Taylor factor (=3), G is the shear modulus, b is the magnitude of the Burgers vector and ρ_f is the free dislocation density. It is known that in ferritic steels the effect of dislocations on strengthening is generally small compared to effect of grain size and shape [34]. Further, the contribution from free dislocations is only for a short duration at higher temperatures and with applied stress [35].

Strengthening due to pinning of dislocation by precipitate particles proposed by Orowan mechanism is given by [33]

$$\sigma_{or} = 0.8\,MGb/\lambda \qquad \text{------------- } 1.2$$

Where λ is the mean interparticle spacing.

Strengthening due to lath boundaries is given by [33]

$$\sigma_{sg} = 10\,Gb/\lambda_{sg} \qquad \text{------------- } 1.3$$

Where λ_{sg} is the shortest width of the sub-grains.

Compared to free dislocations and precipitates, lath structural contribution is significantly higher in typical 9Cr ferritic martensitic steels [19]. The proportionality factor in equation 1.3 also indicates the same. This indicates that the strength depends mainly on the stability of lath structure.

Hence, the crucial microstructural modifications, that affect mechanical properties, in 9Cr ferritic/martensitic steels occur mainly by migration of lath boundaries leading to lath coarsening, at high temperatures (>773 K), and the rate of coarsening increases with stress. Irradiation induced defects accelerate the process by enhanced volume diffusion. The grain and sub-grain boundaries in pure metals and solid solution alloys are highly mobile under stress. The movement of these boundaries can absorb excess dislocations from inside the sub-grains causing dynamic recovery process, resulting in softening [36]. However, ferritic steels consists of variety of other phases ($M_{23}C_6$, MX, M_2X, M_6C, M_7C_3, Fe_2(Mo,W) Laves phase, Fe_7W_6 χ-phase) [19] which will influence the strengthening mechanism by dispersion along lath/sub-grain boundaries, grain boundaries and inside sub-grain boundaries. The lath and sub-grain boundaries with high density of dislocations and dispersed precipitates (mainly $M_{23}C_6$, MX) are dominant strengthening contributors for long term usage of tempered martensitic steels. The free dislocations inside sub-grains are pinned by precipitates dispersed inside the laths. Hence, they will retard absorption of dislocations at boundary walls and coarsening of precipitates on boundaries which will further increase the efficiency of dislocation absorption [19]. The chain reaction leads to accelerated creep. Further, formation of Laves phase and χ-phase contribute to reduction of strength by consuming $M_{23}C_6$ precipitates decorated at boundaries. Hence, the stability of dispersed $M_{23}C_6$, MX precipitates is a key factor that keeps the strength of the material for prolonged service conditions. Furthermore, MX precipitates are found to be less coarsening and can contribute significantly to the stability of microstructure. As an example, plain 9Cr-1Mo steels are recommended for operating temperatures of up to 811 K, while V and Nb optimized modified 9Cr-1Mo steels are considered for operating temperature of 866 K.

It was also proposed that the changes in alloying composition, especially carbon, could attain a microstructure where majority of $M_{23}C_6$ precipitates are replaced by MX precipitates. This modification reduces creep rate and increases the time to rupture significantly (nearly an order) at 923 K and 140 MPa. The effect of irradiation, however, was not considered in the study [37].

The above discussion brings out the importance of precipitate distribution to maintain the microstructural integrity during operation. Hence, it is crucial to know the evolution and distribution of precipitates in ferritic/martensitic steels.

1.5 EFFECT OF AGEING ON MICROSTRUCTURE

As it is said, the long term strength of the materials depends on microstructure stability at service conditions. Hence, microstructural stability is a crucial requirement for selection of steels for high temperature and irradiation conditions. The microstructure as well as hardness of modified 9Cr-1Mo steel is stable up to 1000 h and 400 h at 823 K and 923 K, respectively [32]. Along with $M_{23}C_6$ precipitates, VC precipitates are found to be effective in pinning lath/sub-grain boundaries. Unless stated, all the steels mentioned here will be having composition based on modified 9Cr-1Mo, with respect to V, Nb/Ta concentration. Similar study showed the stability of lath microstructure even after aging for 10000 h at 773 - 873 K [38]. However, coarsening of $M_{23}C_6$ and a decrease in hardness was found in the samples aged for 10000 h at 873 K. Laves phase formation is seen along grain boundaries after 5000 h aging for all temperatures (773–873 K) [38].

In the case of 9Cr-W alloys, similar microstructural stability and hence, mechanical properties are observed. For reduced activation steels with concentration of $\leq$ 9wt % Cr and $\leq$ 1 wt% W, the microstructure and mechanical properties remained same after aging at 523 - 823 K up to 5000 - 13500 h [31]. Similarly, EUROFER97 steel showed microstructural stability after aging at 673, 773 and 873 K up to 10000 h. The lath widths are found to be similar before and after aging i.e. 0.5 ± 0.2 µm [23]. The quantity of extracted phases also shows no much variation before and after aging, 2.5 at% and 2.5–2.0 at%, respectively. Occasional occurrence of equiaxial grains were seen for samples aged at 773 and 873 K for 10000 h indicating thermal aged recrystallization. In majority of cases these equiaxial grains are decorated with large $M_{23}C_6$ (350 nm) precipitates at their boundaries and they were containing neither or a few dislocations and precipitates inside the grains. This indicates the boundary migrations due to absence of pinning centres.

For EUROFER97, upon aging for 5000 h at 773 K, there are no significant changes in DBTT values and tensile properties [39]. Similarly, aging at 875 K for 1050 h and at 855 K for 3330 h did not affect tensile properties significantly [40, 41].

However, under the stress the microstructure is seen changing at 873 K in 9Cr-W alloys. Under the stress of 118 MPa, coarsening of laths, by migration of lath boundaries, and coarsening of precipitates ($M_{23}C_6$), by volume diffusion dominated mechanism, is seen by Ostwald ripening [24]. This will destabilize the microstructure. Increase in W concentration reduces the rate of coarsening of these carbides [24]. However, more than 2% leads to segregate of W at grain boundaries and precipitation of Laves phase that engulf carbides, destabilizing microstructure after aging at 823 K for 10000 h [31].

One more notable microstructural change at 773 K and below for ferritic steels containing more than 12 wt% Cr is the formation of Cr rich α'-precipitates [42]. This precipitation is strongly accelerated by irradiation [43]. Irradiation induced α' precipitation is identified in 12 Cr ferritic steel [27]. Further, α' precipitation is seen upon irradiation with mere 8% Cr concentration in Fe-Cr binary alloys [44].

1.6 Fe-Cr BINARY ALLOYS

The equilibrium phase diagram of Fe-Cr binary alloy is shown in Figure-1.8. In this thesis, the focus will be mainly on Fe rich side of phase diagram (< 20% Cr) which is the region of interest for the current study. The salient features are (i) mainly it is a BCC structure below 1119 K. It can be either homogeneous solid solution or with co-existence of Cr rich BCC α'-phase below 785 K, with the later increase with increase in Cr concentration. Above 785 K, tetragonal close-packed structured intermetallic σ phase coexist with BCC phase. However, there is no consensus on the exact temperature for this boundary. (ii) FCC phase for alloys containing Cr concentration below 11.9 at% between temperatures 1119 - 1667 K.

As it is understandable from previous section 1.3, the concentration of Cr plays a major role in the formation of martensitic structure and hence, the strength and lower DBTT by having fine sized lath structure. Cr rich precipitation is found to be one of the very important reasons for embrittlement, particularly after irradiation.

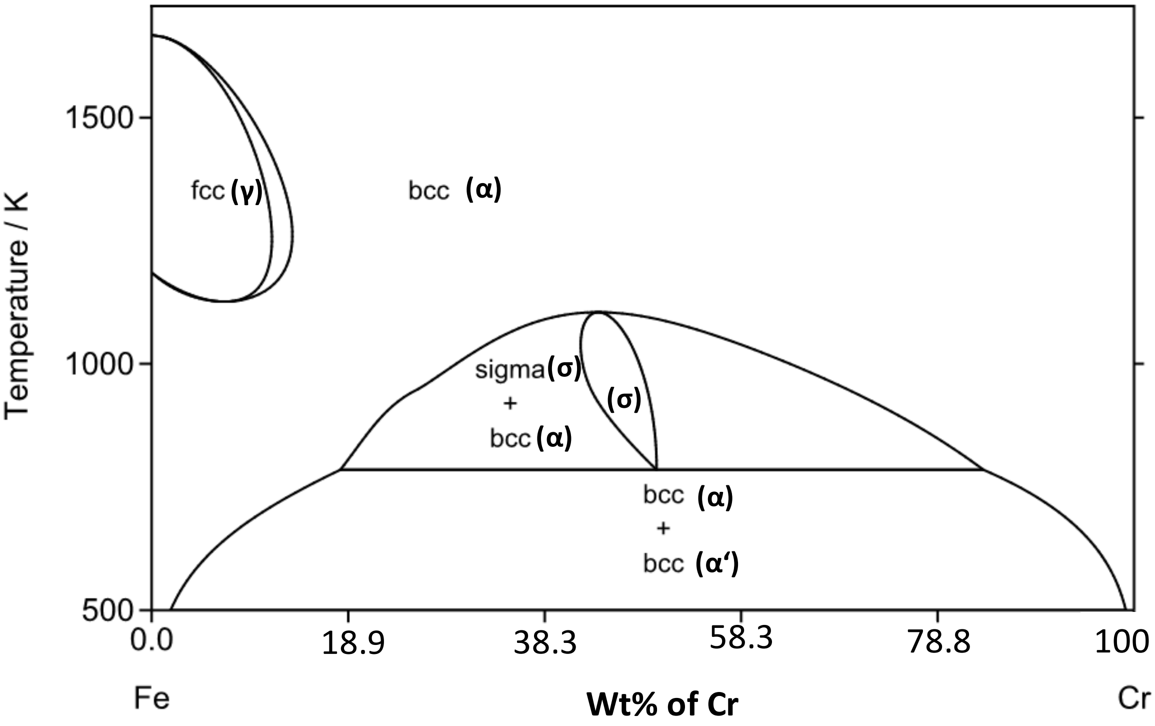

Figure-1.8: Equilibrium phase diagram of Fe-Cr alloy [45, 46]. Some of the phases which are of interest to this work are mentioned as follows. FCC-γ is a high temperature phase for alloys with Cr concentration below 13.45 wt%. For Cr concentration beyond ~10 wt%, α' (Cr rich phase separation from homogeneous Fe-Cr alloy) formation is known. For further high concentration of Cr, σ-phase forms for the temperatures greater than 785 K.

The α' precipitation during thermal aging is known to cause embrittlement in ferritic stainless steels with Cr concentration greater than 12% [42, 47, 48] and Fe-(14, 18)% Cr binary alloys for treatment temperature of 773 K or below [49]. The α' precipitation is known to be accelerated upon irradiation. Despite these observations, all the factors which influence precipitation are not fully understood. The same is the case in understanding of equilibrium phase boundary in Fe-rich side of Fe-Cr phase diagram [46]. Considerable efforts are also being made to obtain reliable interatomic potentials for computational modelling of Fe-Cr system [50].

Earlier resistivity and diffuse neutron scattering studies showed short range ordering in Fe-Cr alloys for Cr content more than 10 at% [51]. Neutron irradiation induced Cr precipitation was observed in Fe-Cr alloys containing >9% Cr [52, 53, 54, 55]. Positron annihilation studies have also showed accelerated phase separation upon electron irradiation followed by isochronal annealing below 700 K for wide range of Cr concentrations (5-20 wt%) [56, 57]. Electron microscopy and Energy dispersive X-ray spectroscopy studies showed clustering of Cr with *insitu* electron irradiation at 873 K for Fe-2.8 at% Cr [58]. Helium implantation causing Cr segregation at grain boundaries was also reported [59]. Metropolis Monte Carlo simulations and positron measurements with electron irradiated conditions showed signatures for Cr clustering [60] and it also supported the study showing tendency to resist the formation of a Cr-vacancy complex [61].

As a whole, the precipitation of Cr depends on the amount of Cr, type of irradiation and irradiation temperature. Except for Ref. [58], which is irradiation at higher temperature (873 K), electron and neutron irradiation showed precipitation for higher Cr alloys (> 9%) only, while low Cr alloys showed Cr precipitation only with ion irradiation, as it can produce irradiation cascades. Contrary to this, simulation work showed tendency for clustering even for pure thermal aging [62, 63, 64], which is not observed experimentally up to now.

Despite extensive observations, the role of dislocations in solute (Cr) segregation was not studied explicitly. It also showed systematic dependence on the structure, being martensitic or equiaxed course grain structure [65]. This thesis brings out the dependence of initial martensitic structure on solute segregation.

1.7 POSITRON TECHNIQUES TO PROBE PRECIPITATION

The selective nature of positrons to vacancy kind of defects prompts their applicability to understand the microstructural changes by studying the associated vacancy defects. The trapping nature of positrons at vacancies due to attractive potential created by missing nucleus make the positron techniques sensitive to defect concentrations ranging from 10^{-7} to 10^{-4}. A simplified schematic diagram of thermalized positron diffusing and trapping at a vacancy is shown in Figure-1.9.

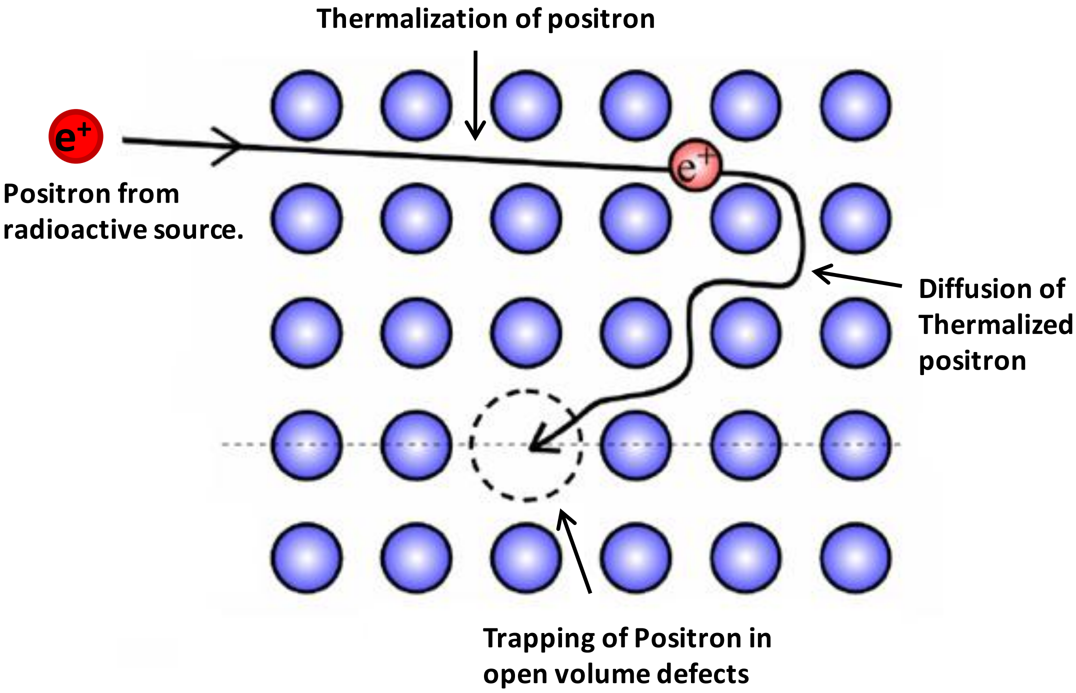

Figure-1.9: Schematic diagram of thermalization and diffusion of positron followed by trapping in a vacancy [66]. The missing ion core acts as a negative potential and traps positron.

Positron annihilation spectroscopy (PAS) is extensively used as a tool to observe the precipitation stages in Fe based steels and many other alloys. Microstructural changes including precipitation are studied in age hardenable commercial Al-Zn-Mg based alloy [67, 68]. Trapping of positrons at matrix and TiC precipitate interfaces has been reported earlier in D9 steel. While Ti-free steel did not show any changes, Ti containing D9 steel exhibited larger lifetime at annealing temperature corresponding to TiC precipitation [69]. Microstructural changes, that includes formation of intermetallic precipitates, in β-quenched Zircaloy-2 [70] and M250 grade maraging steel [71] were investigated by positron annihilation, hardness and ultrasonic velocity measurements. Different stages of precipitation in the process of natural aging of pure Al-Mg-Si alloys were understood with positron, in combination with differential scanning calorimetry [72] resistivity and hardness [73]. Majority of this studies probed precipitates due to trapping of positrons at precipitate-matrix interfaces. A simplified schematic diagram of precipitate-matrix interface and grain boundaries is shown in Figure-1.10.

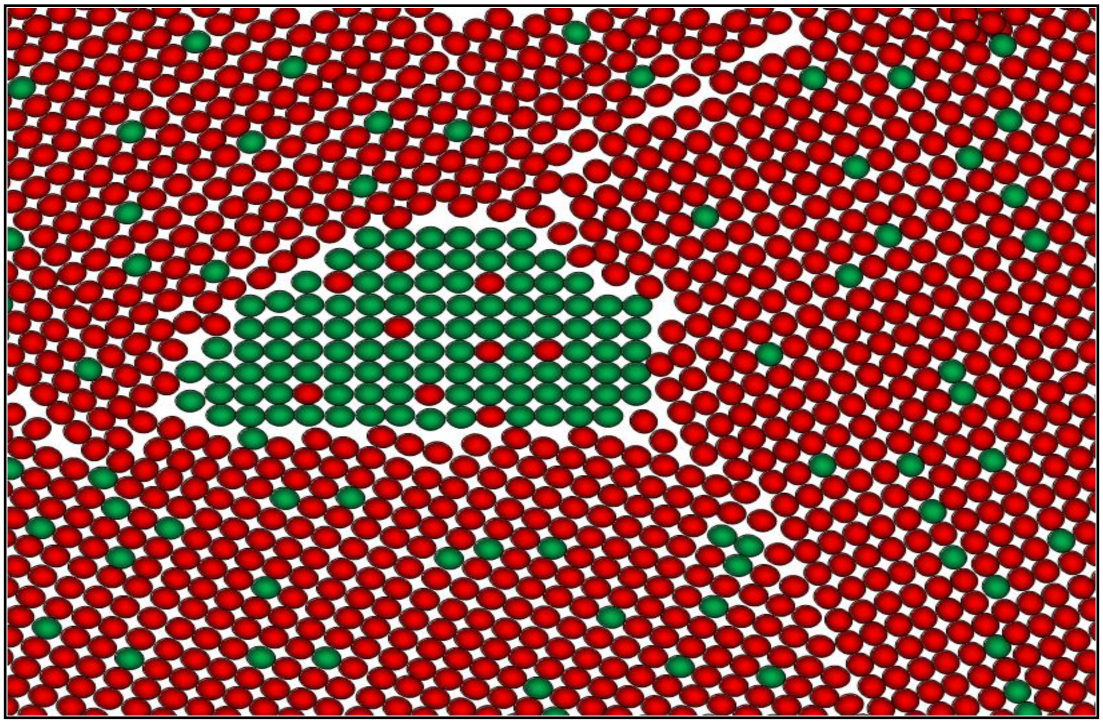

Figure-1.10: Schematic diagram of precipitate-matrix interface. Also shown are the grain boundaries.

PAS was used in characterizing irradiated Fe-Cr binary alloys in the past [56, 65, 74, 75, 76, 77, 78, 79]. This gives the confidence regarding the applicability of PAS to probe microstructural changes in ferritic/martensitic steel and Fe-Cr alloys.

1.8 MOTIVATION FOR THIS WORK

Microstructural characterization of ferritic steels at sub-micron range will be very important with varying chemical composition and heat treatment conditions. Extensive use of TEM is a requisite for these developments, which consumes greater time in terms of sample preparation and characterization. PAS could fit as a preliminary characterization tool to investigate indicative changes in the microstructure, especially the precipitation evolution, due to its sensitivity to associated atomistic defects. Based on the information obtained from PAS, the necessary electron microscopy studies can be carried out on selected samples. Also, PAS could serve as an effective NDE technique in probing the microstructure of ferritic steels during operation [80].

This thesis aims at investigating and establishing a correlation between positron annihilation parameters and microstructural changes, focusing on precipitate evolution, in ferritic/martensitic steels by studying two typical ferritic/martensitic steels i.e. EUROFER97 and Modified 9Cr-1Mo steel. Further, it aims at understanding Cr segregation in pure Fe-Cr binary alloys with varying concentration and the role of microstructure and dislocations on segregation. While the thesis presents detailed positron annihilation studies on all these systems, corroborative studies have also been carried out using electron microscopy, hardness and ultrasonic velocity measurements to obtain a comprehensive picture.

1.9 REFERENCES

---

[1] E. Lucon, P. Benoit, P. Jacquet et.al., Fus. Eng. Des. **81**, 917 (2006).

2 S. L Manan, S.C. Chetal, B. Raj, S.B. Bhoje, Trans. Ind. Inst. Metals **56**, 155 (2003).

[3] A. Hishinuma, A. Kohyama, R. L. Klueh, D. S. Gelles, W. Dietz, K. Ehrlich, J. Nucl. Mater. **258-263**, 193 (1998).

[4] Yusuke Kudo, Kouichi Kikuchi, Masakatsu Saito, J. Nucl. Mater. **307-311**, 471 (2002).

[5] H. M. Chung, B. L. Loomis and D. L. Smith, "U.S. Contribution, 1994 Summary Report, Task T12: Compatibility and Irradiation Testing of Vanadium Alloys, " ed. D. L. Smith, ANL/FPP/TM-287, ITER/US/95/IV MAT 10, March 1995, pp 147-155.

[6] R. L. Klueh, A. T. Nelson, J. Nucl. Mater. **371**, 37 (2007).

[7] N. Baluc, R. Schaublin, P. Spatig, M. Victoria, Nucl. Fusion **44**, 56 (2004).

[8] R. L. Klueh, J. J. Kai, D. J. Alexander, J. Nucl. Mater. **225**, 175 (1995).

[9] D. S. Gelles unpublished work trough R. L. Klueh, ORNL/TM-2004/176.

[10] P. J. Maziasz, R. L. Klueh, J. M. Vitek, J. Nucl. Mater. **141-143**, 929 (1986).

[11] M. Rieth, M. Schirra, A. Falkenstein, P. Graf, S. Heger, H. Kempe, R. Lindau, H. Zimmermann, Karlsruhe Research - Scientific reports - **FZKA 6911** (2003).

[12] K. Seidel, R. A. Forrest, H. Freiesleben, V. D. Kovalchuk, D. V. Markovskij, D. V. Maximov, S. Unholzer, J. Nucl. Mater. **307-311**, 1037 (2002).

[13] D. S. Gelles, J. Nucl. Mater. **239**, 99 (1996).

[14] R. L. Klueh, ORNL/TM-2004/176

[15] M.K. Booker, V. K. Sikka, B. L. P. Booker, Proc. of ASM International conference on ferritic steels for High Temperature Applications, Warrendale. PA. Ashok K. Khare (Eds.). ASM, Metals Park, OH , 1981, pp. 257-273.

[16] Z. Tong, Y. Dai, J. Nucl. Mater. **398**, 43 (2010).

[17] Sikka V K, in Proc. AIME Topical Conf. on Ferritic Alloys for Use in Nuclear Energy Technologies, (Eds.) Davis J W and Michael D J, Snowbird, Utah 317 (1983).

[18] F. Abe and S Nakazawa, Mater. Sci. Technol. **8**, 1063 (1992).

---

[19] F. Abe, Sci. Technol. Adv. Mater. **9**, 013002 (2008).

[20] R.L. Klueh , D.J. Alexander, J. Nucl. Mater. **233-237**, 336 (1996).

[21] A. Kohyama, A. Hishinuma, D.S. Gelles, R.L. Klueh, W. Dietz, K. Ehrlich, J. Nucl. Mater. **233-237**, 138 (1996).

[22] K. Mergia, N. Boukos, J. Nucl. Mater. **373**, 1 (2008).

[23] P. Fernandez, M. Garcia-Mazario, A. M. Lancha, J. Lapena, J. Nucl. Mater. **329-333**, 273 (2004).

[24] F. Abe, Mater. Sci. Eng. A **387-389**, 565 (2004).

[25] K. Maruyama, K. Sawada, J Koike, ISIJ Int. **41**, 641 (2001).

[26] N. Ridley, S. Maropoulos, J. D. H. Paul, Mater. Sci. Technol. **10**, 239 (1994).

[27] J. J. Kai, R. L. Klueh, J. Nucl. Mater. **230**, 116 (1996).

[28] P. Fernandez, A. M. Lancha, J. Lapena, M Hernandez-Mayoral, Fusion Engineering and Design **58-59**, 787 (2001).

[29] R. L. Klueh, A. T. Nelson, J. Nucl. Mater. **371**, 37 (2007).

[30] R. L. Klueh, Inter. Mater. Rev. **50**, 287 (2005).

[31] Y. de Carlan, A. Alamo, M. H. Mathon, G. Geoffroy, A. Castaing, J. Nucl. Mater. **283-287**, 672 (2000).

[32] Wendell B. Jones, C. R. Hills, D. H. Polonis, Metall. Trans. A **22A**, 1049 (1991).

[33] K. Maruyama, K. Sawada, J Koike, ISIJ Int. **41**, 641 (2001).

[34] B. Mintz, E. M. Maina, W. b. Morrison, Mater. Sci. Technol. **24**, 177 (2008).

[35] F. Abe, Metall. Mater. Trans. A **34**, 913 (2003).

[36] S. Takeuchi and A. S. Argon, J. Mater. Sci. **11**, 1542 (1976).

[37] M. Taneike, K. Sawada, F. Abe, Metall. Mater. Trans. A **35**, 1255 (2004).

[38] V. Thomas Paul, S. Saroja, M. Vijayalakshmi, J. Nucl. Mater. **378**, 273 (2008).

---

[39] P Fernandez, A.M Lancha, J Lapena, M Serrano, M Hernandez-Mayoral, J. Nucl. Mater. **307-311**, 495 (2002).

[40] M. Schirra, A. Falkenstein, P. Graf, S. Heger, H. Kempe, R. Lindau, H. Zimmermann, **FZKA 6707**, (2002).

[41] A. Alamo et al., Fusion Technology CEA annual report 2001, Ass. CEA/EURATOM, Saint-Paul-lez-Durance, 239 (2002).

[42] T. Angeliu, E. L. Hall, M. Larsen, A. Linsebigler, C. Mukira, Metall. Mater. Trnas. A **34A**, 927 (2003).

[43] M.H. Mathon et al., in: The 20th ASTM Symposium on Efects of Radiation on Materials, Williamsburg, VA, 6 – 8 June 2000.

[44] H. Kuwano and Y. Hamaguchi, J. Nucl. Mater. **155–157**, 1071 (1988).

[45] H. Okamoto, Cr-Fe, in ASM Handbook: Volume 3: Alloy Phase Diagrams, H. Baker, Ed. ASM International: Materials Park, OH. 1991.

[46] Wei Xiong, Malin Selleby, Qing Chen, Joakim Odqvist, Yong Du, Crit. Rev. Solid. State **35**, 125 (2010).

[47] J. J. Demo, ASTM STP 619, ASTM, Philadelphia, PA, (1977).

[48] T. J. Nichol, A. Datta, G. Aggen, Metall. Trans. A **11A**, 573 (1980).

[49] P. J. Grobner, Metall. Trans. A **4**, 251 (1973).

[50] G. Bonny, R.C. Pasianot, D. Terentyev, L. Malerba, open report, SCK•CEN-BLG-1077, (2011).

[51] Mirebeau, G. Parette, Phys. Rev. B **82**, 104203 (2010).

[52] C. Heintze, A. Ulbricht, F Bergner, H Eckerlebe, J. Phys.: Conf. Ser. **247**, 012035 (2010).

[53] M. Matijasevic, A. Almazouzi, J. Nucl. Mater. **377**, 147 (2008).

[54] E. A. Little, D. A. Stow, J. Nucl. Mater. **87**, 25 (1979).

[55] E. A. Little, D. A. Stow, Mat. Sci. **14**, 89 (1980).

[56] E. Kuramoto, S. Nagano, K, Nishi, K. Makii, Y. Aono M. Takenaka, Mater. Sci. Forum **105-110**, 1125 (1992).

---

[57] P. Druzhkov, V. L. Arbuzov, D. A. Perminov, Phys. Met. Metallorgr. **111(2)**, 218 (2011).

[58] T. Ezawa, T. Akashi, R. Oshima, J. Nucl. Mater. **212-215**, 252 (1994).

[59] Vladimir Krsjak, Vladimir Slugen, Marek Miklos, Martin Petriska, Peter Ballo, Appl. Surf. Sci., **255**,153 (2008).

[60] J. Kwon, T. Toyama, Y. -M. Kim, W. Kim, J. -H. Hong, J. Nucl. Mater. **386-388**, 165 (2009).

[61] Par Olsson, Christophe Domain, Janne Wallenius, Phys. Rev B **75**, 014110 (2007).

[62] G. Bonny, D. Terentyev, L. Malerba, D. Van Neck, Phys. Rev. B **79**, 104207 (2009).

[63] D. Terentev, P. Olsson, L. Malerba, A. V. Barashev, J. Nucl. Mater. **362**, 167 (2007).

[64] Song Lu, Qing-Miao Hu, Rui Yang, Borje Johansson,Levente Vitos, Phys. Rev. B **82**, 195103 (2010).

[65] S. Hari Babu, R. Rajaraman, G. Amarendra, R. Govindaraj, N. P. Lalla, Arup Dasgupta, Gopal Bhalerao, C. S. Sundar, Philos. Mag. **92**, 2848 (2012).

[66] R. Krause-Rehberg, H. S. Leipner, Positron annihilation in semiconductors: Defect studies, Springer-Verlag, Berlin, 1998.

[67] R Ferragut, A Somoza, A Dupasquier, J. Phys.: Condens. Matter. **8**, 8945 (1996).

[68] A. Dupasquier, R. Ferragut, M. M. Iglesias, M. Massazza, G. Riontino, P. Mengucci, G. Barucca, C. E. Macchi, A. Somoza, Phil. Mag. A **87**, 3297 (2007).

[69] R. Rajaraman, Padma Gopalan, B. Viswanthan, S.Venkadesan, J. Nucl. Mater. **217**, 325 (1994).

[70] P. Gopalan, R. Rajaraman, G. Amarendra, C. S. Sundar, B. Viswanathan, T. Jayakumar, Palanichamy, B. Raj. J. Nucl. Mater. **345**, 162 (2005).

[71] K. V. Rajkumar, R. Rajaraman, Anish Kumar, G. Amarendra, T. Jayakumar, Philos. Mag. **89**, 1597 (2009).

[72] J. Banhart, M. D. H. Lay, C. S. T. Chang, A. J. Hill, Phys. Rev. B **83**, 014101 (2011).

[73] J. Banhart, M. Liu, Y. Yong, Z. Liang, C.S.T. Chang, M. Elsayed, M.D.H. Lay, Physica B: Condensed Matter **407**, 2689 (2012).

[74] P. Druzhkov, V. L. Arbuzov, D. A. Perminov, Phys. Met. Metallorgr. **111(2)**, 218 (2011).

---

[75] J. Kwon, T. Toyama, Y. -M. Kim, W. Kim, J. -H. Hong, J. Nucl. Mater. **386-388**, 165 (2009).

[76] E. Kuramoto, Y. Takano, N. Kikuchi, M. Takenaka, J. Nucl. Mater. **141-143**, 829 (1986).

[77] V. Krsjak, V. Slugen, M. Miklos, M. Petriska, P. Ballo, Appl. Surf. Sci. **255**, 153 (2008).

[78] M. Lambrecht, L. Malerba, Acta Mater. **59**, 6547 (2011).

[79] V. Krsjak, S. Sojak, V. Slugen, M. Petriska, J. Phys.: Conf. Ser. **265**, 012014 (2011).

[80] S. Hari Babu, K. V. Rajkumar, S. Hussain, G. Amarendra, C. S. Sundar and T. Jayakumar, J. Nucl. Mater. **432**, 266 (2012).

Chapter - 2

Experimental Methods

2.0 PREAMBLE

This chapter presents the details of experimental techniques and analysis procedures of positron annihilation spectroscopy (PAS) used in the present thesis. Brief description of other techniques used i.e., electron microscopy (TEM, SEM), Vickers hardness and ultrasonic velocities, is presented. It also sketches the heat treatment procedures.

2.1 POSITRON SOURCE

In the present thesis work, ^{22}Na source, commonly used positron source, is used for all PAS measurements. ^{22}Na decays into ^{22}Ne with emission of a positron and a neutrino. The end point energy of emitted positrons is around 543 keV [1]. Further, a gamma ray of energy 1274 keV is emitted from ^{22}Ne in about 4 ps after positron emission. This gamma ray provides the reference time signal corresponding to the birth of positron, usually called start signal. The positron that enters the sample slows down by inelastic collisions to thermal energies in a few picoseconds. After equilibration, either in bloch states or trapped states, the positron annihilate with an electron in the medium. The annihilation results in emission of dominantly two 511 keV gamma rays nearly in opposite directions. Figure-2.1 shows schematic diagram of different stages between positron emission and annihilation.

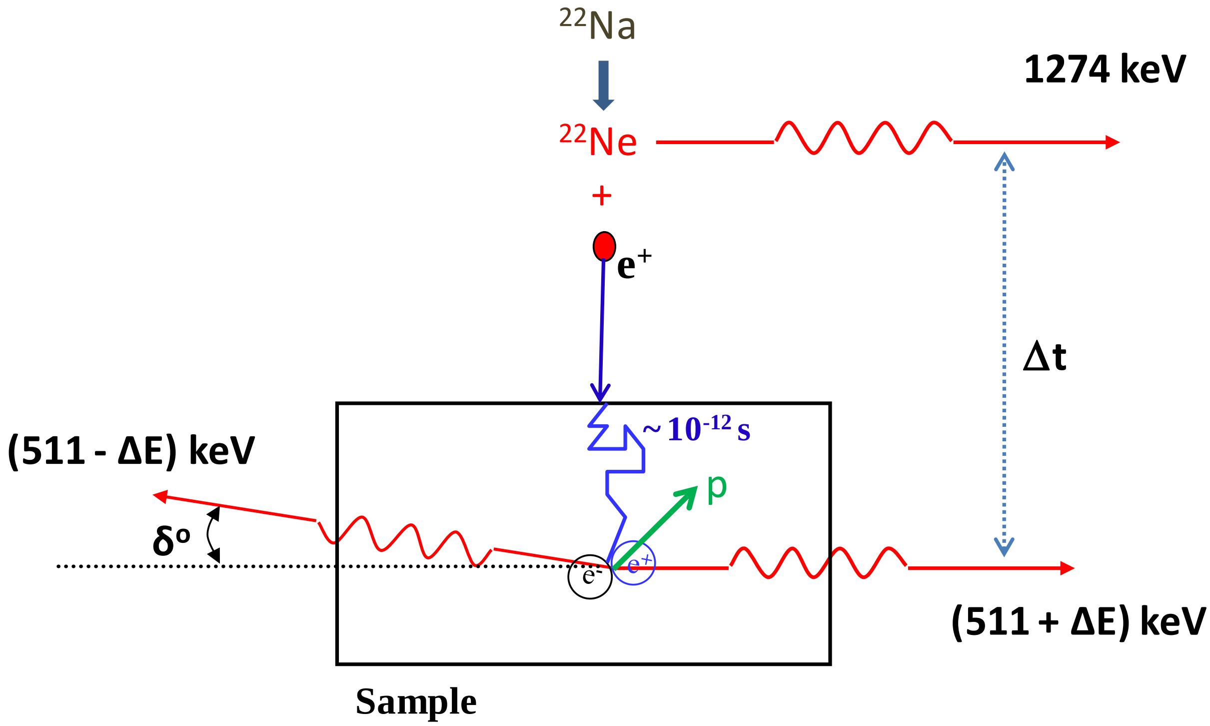

Figure-2.1: Schematic diagram of positron emission from ^{22}*Na, thermalization , diffusion and annihilation with electron. The shift in energy (ΔE) of annihilated gamma rays from 511 keV is to conserve the positron-electron momentum component in the direction of gamma ray emission. The penetration depth of positrons is around 100 μm in metals. The diffusion length of positrons after thermalization is around 100 nm [2]. The distribution of Δt constitutes lifetime spectra. δ° is the deviation from collinearity of the gamma rays.*

2.2 POSITRON LIFETIME MEASUREMENTS

2.2.1 Positron lifetime spectroscopy

The distribution of time intervals (Δt), between 1274 keV start gamma and annihilated 511 keV stop gamma ray, constitutes the lifetime spectrum. According to the theoretical model, the lifetime spectrum is a sum of multiple elementary exponential functions, each corresponding to a distinct annihilation site. The lifetime of positron at a site is inversely proportional to the electron density at the annihilation site. The lifetime of positron varies from 100 to 418 ps [3] in defect-free metallic materials. Positron lifetime in defect-free metals encountered in this thesis are Fe (108 ps), Cr (120 ps), Mo (106 ps), W (105 ps), Al (165 ps), Ti (150 ps) and Ni (109 ps). However, the electron density at open volume defects is significantly lower than that of defect-free lattice. Hence, sample containing defects will have higher lifetime components corresponding to those defects. Figure-2.2 shows the comparison of lifetime spectra of annealed and deformed nickel. Deformation was carried out by cold-working to a thickness reduction of 30%. It can be seen that the annealed rate (inverse of lifetime) of deformed nickel spectrum is lower than the annealed nickel spectrum. Thus, the presence of defects results in an increase in the lifetime.

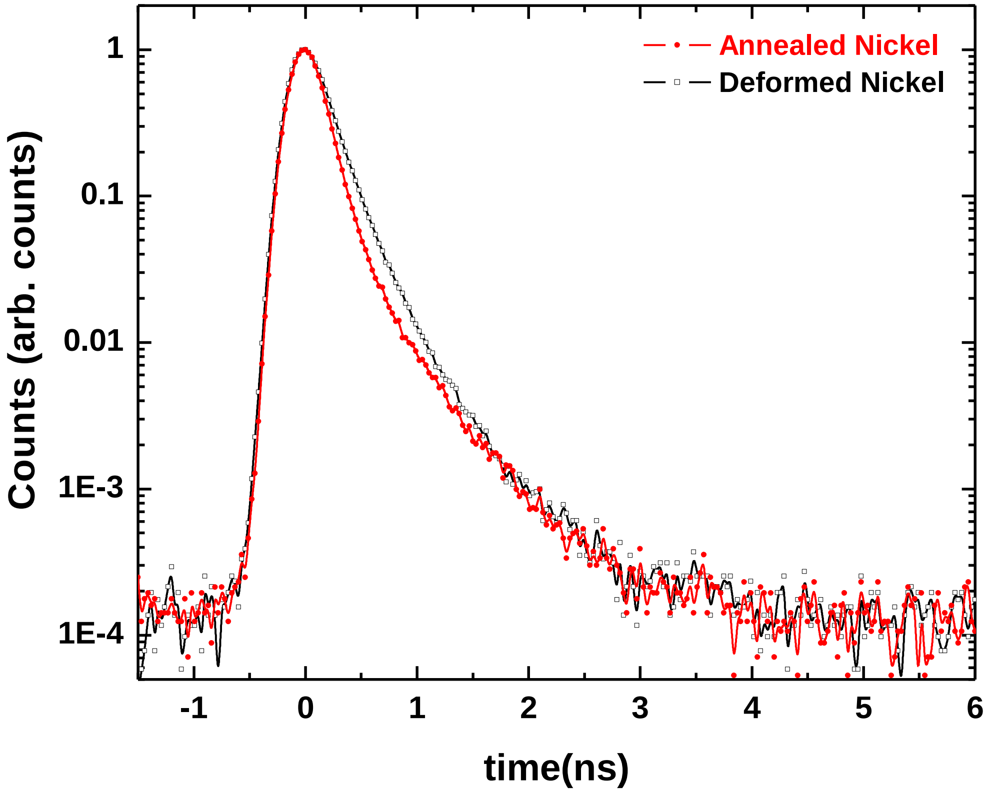

Figure-2.2: Lifetime spectra of annealed nickel and deformed nickel. The spectra are peak normalized for comparison of annihilation rate. The annihilation rate of deformed nickel spectrum is seen to be lower. The average lifetime of annealed nickel and deformed nickel obtained from these spectra are 111 ± 2 ps and 166 ± 2 ps, respectively [4].

2.2.2 Positron lifetime spectrometer

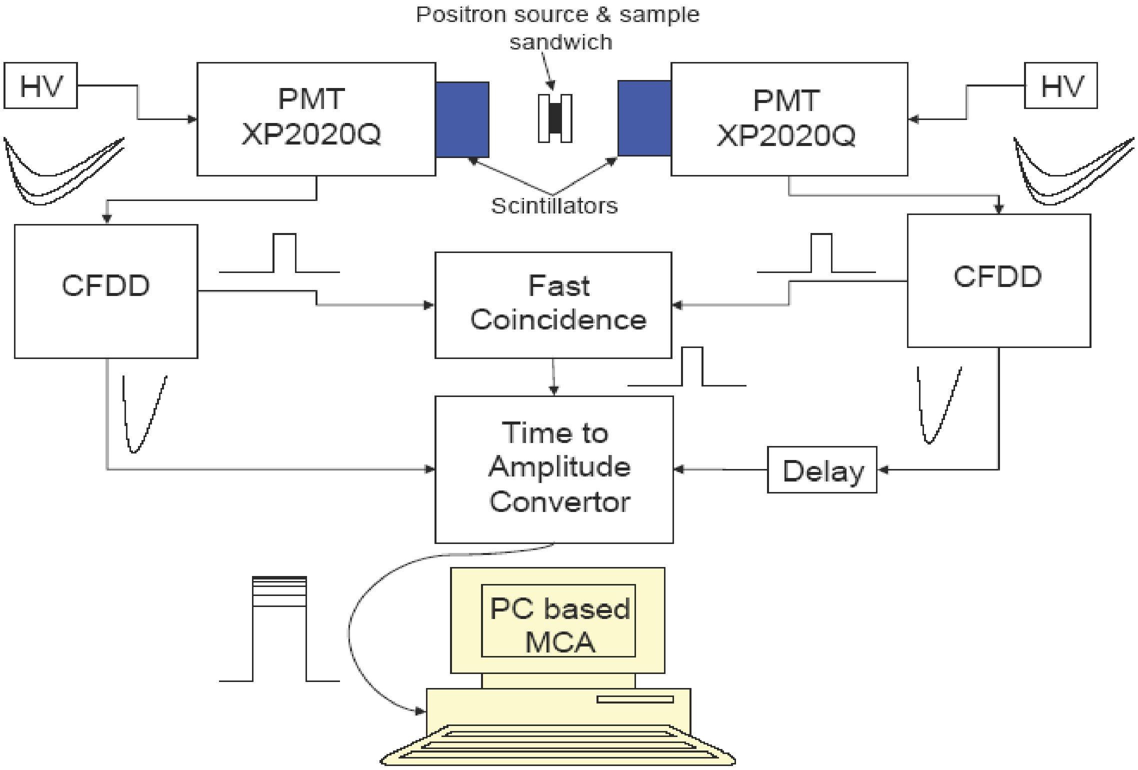

Figure-2.3: Fast-fast coincidence spectrometer used for positron lifetime experiments. The scintillators used for gamma detection are BaF_2 crystals.

All positron lifetime measurements of this thesis work were carried out with a fast-fast coincidence lifetime spectrometer. The block diagram of spectrometer is shown in Figure-2.3. The detectors used for gamma detection are BaF_2 scintillators (Scionix, Holland) coupled to XP2020Q photomultiplier tubes (PMTs), having a quartz window. The output pulses of PMTs are fed to respective constant fraction differential discriminators (CFDD). The CFDD discriminates the pulse heights for a definite energy band with a set values of lower level discriminator (LLD) and upper level discriminator (ULD). The LLD and ULD for the start pulse and the stop pulse are set such that it selects 1274 keV and 511 keV gamma rays, respectively. For each valid input, the CFDD provides a fast logic timing pulse and a Transistor-Transistor-Logic (TTL) pulse. The TTL pulses are fed to a fast coincidence unit operating at a resolving time of 20 ns. The start and stop timing signals from CFDD are fed to a time to amplitude converter (TAC). The stop timing signals from CFDD are delayed by extra cable to shift the time spectrum. The TAC is gated by the output of fast-fast coincidence unit to get time interval between start and stop gamma rays of a single event. The output of TAC is fed to multi channel analyser (MCA) and then the output is transferred to a personal computer.

2.2.3 Analysis of lifetime spectra

An elementary lifetime component is an exponential function. The lifetime τ is inversely proportional to the electron density at the site at which positron annihilates. A lifetime spectrum is a combination of several components, each corresponding to a distinct site.

The annihilation rate λ at a site is given by the overlap of the positron density $n_+(r)$ and electron density $n_-(r)$ [1]

$$\lambda = \pi r_0{}^2 c \int n_+(r)\, n_-(r)\, \gamma\, dr \quad \text{-------------------} \quad 2.1$$

Where, r_o is the classical electron radius, c is the speed of light and r is the position vector. The enhancement factor $\gamma = 1 + (\Delta n_- / n_-)$ describes the increase in the electron density due to the coulomb attraction between positron and electron.

For n distinct sites of annihilation, n annihilation rates exist and the decay spectrum is a sum of all the components with corresponding intensities proportional to fraction of annihilation at the site. The experimental lifetime spectrum, $I(t)$ is a time derivative of decay spectrum

$$I(t) = \sum_{i=1}^{n} I_i\, \lambda_i e^{-\lambda_i t} \quad \text{-------------------} \quad 2.2$$

In principle, all the components can be extracted from lifetime spectrum. However, the spectrometer resolution and the data error connected with the instrumental drifts impose limitations on how close the distinct lifetimes can be resolved.

All the spectra are analyzed with LT program [5]. In the case of discrete lifetimes, the convoluted physical model function (2.2) with appropriate instrument function (FWHM) will be fitted with experimental spectrum to obtain the optimum values of the model parameters. Figure-2.4 shows the prompt spectrum of ^{60}Co comparing with positron lifetime spectrum.

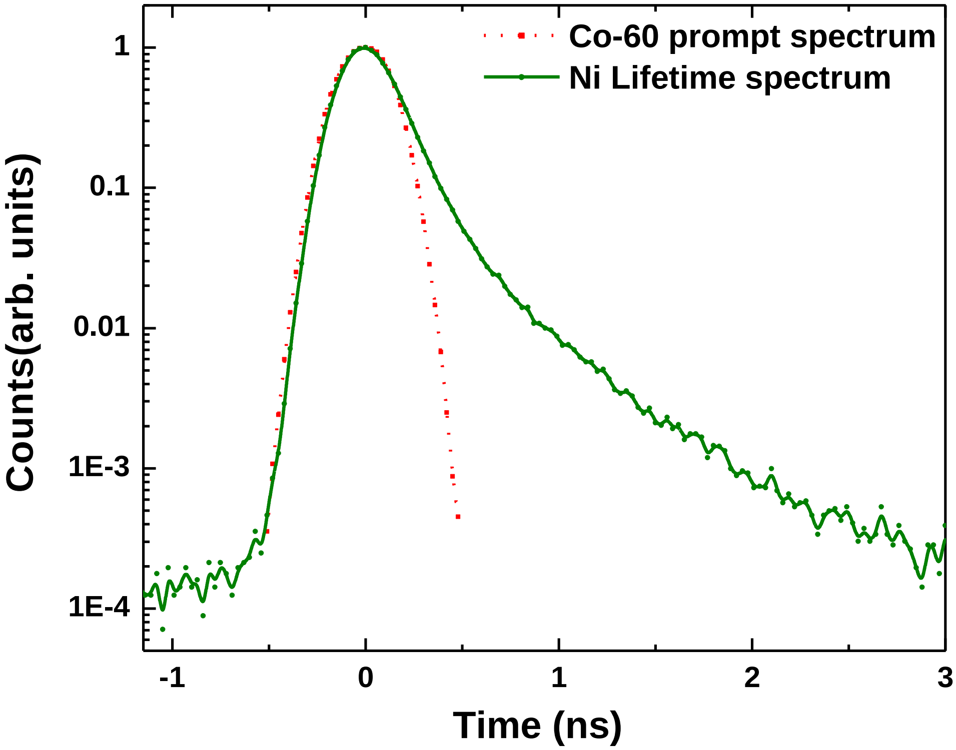

Figure-2.4: The prompt spectrum of ^{60}Co along with lifetime spectrum of annealed nickel.

For the systems studied in this thesis, the maximum average lifetime is about 150 ps. In each case, the measured lifetime spectra were attempted to be fit with two or more components. However, the resolved components were neither consistent nor meaningful, despite a slight improvement in variance. It is believed that the difference between bulk lifetime value and the lifetime of trapped sites is quite small. Hence, we resort to present only the average lifetime in the studies reported later on.

2.3 DOPPLER BROADENING MEASUREMENTS

2.3.1 Doppler broadening spectroscopy

To conserve the momentum of annihilating positron-electron pair in the direction of annihilated gamma rays, the energy of annihilated gamma rays will be Doppler shifted by $\pm\Delta E$. The majority of contribution comes from the electron momentum as thermal energy of positron is negligible in the material. Since the shift in energy ΔE is equal to $cp_z/2$, where p_z is the momentum component of electron-positron pair in the emission direction of annihilated gamma ray, the Doppler shift will be larger for annihilation with high momentum electrons. Hence, the Doppler broadening for positron annihilation inside defect-free pure metal sample, generally, increases with atomic number. Figure-2.5 shows the increase in DB with increase in atomic number between Al, Ti, and Ni.

On the other hand, for the samples containing positron trapping open volume defects the probability of annihilations with free and valence electrons increases as compared to the case defect-free lattice. The free electrons and valence electrons will have lower momentum than core electrons. Hence, the Doppler broadening decreases for samples containing open volume defects as compared to defect-free samples. Figure-2.6 shows the DB curves of annealed and deformed nickel samples. The deformation of Ni sample was carried out by cold-working to 30% reduction in thickness.

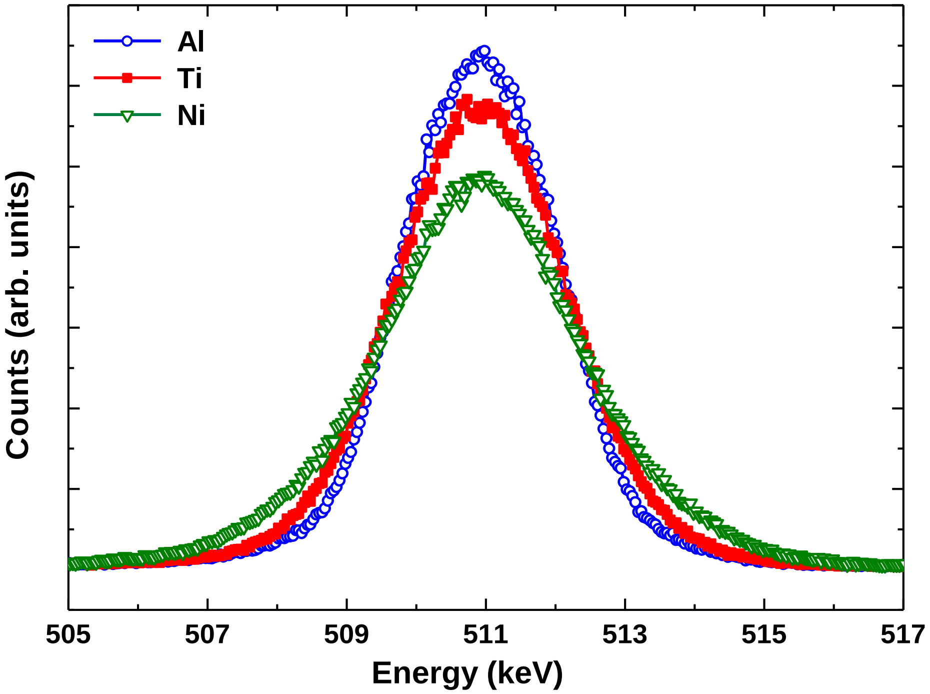

Figure-2.5: Positron annihilation Doppler broadening in annealed Al, Ti, and Ni alloys. Broadening increased with atomic number.

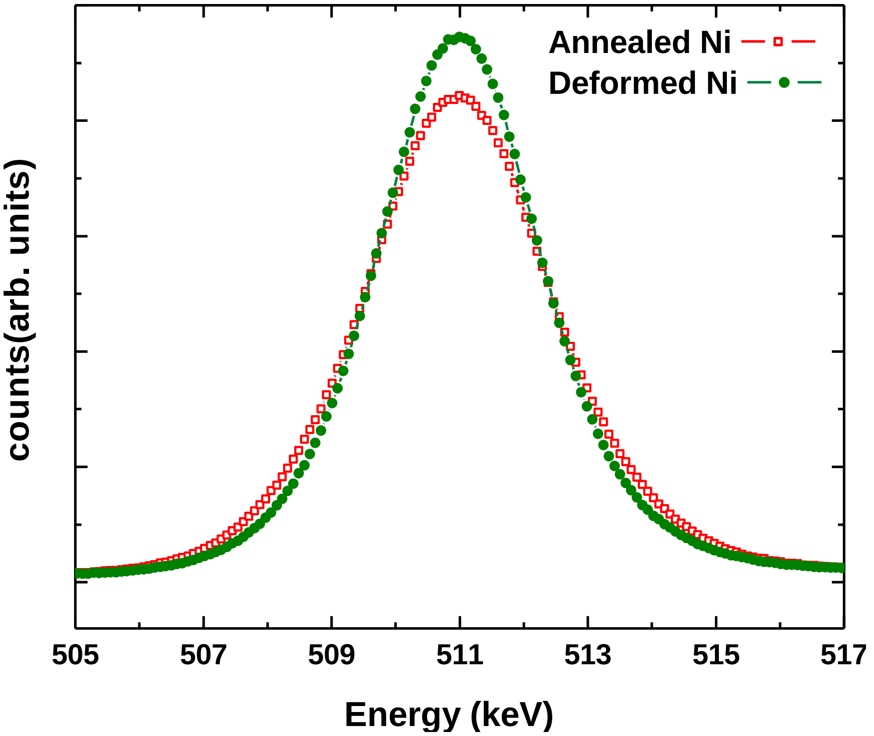

Figure-2.6: Positron annihilation Doppler broadening curves of annealed and deformed Ni samples. The broadening decreased in defect present deformed Ni samples [3].

Since, open volume defects trap positrons [6, 7] and the annihilation characteristics are dependent on the nature and concentration of these defects, changes in open volume defect concentrations can be studied qualitatively.

However, in the case of alloys, when there is a preferential bonding between open volume defects and one or more of the minor alloying elements, the characteristics of electrons from the minor alloying elements govern the annihilation characteristics. The effect will be more pronounced when the atomic number difference between minor alloying element and major element is significant.

The above observation will be useful when the interest is to probe such chemical nature of alloying elements associated with vacancies. However, to bring out the characteristic momentum distribution of core electrons, the background that dominates at the high momentum component of DB spectrum should be suppressed significantly. Coincidence Doppler broadening technique will reduce the background by three orders to allow us to study high momentum contributions [8, 9].

2.3.2 Doppler broadening spectrometer

The Doppler broadening annihilation line shape measurements were carried out using a p-type High Pure Germanium (HPGe) detector of 30% efficiency with built-in preamplifier. The output pulse of the detector is fed to a spectroscopy amplifier and multichannel analyzer. The data from MCA is acquired in a personal computer. The energy resolution (FWHM) of the detector is 1.26 keV at 662 keV, measured using standard ^{137}Cs source, with an energy calibration of 70 eV/channel. A typical Doppler broadening annihilation peak of annealed Ni along with ^{137}Cs 661.6 keV peak is shown in the Figure-2.7.

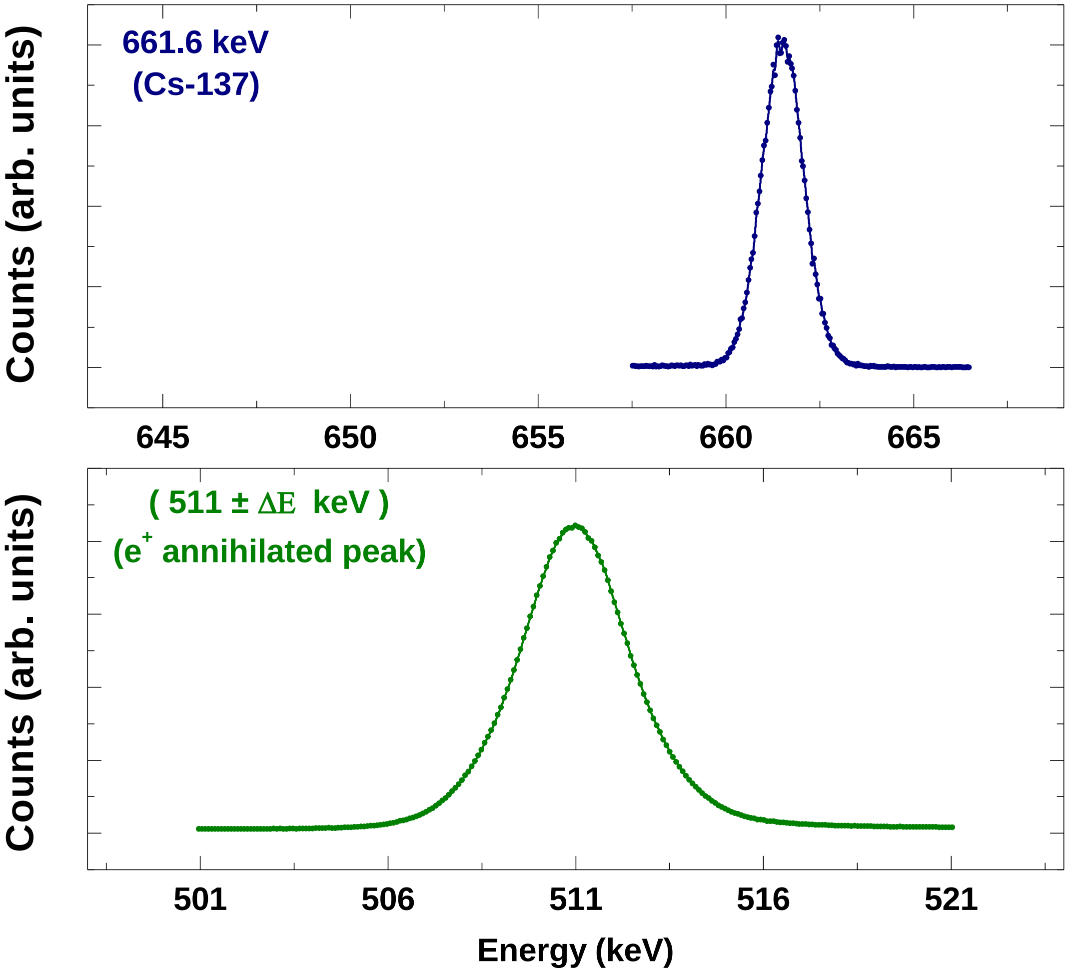

Figure-2.7: Comparison of positron annihilation Doppler broadened 511 keV peak with ^{137}*Cs decay 661.6 keV peak.*

2.3.3 Analysis of Doppler broadening spectra

The defect sensitive S-parameter is defined as ratio of peak counts to total counts of Doppler broadening annihilation peak i.e. $S = N_p / N_{Total}$ (Figure-2.8). The total counts are defined as area of 511 ± 10 keV. The peak counts are defined as area of 511 ± 1 keV. The increase in S-parameter corresponds to increase in fraction of annihilations with low momentum electrons. This implies an increase in open volume defects, provided that the nature of defects remains the same i.e., there is no preferential accumulation of minor alloying elements next to vacancies. W-parameter corresponds to the ratio of $(N_{w1} + N_{w2}) / N_{total}$ as shown in Figure-2.8.

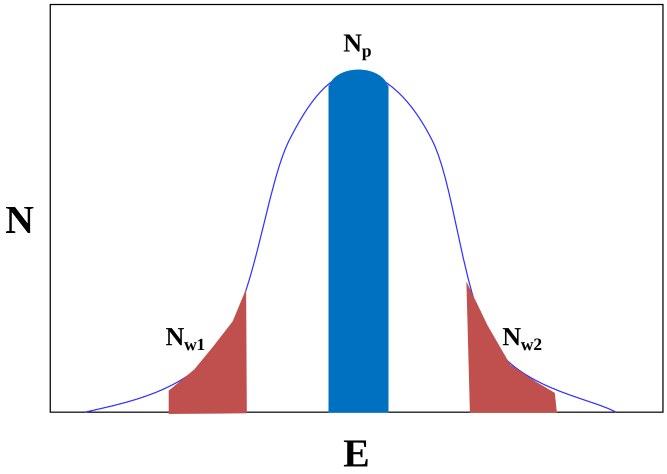

Figure-2.8: Schematic representation of windows for peak counts (N_p) for S-parameter measurements and wing counts ($N_{w1} + N_{w2}$) considered for W-parameter. S-parameter is defined as N_p/N_{total} and W-parameter is defined as $(N_{w1} + N_{w2})/N_{total}$.

S and W-parameters are not absolute parameters that they can be reproduced independent of instrumental functions. It varies with resolution of the detector and the respective energy windows for S and W-parameters. Hence, it is always useful to compare a series of measurements taken with same instrumental parameters.

However, there will be situations where the S-parameter values do not convey information regarding presence or absence of defects, especially, when we do not have reference spectra. Also, fine changes in S-parameter can be considered within error. However, the comparison of area normalized virgin data conveys such information. Such a situation arises in chapter-5 of this thesis. In such case, area normalized data of a reference sample is subtracted from the data of samples to be probed to get the better understanding. Similar situation arises in appendix to compare the relative signal to background ratio of DB spectra taken with different backgrounds. Figure-2.9 shows one such result where area normalized data of annealed Ni subtracted from data of deformed Ni. It shows increase in low momentum contribution and decrease in high momentum contribution in deformed sample. Since the interest is only on low momentum counts, this procedure worked well than ratio method.

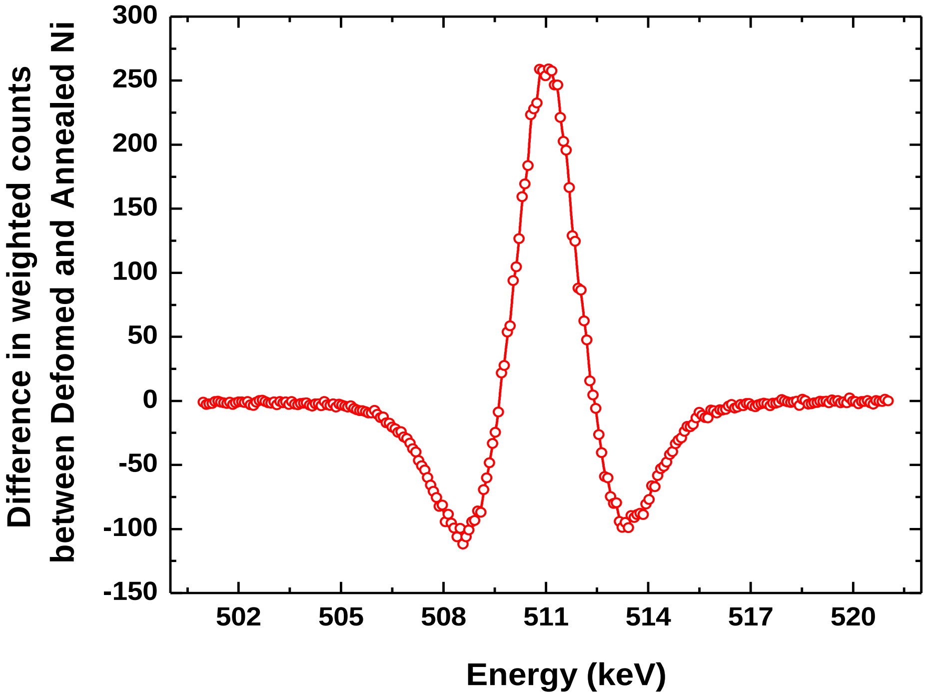

Figure-2.9: The difference in area normalized spectra of annealed and deformed nickel.

2.3.4 Coincidence Doppler broadening spectrometer

Two identical p-type HPGe detectors having energy resolution of 1.26 keV at 662 keV are placed opposite to each other with source-sample sandwich on axial line of detector end caps. The block diagram of the spectrometer is shown in Figure-2.10. The outputs of spectrometer amplifier are connected to analog-to-digital (ADC) converters and they are fed to dual parameter multichannel analyzer for coincidence and data storage of two gamma rays of the same event. The data then is transferred to personal computer.

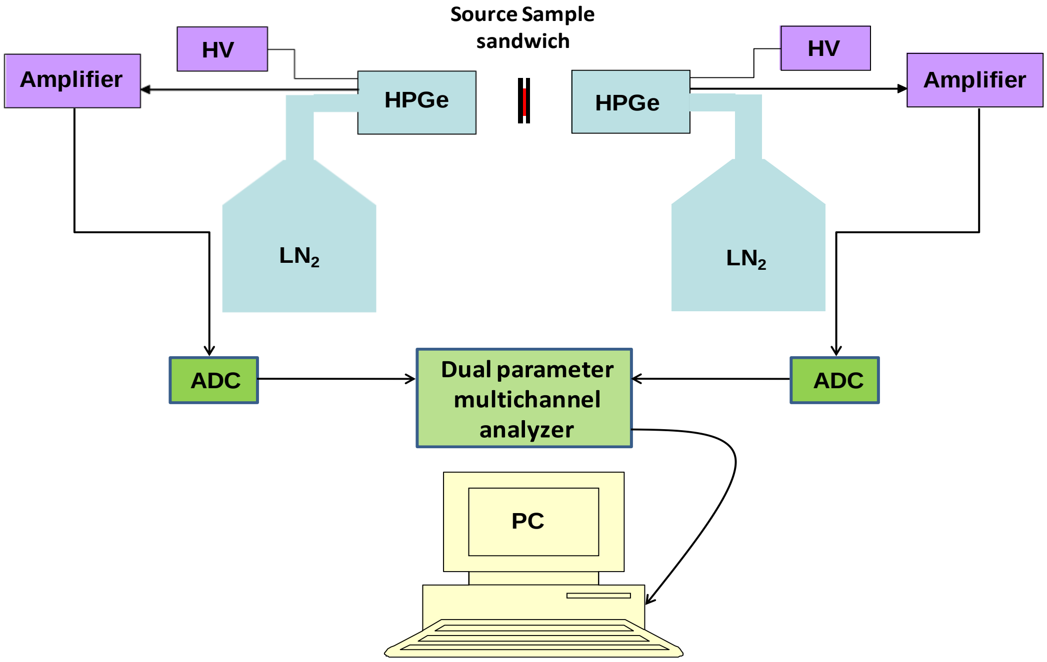

Figure-2.10: Block diagram of coincidence Doppler broadening S-parameter.

2.3.5 Analysis of CDB spectra

The acquired two-dimentional array of gamma counts are extracted by constraining the total energy of two gamma rays of single event to be within (2 x 511) ± δE keV, where δE is the error allowed during the data extraction. An error of ±1 keV is allowed in this study. This will eliminate the off diagonal counts, which contribute to background counts. A typical CDB two-dimensional array spectrum is shown in Figure-2.11 with marked regions of selection of data. The extracted data is area normalized and ratio with respect to reference spectrum is taken. In this thesis, spectrum of annealed Fe sample is taken as a reference.

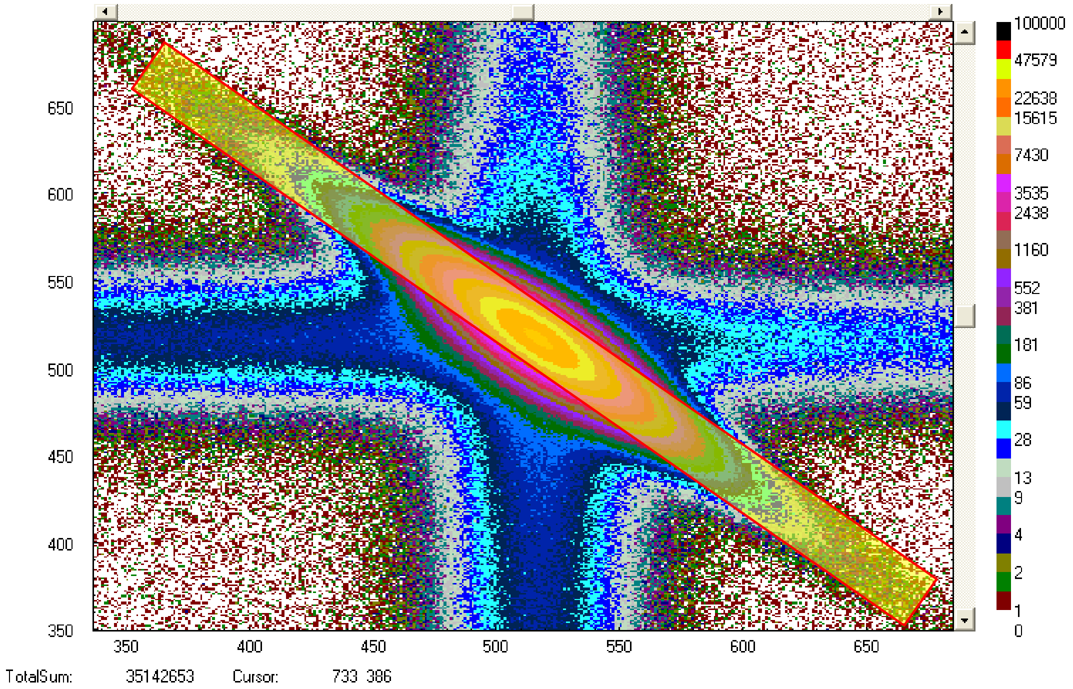

Figure-2.11: A typical two dimensional array of CDB spectra. The marked region is the window of extracted data for ratio curves.

2.4 TRANSMISSION ELECTRON MICROSCOPY

Transmission electron microscopy studies were carried out using two different instruments (1) Analytical Transmission Electron Microscopy (ATEM), M/S Philips CM 200 microscope, with operating voltage of 200 kV. (2) Tecnai-G^2-20 TEM microscope operating at 200 kV. Selected Area Diffraction (SAD) and Energy-dispersive X-ray spectroscopy (EDS) were used to identify the precipitates. Imaging was carried in conventional bright-field mode and occasionally in dark-field mode to identify the preferential orientations. SAD analysis was carried by getting real space *d* spacing values from inverse of distance between diffraction spots. From the *d* spacing values obtained and comparing with JCPDS data, the possible structure and corresponding (h k l) values will be identified. From the (h k l) values, theoretical interplanar angles will be calculated and cross checked with the angles from diffraction pattern to confirm the structure and planes corresponding to diffraction.

2.5 SCANNING ELECTRON MICROSCOPY

Scanning electron microscopy was carried out using two different instruments (1) Carl Zeiss Field Emission Scanning Electron Microscope (FESEM) with INCA EDS analyser from M/S Oxford (2) Philips XL30 Scanning Electron Microscope (SEM), in secondary electron mode. Samples for electron microscopy were prepared by standard metallographic methods of grinding and polishing. Finely polished samples are etched with Vilella's Reagent (1g Picric Acid, 5ml HCl with 100ml Ethanol) to reveal the precipitates.

2.6 HARDNESS MEASUREMENTS

Fundamental properties such as resistance to plastic deformation, modulus of elasticity and yield strength can be predicted from hardness [10]. Static indentation hardness tests were conducted using Vickers microhardness tester (Leitz microhardness tester) with an applied load of 0.1 kg. A pyramidal indenter with a 136° angle is used. The basic concept is to apply a set force to an indenter in order to determine the resistance of the material to penetration. The size of indentation resulted after application of the force is inversely proportional to the hardness of the material. When the force is applied to the sample with the indenter, the material will yield. Biaxial residual stresses remain in the planes parallel to the free surface after the force is removed. The hardness values are calculated by the amount of permanent deformation of the material observed relative to the test force applied. The deformation is quantified by the area of indentation. The Vickers hardness values are calculated by dividing the test force by the surface area of the indentation.

$$HV = 1854.4\,\frac{P}{d^2} \qquad \text{-------------------} \qquad 2.3$$

P is test force in gf, d is mean diagonal of the indentation in µm.

2.7 ULTRASONIC VELOCITIES MEASUREMENTS

Velocity of ultrasound in a given medium varies with its physical properties. For a material of density ρ, the longitudinal velocity (V_L) and shear velocity (V_T) are related to Shear (G), Bulk (B) and Young's (E) moduli as follows,

$$G = {V_T}^2\rho \qquad \text{-------------------} \quad 2.4$$

$$B = \rho\left({V_L}^2 - \frac{4}{3}{V_T}^2\right) \quad \text{-------------------} \quad 2.5$$

$$E = 3\rho {V_T}^2 \,\frac{\left({V_L}^2 - \frac{4}{3}{V_T}^2\right)}{\left({V_L}^2 - {V_T}^2\right)} \quad \text{--------------------} \quad 2.6$$

The microstructural changes in the alloy affect the elastic moduli and hence, the ultrasonic velocity. Therefore, measurement of ultrasonic velocities inside an alloy can provide information on the microstructure of the alloy [11].

Ultrasonic longitudinal and shear velocities were carried at room temperature using a 10 MHz longitudinal wave and 5 MHz shear wave transducers. A 100 MHz broad band pulser-receiver (M/s. Accutron) and 500 MHz digitizing oscilloscope (M/s. Lecroy) were used for carrying out the ultrasonic velocity measurements. The cross-correlation technique has been used for precise velocity measurements [12]. For velocity measurements, the ultrasonic signals were digitized at 500 MHz and the gated backwall echoes from the oscilloscope were transferred to a personal computer with the help of the GPIB interface and specific software developed in LabVIEW. Samples for measurements were prepared by grinding to a constant thickness of 13 mm and plane parallelism to an accuracy of better than ± 3 µm. The accuracy in time-of-flight measurements was better than 1 ns, and the maximum scatter in ultrasonic velocity was found to be less than ± 3 m/s.

2.8 HEAT TREATMENTS

The major emphasis in this thesis is to investigate the effect of heat treatments on the microstructure of materials. This involves both isochronal and isothermal heat treatments. A tubular furnace, which can attain temperatures upto 1373 K, is used for heat treatments. The arrangement allows insertion of the samples, kept inside a quartz tube, after the furnace attains the set temperature. The other end of quartz tube will be connected to a dynamic vacuum < 10^{-5} torr, with the help of a diffusion pump. The time taken for the samples inside quartz tube to attain set temperature is calibrated for different temperatures and the heat treatment time is counted accordingly. The temperature and time program for the isochronal and isothermal heat treatment studies are shown in Figure-2.12 and Figure-2.13, respectively. For isothermal treatments, the sample is maintained successively at elevated temperature for 1 h and positron annihilation measurements are carried out at room temperature at the end of each heat treatment.

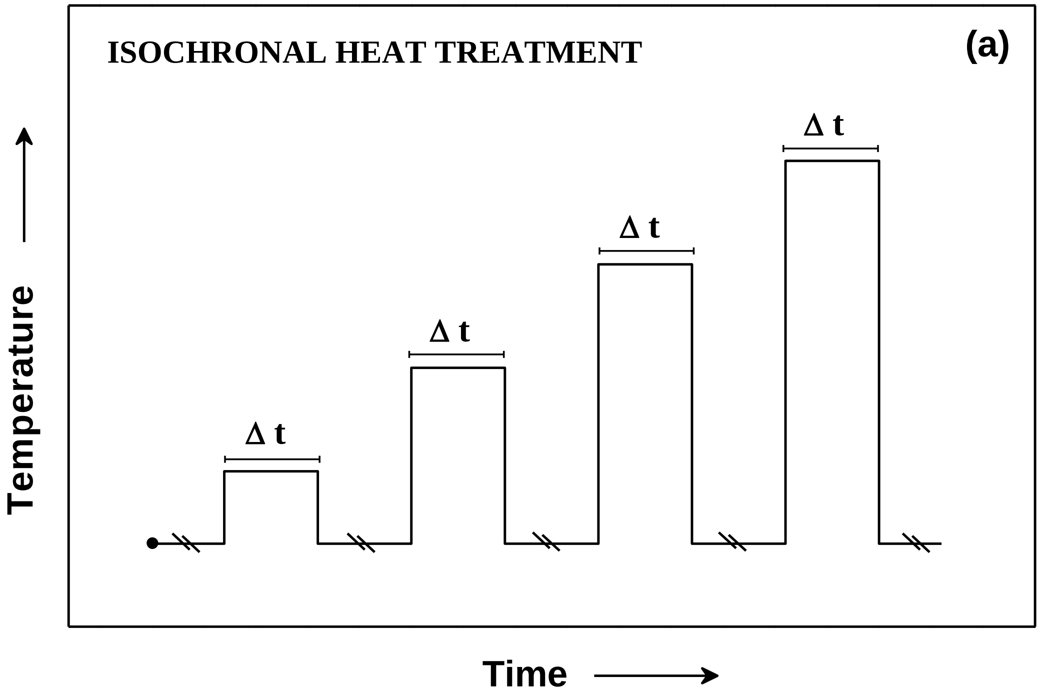

Figure-2.12: Isochronal heat treatment program used in the present studies. Δt = 1h.

In isothermal studies, the samples are annealed at a fixed temperature for various periods of time and positron studies are carried out at room temperature after each isothermal treatment.

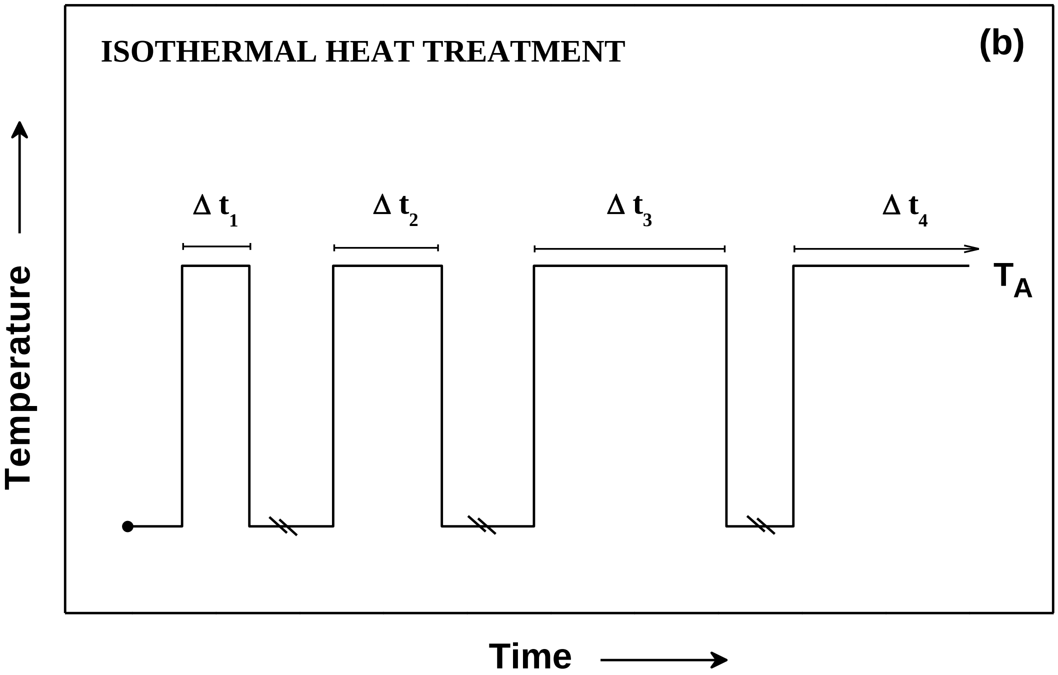

Figure-2.13: Isothermal heat treatment program used in the present studies.

The experimental methods mentioned here are used to find out the microstructural changes in EUROFER97, plain and modified 9Cr-1Mo steels and Fe-Cr binary alloys, for different thermo-mechanical treatments. Positron annihilation techniques, in particular lifetime technique, are used extensively. The other techniques are used either to corroborate the observations from positron techniques or to find out the relation of corresponding parameters with positron annihilation characteristics, so that they can be used conjunctively to understand the microstructural changes in the materials better.

2.9 REFERECES

---

[1] R. Krause-Rehberg, H. S. Leipner, Positron annihilation in semiconductors: Defect studies, Springer-Verlag, Berlin, 1998.

[2] P. Hautojarvi, A. Vehanen, Positrons in Solids, Spinger-Verlag, Berlin, 1979.

[3] J. M. Campillo Robles, E. Ogando, F. Plazaola, J. Phys.: Condens Matter **19**, 176222 (2007).

[4] Meenakshi Bhatia, G. Vasanthi, M.Sc project report, University of Kota and Pondicherry University, (2009) (unpublished data).

[5] J. Kansy, Nucl. Instr. Methods A **374**, 235 (1996).

[6] M. J. Puska, R. M. Nieminen, Rev. Mod. Phys. **66**, 841 (1994).

[7] M. J. Puska, M. Sob, G. Brauer, T. Korhonen, Phys. Rev. B **49** 00947 (1994).

[8] K. G. Lynn, J. R. MacDonald, R. A. Boie, L. C. Feldman, J. D. Gabbe, M. F. Robbins, E. Bonderup, and J. Golovchenko, Phys. Rev. Lett. **38**, 241 (1977).

[9] P. Asoka-Kumar, M. Alatolo, V. J. Ghosh, A. C. Kruseman, B. Nielsen and K. G. Lynn, Phys. Rev. Lett. **77**, 2097 (1996).

[10] Janice Klansky, Characterization of Materials, edited by Elton N. Kaufmann, Wiley-interscience (2003).

[11] Baldev Raj, V. Moorthy, T. Jayakumar, K. Bhanu sankara Rao, Int. Mater. Rev. **48**, 273 (2004).

[12] B. P. C. Rao, T. Jayakumar, D.K. Bhattacharya and Baldev Raj, J. Pure Appl. Ultrason. **25**, 53 (1993).

Chapter - 3

Dependence of Positron Lifetime on Evolution of Precipitates in F/M Steels: Studies on EUROFER97

3.0 PREAMBLE

This chapter aims at investigating and establishing direct dependence of positron lifetime on precipitate-matrix interface area which can be estimated from the precipitate size and their number density. EUROFER97 being a typical system in the class of high chromium (9-12 wt%) ferritic/martensitic steels, the trend in results, with regard to precipitate evolution, can be considered as representative for high chromium ferritic/martensitic steels.

3.1 INTRODUCTION

The importance of distribution of different precipitates for a stable microstructure in ferritic/martensitic steels was discussed in the chapter-1. The effect of irradiation and aging on the precipitates [1, 2, 3, 4, 5] and stabilization of microstructure by addition of carbide forming elements such as Nb, Ta, V and Ti is also discussed. Suitable technique should be employed to understand the detailed microstructures effectively and reasonably faster.

Transmission electron microscopy (TEM) is one of the established techniques to characterize precipitates as low as a few nanometers in size. Using TEM it is possible to find the structural details, size and chemical nature of precipitates. Atom Probe

Tomography (APT) is also emerging as a powerful technique to investigate chemical composition of nano-precipitates in materials [6, 7, 8]. An advantage of APT technique is that it can probe three dimensional distributions of atoms. While ATP can find size, three dimensional shapes and chemical nature of precipitates, it fails to identify the crystal structure of precipitates. However, both TEM and APT require laborious sample preparation and time consuming experiments and analysis. During extensive study of varying microstructural changes, time and labor impose constraints on the number of samples that can be investigated. Indicative changes from other simple experiments could provide valuable information before performing detailed microstructural studies using the above techniques.

Positron annihilation spectroscopy (PAS) can serve the purpose of probing indicative changes in microstructure, especially precipitation processes. Positron annihilation, having sensitivity to the variation in defects that are associated with changes in the microstructure, can serve as an effective tool in finding out microstructural changes. The current chapter aims at correlating positron annihilation lifetime and precipitation stages to evidence the applicability of the technique to identify the microstructural changes in ferritic steels. The unique sensitivity of positron annihilation spectroscopy for fine microstructural changes, in term of annealing out of atomistic defects, at lower temperatures will also be brought out.

3.2 EUROFER97 STEEL

EUROFER97 is a Reduced Activation Ferritic/Martensitic (RAFM) steel whose composition is drawn from modified 9Cr-1Mo steel by replacing Mo, Nb by W, Ta respectively and reducing N. The resultant composition, after irradiation, takes around 100 years to be classified as low level waste unlike Mo, Nb containing steels ferritic steels or SS316 whose time scales of decay are more than 10^4 years [9].

The composition of EUROFER97, both specified and the actual sample measured by Direct Reading Optical Emission Spectroscopy (DROES) is shown in Table-3.1. Given the limitations of DROES regarding quantifying N, O concentrations and the main alloying elements being found as specified, it is considered as an exact composition of EUROFER97. As-received samples are in normalized and tempered condition. The samples are of dimensions 0.15 x 0.8 x 2.0 cm^3.

Table-3.1 : Specified limits and the chemical composition of EUROFER97 sample.

Element	**Concentration (wt %)** (specified)	**Concentration (wt %)** (as measured by DROES)
Cr	8.50 - 9.50	8.70 (0.05)
C	0.09 - 0.12	0.082 (0.005)
Mn	0.20 - 0.60	0.50 (0.02)
V	0.15 - 0.25	0.187 (0.005)
W	1.0 - 1.2	1.04 (0.05)
Ta	0.05 - 0.09	-
P	<0.005	<0.007
S	<0.005	<0.007
N	0.015 - 0.045	-
O	<0.01	-
Nb	<0.001	<0.030
Mo	<0.005	<0.005
Ni	<0.005	0.1 (0.02)
Cu	<0.005	<0.05
Al	<0.05	<0.010
Si	<0.05	<0.2
Co	<0.005	<0.014 (0.005)

3.3 EXPERIMENTAL PROCEDURE

Positron lifetime studies are carried out as a function of heat treatment to understand microstructural evolution as a function of temperature. The results are substantiated with Transmission Electron Microscopy (TEM) analysis and Coincidence Doppler Broadening Spectroscopy (CDB). Vickers hardness measurements at representative temperatures have also been carried out.

3.3.1 Heat treatment

Normalized samples

As-received samples are mechanically polished to have smooth surface and to remove any contamination on the surface. These samples are normalized by heat treating at 1273 ± 5 K for 2 h in quartz tube connected to dynamic vacuum. The samples are air-quenched by cooling the quartz tube outside the furnace.

Normalized samples were subjected to isochronal heat treatment from 300 K to 1273 K in steps of 50 K with a holding time of 1 h in a vacuum, followed by cooling outside the furnace similar to the procedure adopted for normalization. After heat treatment, it is expected that the microstructure existing at holding temperature (below lower critical temperature, $Ac_1 \approx 1123$ K) is retained at room temperature. Above Ac1 temperature, the differences brought out by cooling are discussed. No further polishing has been carried out after heat treating the samples.

Normalized and deformed samples

A set of samples in normalized condition, mentioned as above, were 10% cold worked to introduce more nucleation sites, in particular dislocations. Positron lifetime studies alone were carried out on these samples with isochronal heat treatments as mentioned above.

3.3.2 Experimental details

Positron lifetime measurements were carried out at room temperature with a fast-fast coincidence lifetime spectrometer having a time resolution of 260 ps (FWHM). Source lifetime and its intensity were measured using annealed Fe as reference and these were taken into account while analyzing the lifetime spectra of actual samples. For each measurement, more than 2 x 10^6 counts have been collected. Accumulated lifetime spectra were analyzed using LT program [10].

CDB measurements were carried at treatment temperatures of 323 K, 723 K and 923 K. Annealed Fe sample was used as a reference sample for the ratio curves. To determine the possible extent of errors due to variations in detector parameters between measurements and during measurements, repeat measurements on annealed Fe samples were carried between EUROFER97 measurements. One such spectrum was shown in ratio curves. About 3 x 10^7 counts were accumulated for each spectrum. The data was analysed by extracting coincident counts and area normalizing for counts within ±10 keV from 511 keV. Ratio curves were obtained by taking ratio of counts of corresponding energies (channels). Annealed Fe spectrum was taken as a reference for obtaining ratio curves.

Transmission electron microscopy studies were carried out on as-prepared (normalized) sample and samples treated at 773 K, 973 K and 1073 K. Analytical Transmission Electron Microscopy (ATEM), Philips CM 200 microscope, with operating voltage of 200 kV was used for analyzing the samples. Selected Area Diffraction (SAD) and Energy-dispersive X-ray spectroscopy (EDS) were used to identify the precipitates. The samples were studied in both thin foil method and carbon replica extraction method to find variations in dislocation concentrations and to quantify the size and density of precipitates. From carbon replica results, quantification of precipitate density and size distribution had been brought out to corroborate the lifetime results. Carbon replica samples are prepared by conventional metallographic methods to get polished surface followed by etching, carbon coating and film lifting with Vilella's reagent (1 g picric acid, 5 ml HCl with 100 ml Ethanol). Sample for thin foil measurements were prepared by grinding and polishing, down to 30 µm. Final thinning was done using Ar-ion beam polishing at 3-5 kV/20-40 mA and a grazing incidence of 3° with respect to the sample surface.

3.4 RESULTS

3.4.1 Normalized samples

The observed lifetime variation in EUROFER97 steel as a function of treatment temperature is shown in Figure-3.1. As can be seen, three distinct stages of microstructural changes are seen viz., lifetime decreases from initial value to a lower value from room temperature until 773 K, an increase and decrease during 773 K–1123 K and finally a steep increase beyond 1123 K.

Corresponding to initial normalized sample, the positron lifetime value is 133 ps, which is higher than the lifetime value in defect free coarse grained (> 10 µm) pure Fe [11] and Fe-9Cr binary alloy [12] i.e. 108 ± 2 ps. Hence, it is evident that there exists open volume defects in the normalized sample. The exact nature of defects responsible for positron trapping is not clear. In order to identify possible open volume defects responsible for this higher lifetime, the observations from TEM micrographs could be useful to some extent.

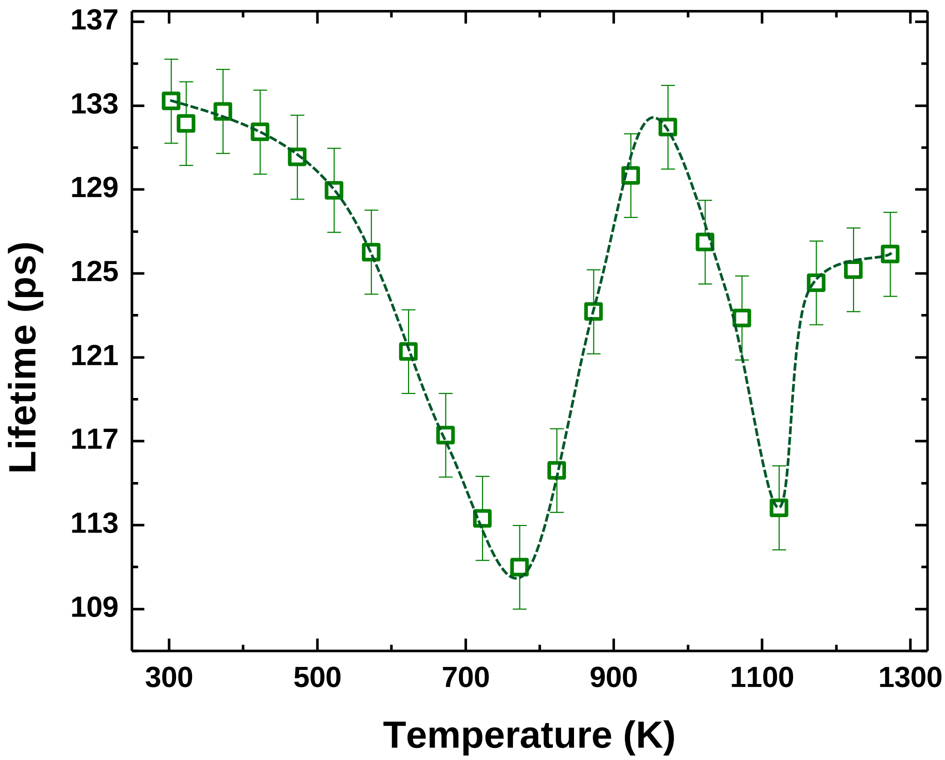

Figure-3.1: Positron lifetime as a function of treatment temperature in normalized sample. Decrease in lifetime during 300 K-773 K corresponds to annealing of quenched-in defects. Increase and decrease in lifetime between 773 K and 1123 K is due to precipitate evolution and increase in lifetime above 1123 K is due to martensitic phase formation. The line through the data points is just a guide to the eye.

The microstructure of normalized sample is complete martensite with typical lath microstructure of martensitic steels. The TEM micrographs are shown in Figure-3.2 and Figure-3.3. The micrograph of the lath structure is shown in Figure-3.2(a). The measured average lath size is 0.244 ± 0.032 µm. The microstructure includes high concentration of dislocations randomly oriented, which is another common feature of martensitic steels. Apart from the characteristic features of martensitic phase, a few coarse carbide precipitates of type $M_{23}C_6$ and MX are observed (Figure-3.2(b)). These are believed to be undissolved precipitates during normalization. But, the number density and hence, the volume fraction are very small. Figure-3.3 shows the representative Cr rich $M_{23}C_6$ precipitate and Ta rich carbide along with corresponding SAD patterns and EDS.

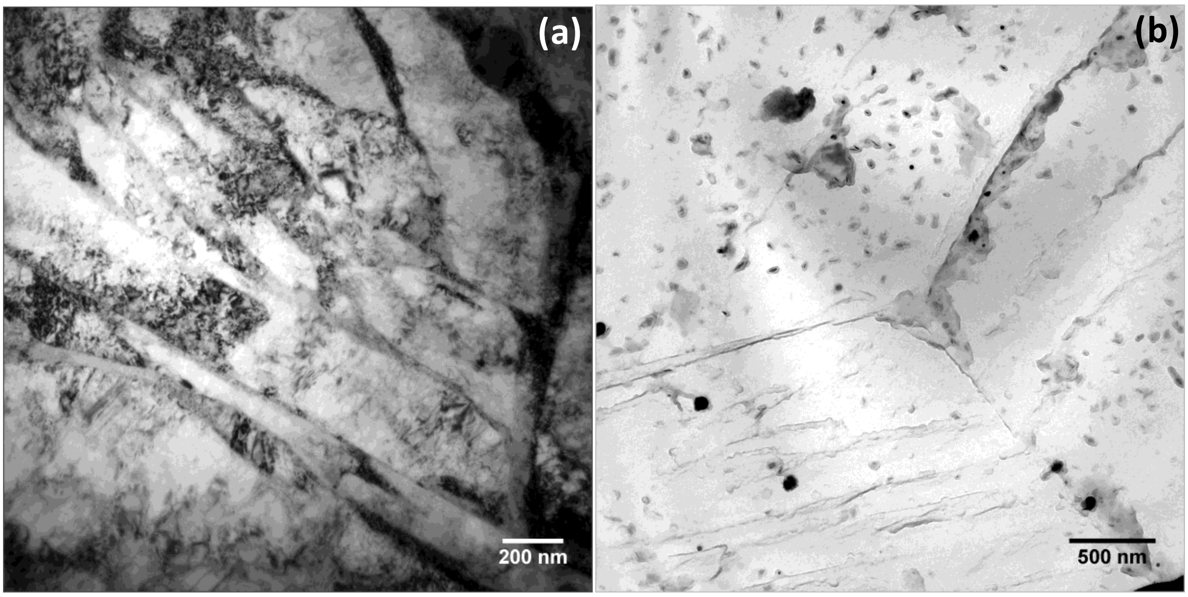

Figure-3.2: (a) TEM micrograph of normalized sample with lath structure and dense dislocations. This micrograph is taken using thin foil method. The average lath size is 0.244 ± 0.032 µm. (b) micrograph taken using carbon replica extraction method. A few precipitates can be seen in the micrograph. They are identified to be $M_{23}C_6$ *and TaC precipitates.*

The Vickers hardness value of normalized steel is measured as 490 ± 15 VHN. This value is relatively larger as compared to literature value of 425 VHN [13]. This could be either due to difference in mass of samples that are heat treated (15 mm rods in the case of [13]) that could alter the rate of cooling or due to the type of hardness technique used (macrohardness in the case of [13]). However, the hardness variation trend as a function of temperature is of prime interest.

The TEM microstructural observation of normalized sample indicate a variety of defects associated with lath boundaries, grain boundaries, dislocations and precipitate-matrix interfaces that can act as possible open volume defects responsible for positron trapping. Further, previous work showed that carbon impurities as low as 50 ppm in pure Fe can bind vacancies to form vacancy-carbon complexes, which are stable up to 350 K [14]. EUROFER97 having carbon content of about 0.08 wt% (>4500 ppm) could also contribute to carbon-vacancy complexes.

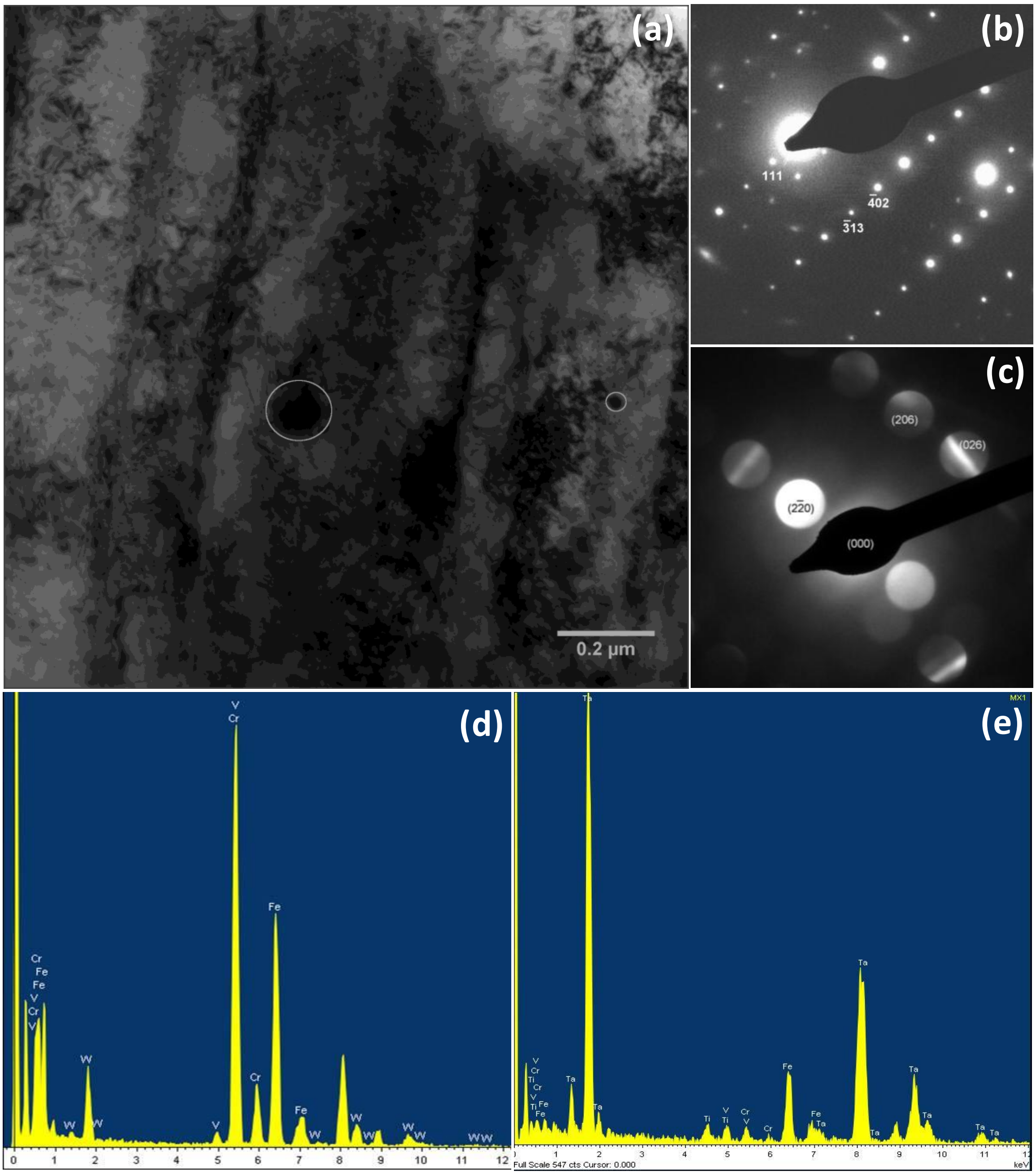

Figure-3.3: (a) TEM micrograph of normalized sample taken using thin foil mode. Precipitates are marked with circles. Larger one is $M_{23}C_6$ and smaller one is TaC precipitate. Diffraction patters of $M_{23}C_6$ (along [1 $\bar{3}$ 2] zone axis) and TaC (along [3 3 $\bar{1}$] zone axis) precipitates are shown in (b) and (c), respectively. Corresponding ED spectra of $M_{23}C_6$ and TaC precipitates are presented in (d) and (e), respectively. $M_{23}C_6$ found to be rich in Cr.

Also, the nature of positron trapping in dislocations is a subject still evoking continued interest [15, 16, 17, 18]. These studies suggest that dislocations alone cannot explain lifetime greater than 121 ps. Hence, vacancies trapped at dislocations also need to be considered. The resultant lifetime of vacancy trapped at dislocation, in Fe matrix, is found 150 ps [19]. The vacancies available for the formation of these complexes are expected to be quenched-in vacancies during cooling. The above mentioned possible defects are rationalized and a few will be eliminated with respect to variation in lifetime and observations from micrographs corresponding to the subsequent treatment at 773 K. Out of the listed possible open volume defects, precipitate-matrix interfaces can be neglected as they are very few in number per unit area and they are well separated (Figure-3.2(b)) with relative to diffusion length of positrons in metals and alloys i.e. 100 nm. Hence, the contribution from these precipitates is negligible. Similarly, the prior austenite grain size is greater than 12 μm (Figure-3.4) ruling out the possibility of contribution by significant fraction of positrons annihilating at grain boundaries due to trapping.

The positron lifetime gradually decreases with the increase of treatment temperature up to 773 K (Figure-3.1). This will strengthen the above arguments that existing precipitates and grain boundaries are not responsible significantly for higher lifetime observed in normalized sample. It is because the precipitates retained same despite decrease in lifetime after 773 K treatment. TEM micrographs at 773 K showed no change in lath structure (Figure-3.6). Hence, the contribution from lath boundaries is also seemed not responsible for higher lifetime in normalized sample. It is reported previously that the vacancy-carbon complexes are unstable above 550 K in α-iron [14, 20]. However, there are various other solute atoms in EUROFER97 to prevent a definite conclusion regarding the stability of carbon-vacancy complex above 550 K.

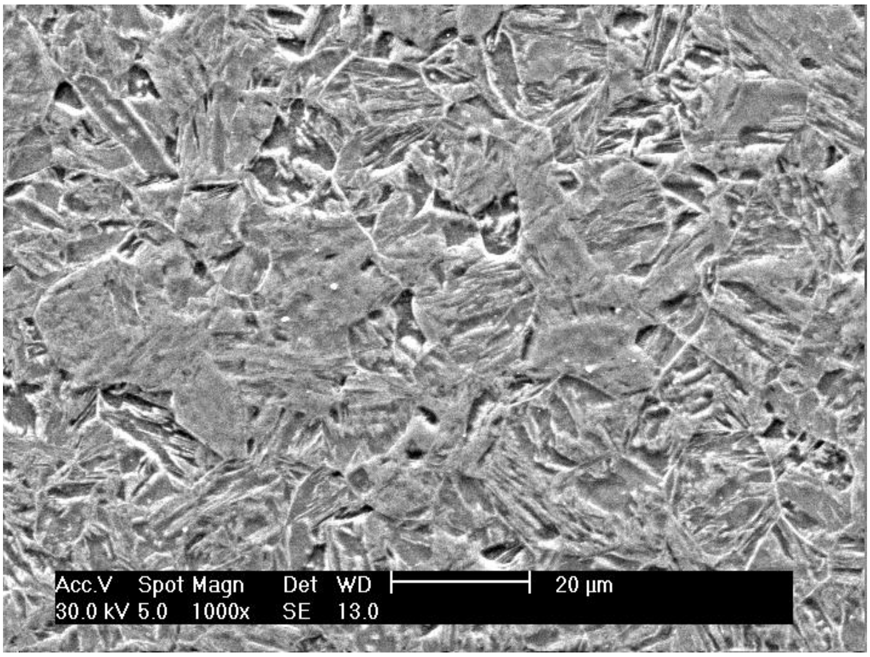

Figure-3.4: SEM micrograph of normalized sample with prior austenite grain boundaries.

The exact nature of defects responsible for higher lifetime in normalized condition is rather difficult to establish. They could be dislocations or/and dislocations with decorated vacancies or/and vacancy-carbon complexes. The observations tend to indicate them as dislocations. The trend of positron lifetime decrease in cold-worked pure Fe also favors the consideration. Figure-3.5 shows the positron lifetime as a function of annealing temperature in pure Fe deformed by 20% cold-working. As can be seen, the observed higher lifetime of 155 ps retain upto 523 K and decreases beyond. However, lifetime retains greater than defect free bulk value upto 773 K. This clearly indicates that the reduction in the lifetime is not due to annealing out of vacancies or vacancy-carbon complexes (80 ppm carbon in the pure Fe sample), but, due to reduction in dislocations. Based on this evidence, the observed annealing stage seen in EUROFER97 (Figure-3.1) is attributed to dislocation annealing.

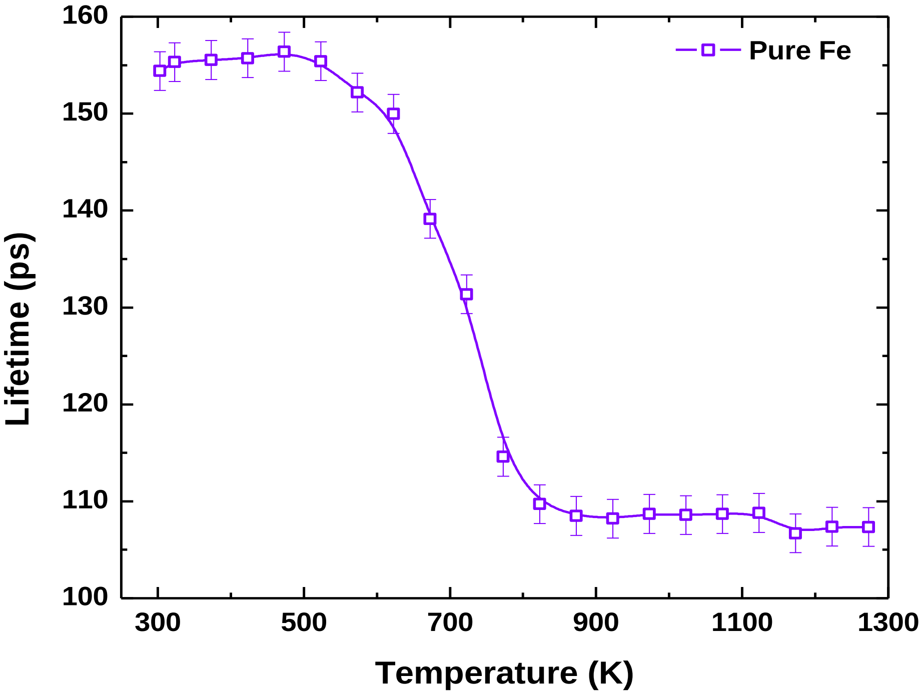

Figure-3.5: Positron lifetime as a function of annealing temperature in cold worked Fe sample. The lifetime retained higher value even beyond the temperature known for annealing out of carbon-vacancy complexes (550 K) [14], indicating the contribution of dislocations to higher lifetime.

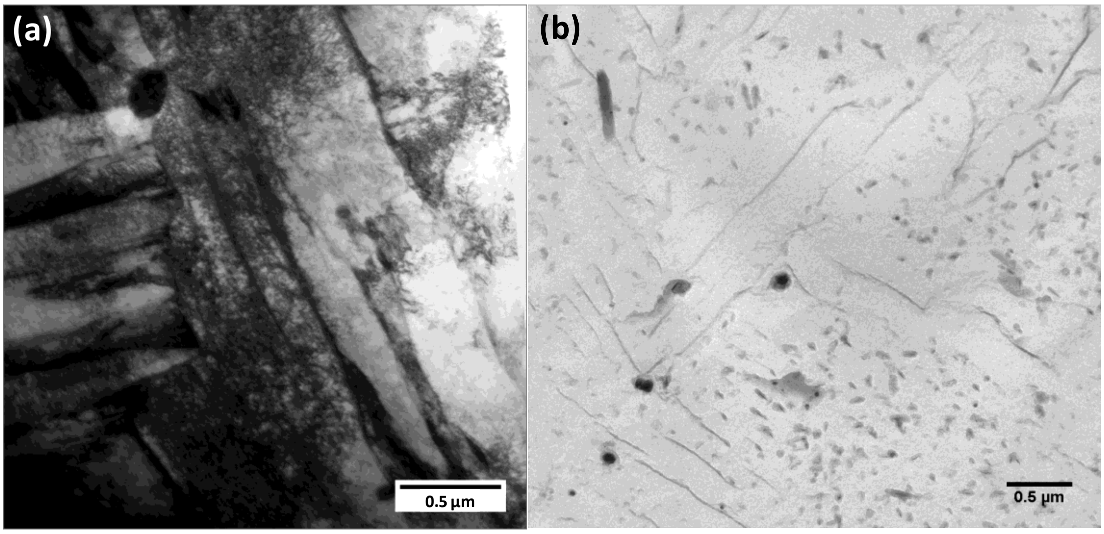

Figure-3.6: (a) TEM micrograph of 773 K annealed sample with lath structure. This micrograph is taken using thin foil method. The lath structure retained same as in the case of normalized sample. (b) Micrograph of precipitates observed in carbon replica. In addition to a few already existing $M_{23}C_6$ and MX precipitates, large number of M_2X precipitates observed.

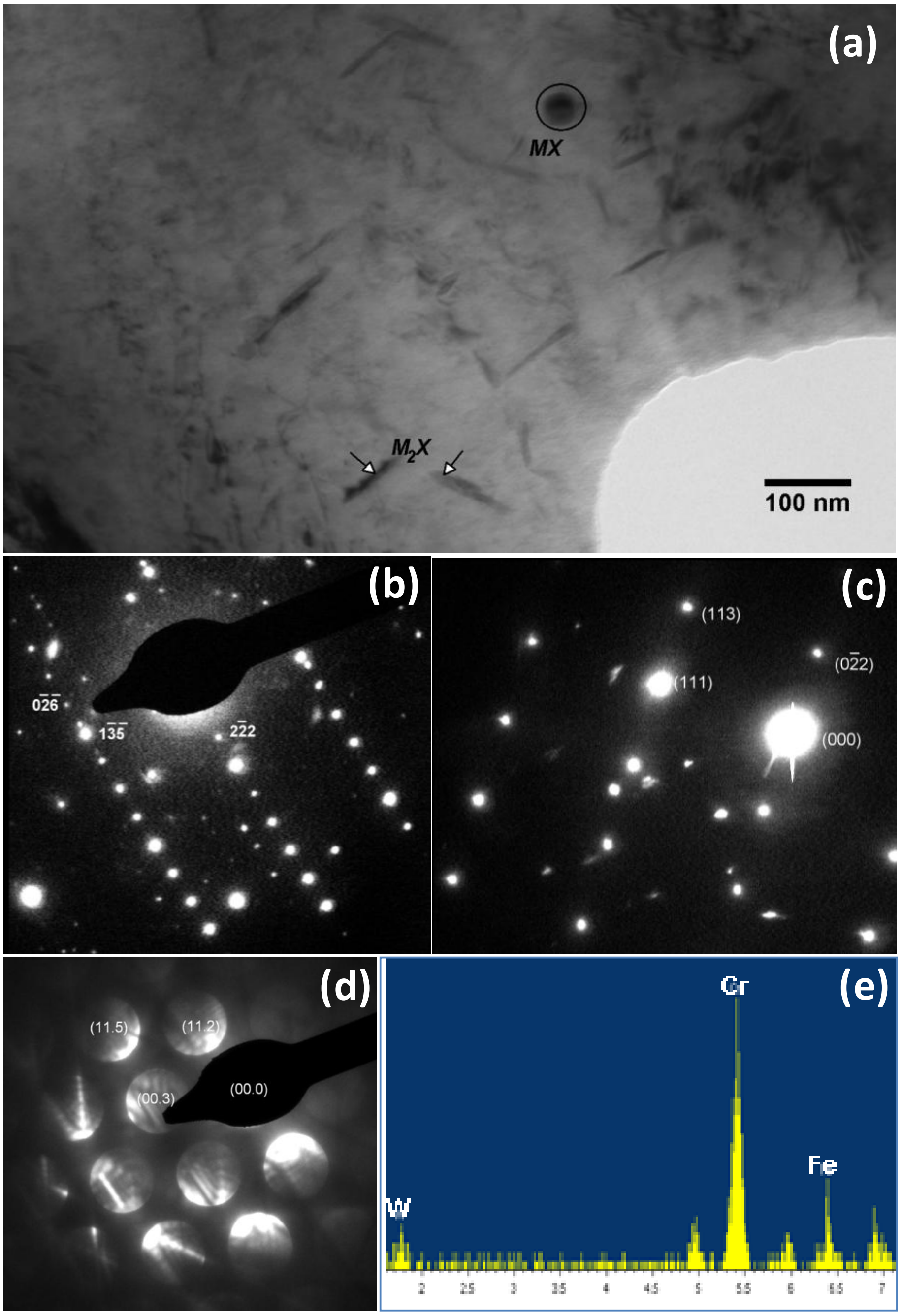

Figure-3.7: (a) TEM micrograph of 773 K annealed sample taken using thin foil mode. Needle like precipitates are M_2X type and circular one is MX precipitate. Diffraction patterns of (b) a representative $M_{23}C_6$ along $[\bar{4}\ \bar{3}\ 1]$ *zone axi. (c) a MX precipitate in* $[1\ \bar{1}\ 0]$ *zone axis (d) a M_2X precipitate in* $[1\ \bar{1}\ 0\ 0]$ *zone axis and (e) ED spectrum of a M_2X precipitate showing enrichment of Cr.*

Heat treatment up to 773 K did not change the lath structure (Figure-3.6(a), but only formation of additional very fine needle like precipitates (Figure-3.6(b) and

Figure-3.7(a)). These precipitates are identified to be M_2X precipitates, where M represents metal and X represent C, N. Formation of M_2X precipitates at low temperature is known previously [21]. These precipitates are identified to nucleate on dislocation. These precipitates are, in general, known to be high Cr and high N in composition [1].

Beyond 773 K lifetime increased (Figure-3.1) indicating an increase in open volume defects. The increase in lifetime continues upto 973 K and beyond this, it decreases upto temperature less than Ac_1. Martensitic phase is known to be stable up to 773 K in modified 9Cr-1Mo martensitic steel [22]. Hardness also did not show any change from normalized condition until 773 K (Figure-3.8). This is consistent with previous report [13]. At temperatures above 773 K, the transformation of martensite to ferrite with lath coarsening and growth of precipitates start taking place.

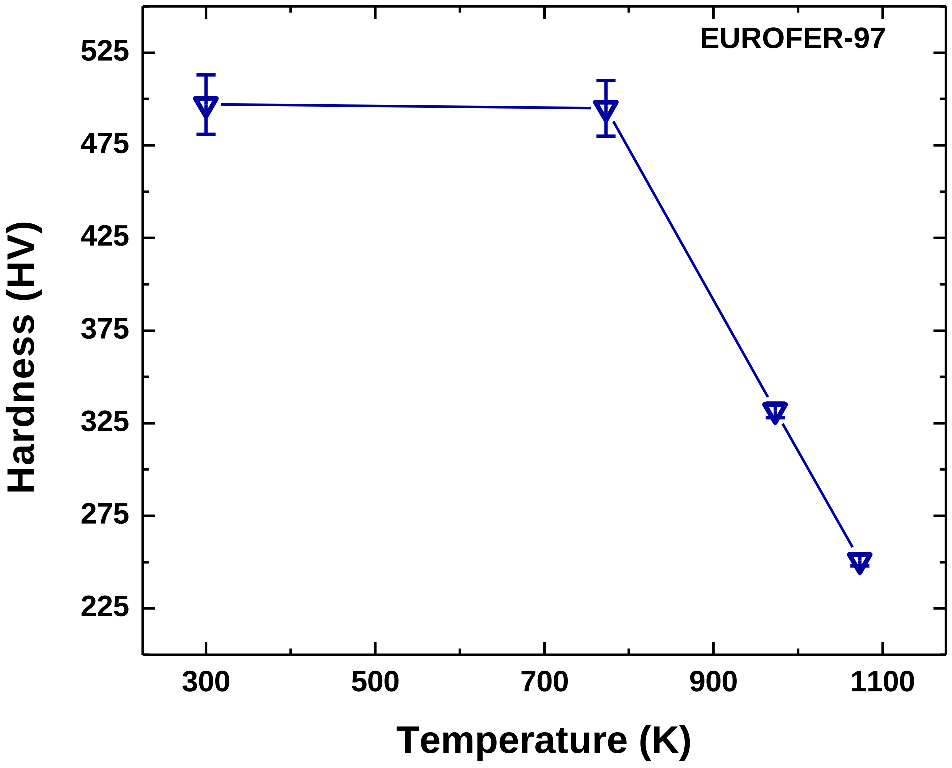

Figure-3.8: Vickers hardness of EUROFER97 normalized sample treated at different temperatures. The hardness did not vary until 773 K and decreased linearly at higher temperatures. This is consistent with previous observations [13].

Beyond 773 K, the martensite structure transforms to ferrite and precipitate start growing by accumulation of C which is above the solubility limit in the matrix. These two, though look different, are interdependent as martensite turns ferrite by carbon elimination from matrix by carbides formation. It is also known that the M_2X precipitates formed at low temperatures gradually turns to $M_{23}C_6$ as alloying elements diffuse into these precipitates [21]. The growth process of these precipitates can be found from increase in positron lifetime. Though the coarsening at the expense of small precipitates also takes place, it is not a dominant process as compared to growth process. This can be seen explicitly by quantifying the volume fraction increase from carbon replica extracted micrographs. The microstructure of 973 K heat treated sample studied by thin foil method is shown in Figure-3.9(a) and the precipitates extracted by carbon replica are shown in Figure-3.9(b). The formation of sub-grains due to recovery of martensite and growth of $M_{23}C_6$ precipitates cab be seen. Hence, the growth dominated precipitation is responsible for the increase in positron lifetime. A few M_2X precipitates are also present in this sample.

Beyond 973 K, lifetime starts decreasing (Figure-3.1), indicating the decrease of open volume defects. TEM observations of sample treated at 1073 K indicate the extensive formation of sub-grains due to high recovery rate (Figure-3.10(a)) and coarse $M_{23}C_6$ carbides (Figure-3.10(b)). TEM micrographs of precipitate extracted carbon replica showed lower number density of carbides (as compared to 973 K treated sample) with larger size. This observation confirms that above 973 K, it is the coarsening dominated process as the number density decreases and the particle size increases significantly. During this process smaller precipitates dissolve and larger precipitates grow by diffusion of solute away from small precipitates to precipitates of larger size, due to relative concentration gradient of solute in the matrix. One more important observation seen when compared to 973 K sample is, in the case of 1073 K treated sample less volume fraction of precipitates are formed indicating high solubility of alloying elements, hence, dissolution of some of the precipitates.

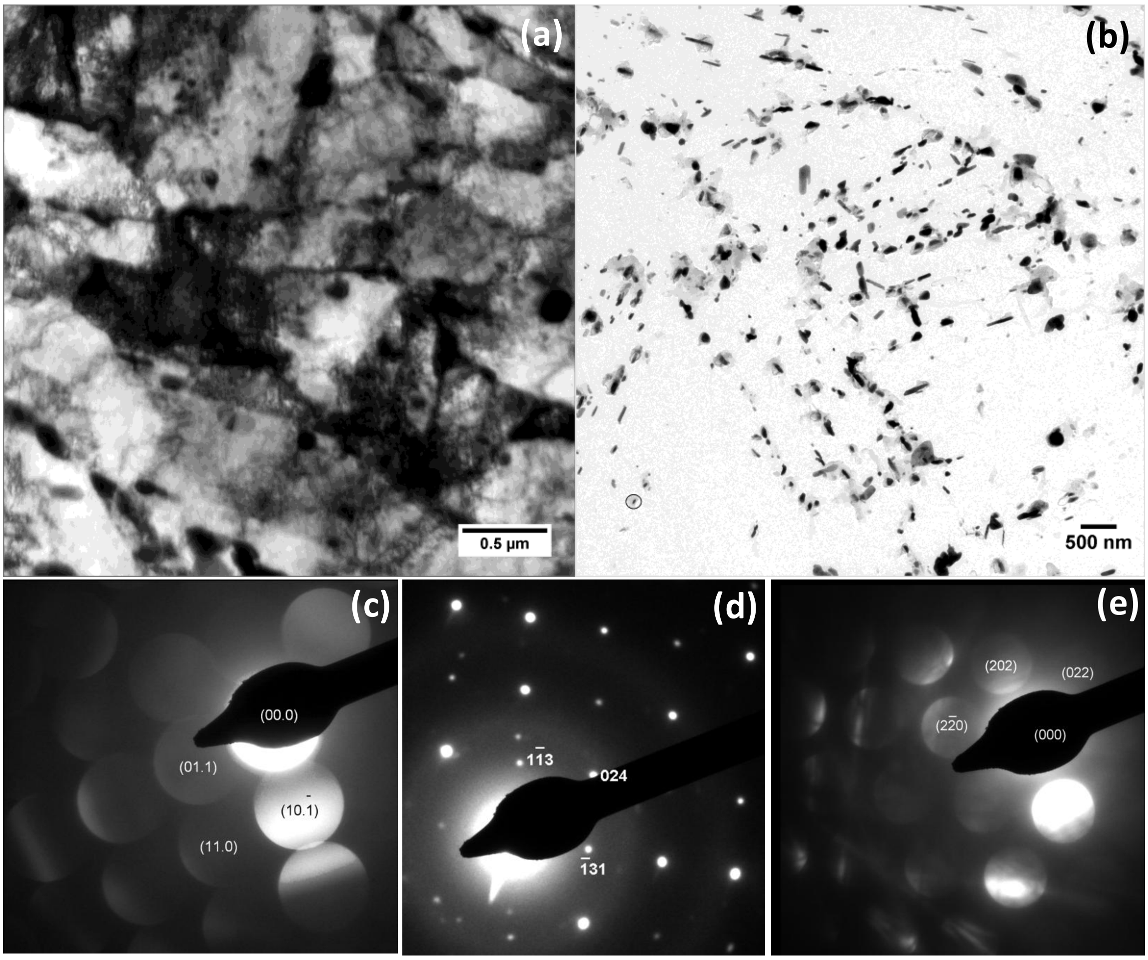

Figure-3.9: (a) TEM micrograph of sample treated at 973 K. Lath recovery and sub-grain formation can be found from the micrographs. (b) Distribution of precipitates, mainly $M_{23}C_6$*, found in carbon replica. (c) Diffraction pattern from a fine acicular* M_2X *carbide along* $[1\ \bar{1}\ 0\ 0]$ *zone axis. (d) Diffraction pattern of a* $M_{23}C_6$ *precipitate along* $[\bar{5}\ \bar{2}\ 1]$ *zone axis. (e) Diffraction pattern of a MX precipitate along* $[1\ 1\ \bar{1}]$ *zone axis.*

Hence, the present observation (Figure-3.1) showing the first stage which is the decrease of lifetime as a function of temperature until 773 K is due to annealing of one or more of dislocations, dislocations decorated with vacancies, vacancy-carbon complexes. The second stage, increase and decrease between 773 K and 1123 K is due to growth and coarsening of precipitates, with the transition from growth to coarsening domination around 973 K. The third stage i.e. increase in lifetime beyond 1123 K is a mere reproduction of initial microstructure due to martensite formation.

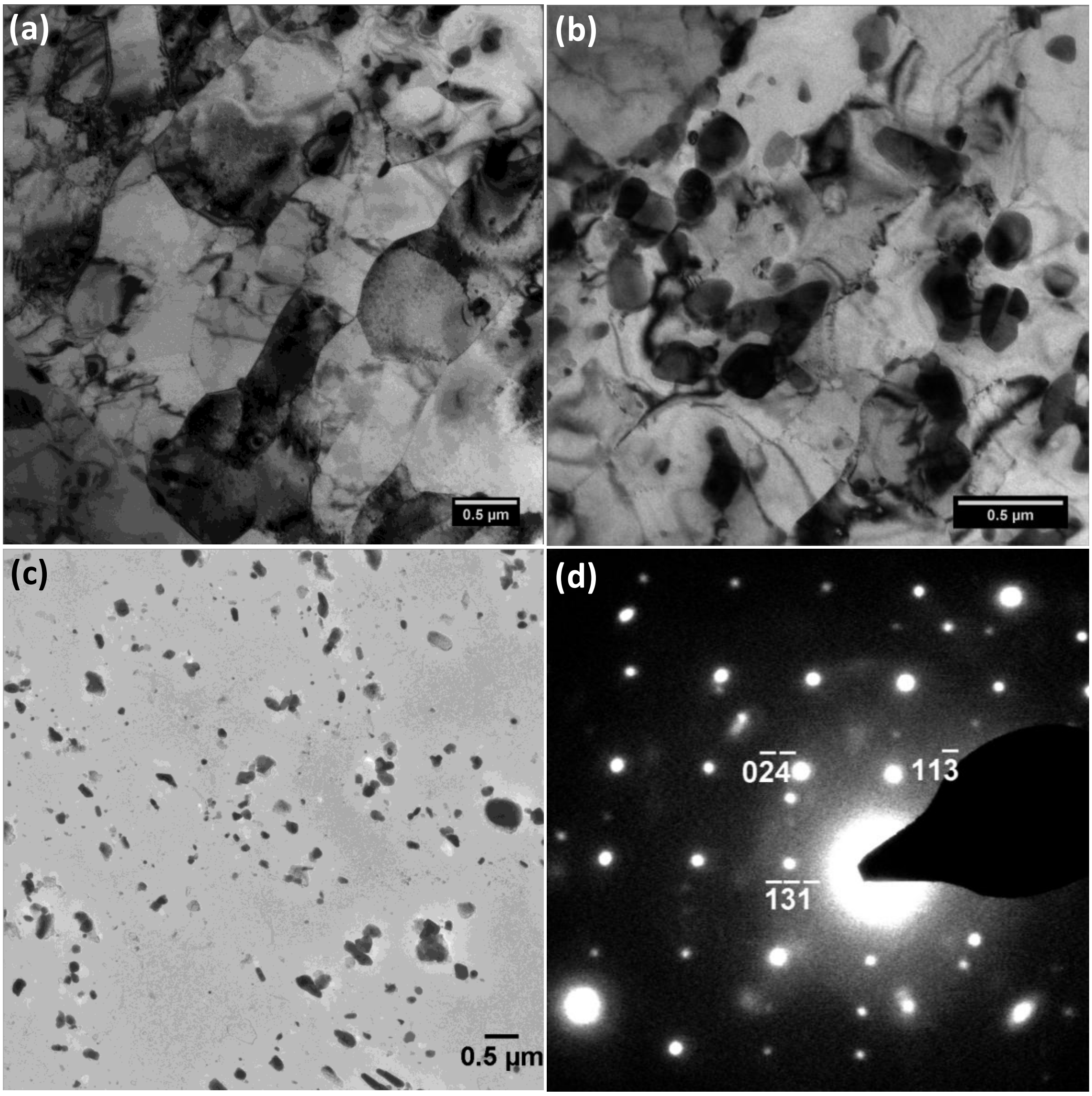

Figure-3.10: TEM micrograph of sample treated at 1073 K. (a) Extensive sub-grain formation can be found from the micrographs. (b) Coarse precipitates observed. (c) Precipitate distribution found in micrograph taken using carbon replica. (d) Diffraction pattern of $M_{23}C_6$ *precipitate along* [5 $\bar{2}$ 1] *zone axis.*

The quantified number density and particle size of precipitates obtained from TEM micrographs of carbon replica are shown in Figure-3.11. To quantify the size of precipitates, the projected area is measured and diameter of an equivalent circle of same area is taken as particle size.

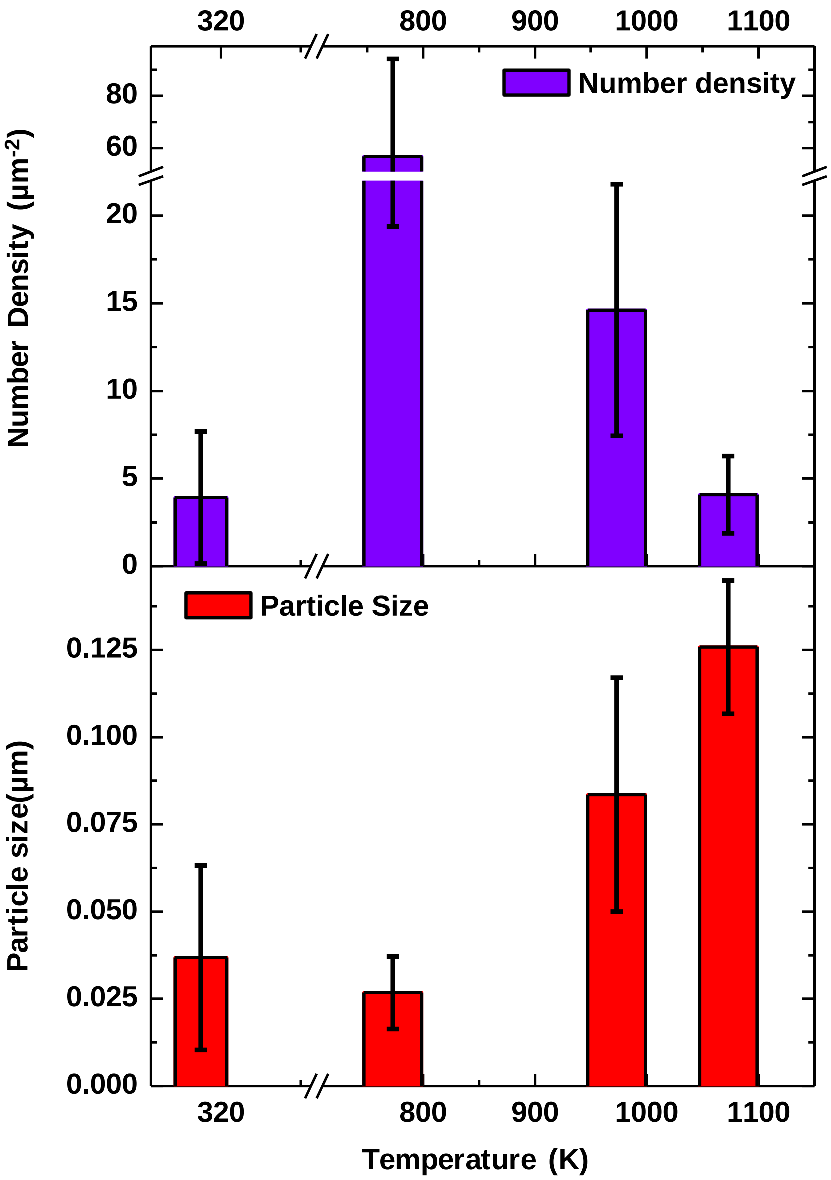

Figure-3.11: Average particle size and corresponding number density quantified from carbon replica as a function of treatment temperature. The size of particle is the diameter of equivalent circle to the projected area of precipitate.

From the particle size and number density, the surface area of precipitate-matrix interface and volume fraction are calculated and plotted along with the lifetime in the temperature zone corresponding to the precipitation (Figure-3.12).

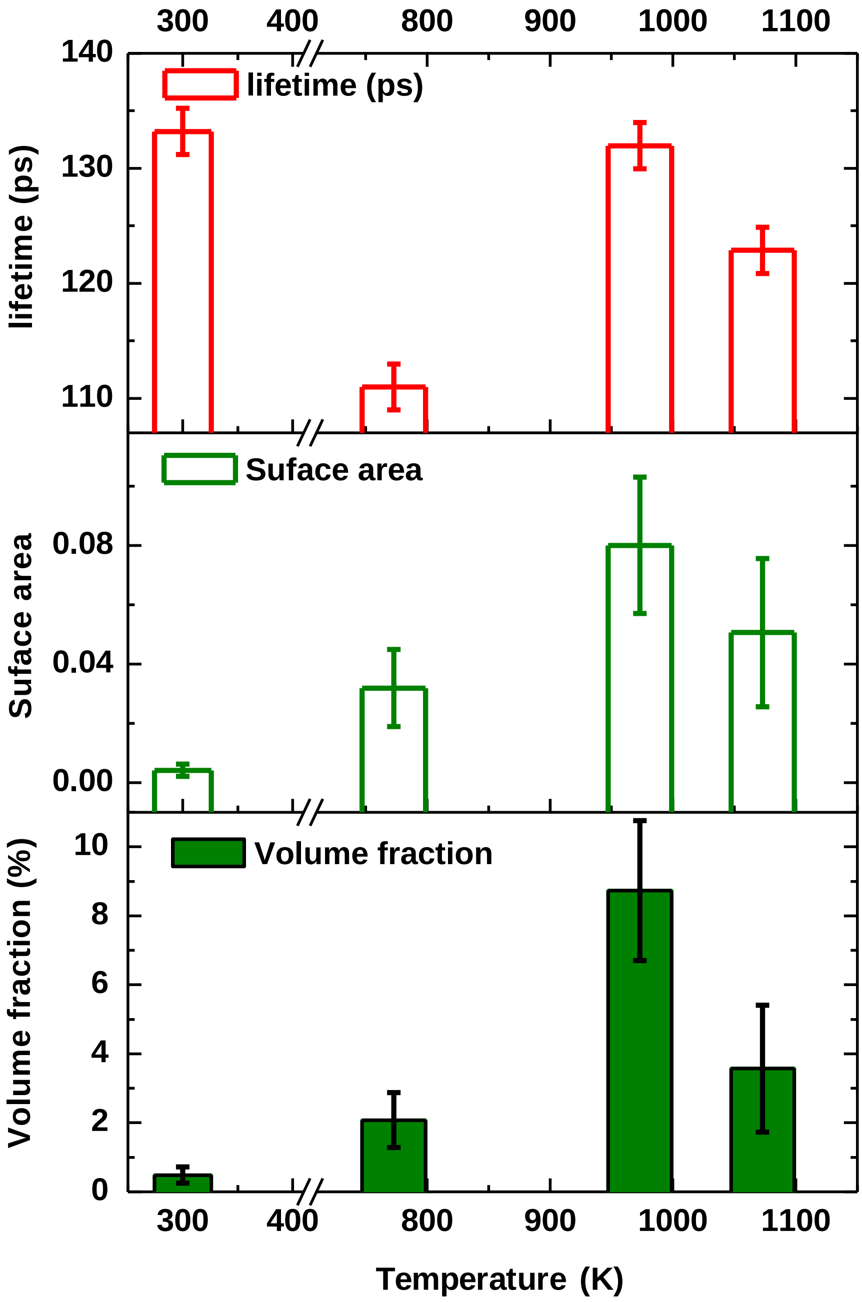

Figure-3.12: Volume fraction and surface area of precipitates calculated from particle size and number density. Corresponding lifetime plotted for comparison. Bar corresponding to 300 K is normalized sample in which precipitate number density is very small. However, the corresponding higher lifetime is dominated by contribution from quenched-in open volume defects present. Correlation between precipitates and lifetime is found between 773 K and 1073 K.

The above results suggest the higher lifetime between 723 K and 1123 K is due to precipitation where the growth process is dominated below 973 K and coarsening dominated above. The major contribution to the increase in lifetime is from $M_{23}C_6$. This is because, the concentration of $M_{23}C_6$ is an order higher than other Ta, V rich carbides [5]. This fact will be explicitly proved in the next chapter by measuring lifetime in samples by varying other carbide forming elements.

Though it was considered that the precipitate-matrix interface defects are responsible for trapping of positrons and hence, the higher lifetime, the fact that it is not explicitly proved whether the higher lifetime is due to annihilation at the interface defects or annihilation inside the precipitates. Both the interfacial area and volume fraction of precipitates show the same trend as positron lifetime (Figure-3.12). The coincidence Doppler broadening (CDB) results at 323 K (close to as-prepared condition), 723 K (quenched-in defect annealed condition) and 923 K (peak lifetime region corresponds to maximum precipitation) will be able to address this ambiguity. Before explaining the CDB results the following hypothesis should be mentioned about the nature of precipitates. The precipitates are considered to be free of vacancy defects within. The way the experimental synthesis of pure refractory metal carbides and nitrides carried is generally non-stoichiometric which will lead to large concentration of defects. It is known from the earlier theoretical calculations that the metal vacancies inside the transition-metal carbides and nitrides could trap positrons which lead to higher lifetime than defect-free lattice [23]. However, in this case, the precipitates are grown due to supersaturation of the carbon or due to the carbide forming elements. Since the precipitates are expected to grow atom by atom after nucleation, the consideration of perfect lattice seems valid. Figure-3.13 shows the ratio curves of CDB spectra of Fe and EUROFER97 steels with respect to annealed pure Fe. Figure-3.13(a) shows ratio curve of CDB spectrum of annealed Fe with respect to annealed Fe (repeat measurement) for showing the extent of experimental error. The marked region considered inappropriate for comparisons. Figure-3.13(b) shows the ratio curves of CDB spectra of EUROFER97 samples treated at 323 K, 723 K and 923 K.

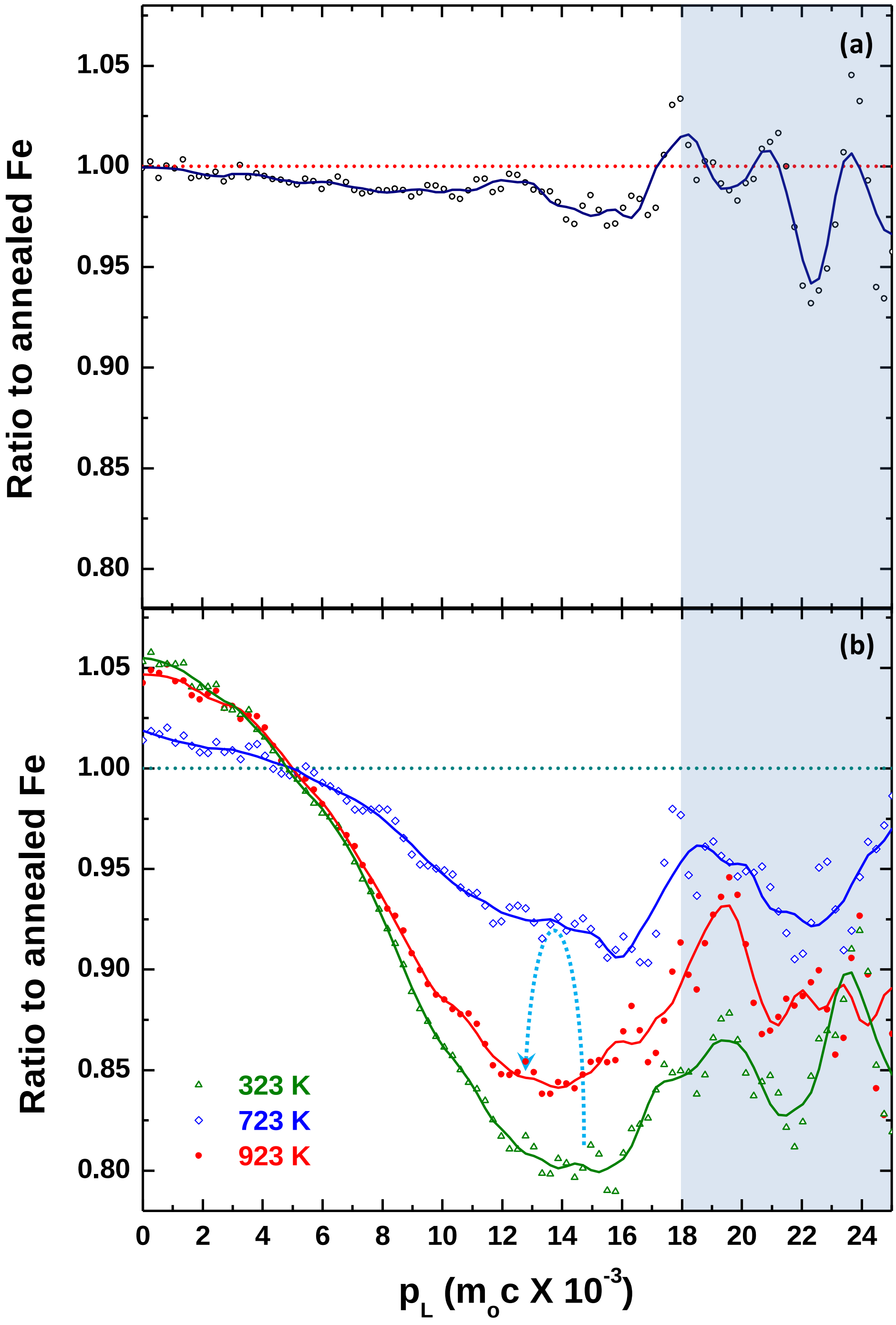

Figure-3.13: (a) Ratio curves for annealed Fe with annealed Fe (repeat measurement). It is shown to indicate the possible extent of errors in the measurements due to variation in detector and spectrometer parameters fluctuations. (b) Ratio curves of EUROFER97 samples treated at 323 K, 723 K and 923 K with respect to annealed Fe.

The high momentum component increased between 323 K and 723 K while the low momentum component decreased. Since, these variations are expected for the decrease in vacancy kind of defects and our previous discussions suggest that the vacancy kind of defects anneal out, the observations are consistent. Further, high momentum distribution decreased and low momentum distribution increased between 723 K and 923 K, indicating the changes are only due to increase in vacancy kind of defects. If the annihilation is inside the defect free precipitates, the variations in low momentum region are not expected to change between 773 K and 973 K treated samples. Also, the lifetime in defect free lattice of metal carbide is expected to be less than bulk lifetime value of corresponding transition metal [23] against the experimentally observed higher lifetime (Figure-3.1). These observations strengthen the argument that vacancy kind of defects concentration is solely responsible for the variation in lifetime. Considering the hypothesis that the precipitates are defect-free within, the precipitate-matrix interfaces are responsible for the changes.

3.4.2 Normalized and cold worked samples

In many alloys, deformation induced dislocations act as the nucleation sites for the formation of precipitates. As an example, in austenitic D9 steel TiC precipitates form during post-deformation heat treatment [24, 25]. The variation in positron lifetime with variation in percentage of cold-work was reported earlier [26, 27]. In the present study, the effect of cold-work on enhancement of concentration of the precipitate nucleation sites is studied in EUROFER97 steel. This study will strengthen our consideration regarding precipitate-matrix interfaces as trapping sites rather than the defect inside precipitates. Positron annihilation lifetime studies have been carried on 10% cold worked EUROFER97 sample to understand the effect of cold working on the number of nucleating sites for precipitation. As it will be the case, the additional 10% cold working increased the positron trapping vacancy kind of defects, dislocations, vacancies etc, hence the higher lifetime 150 ps (Figure-3.14). Same as in the case of normalized sample, these defects anneal out with treatment temperature till 773 K.

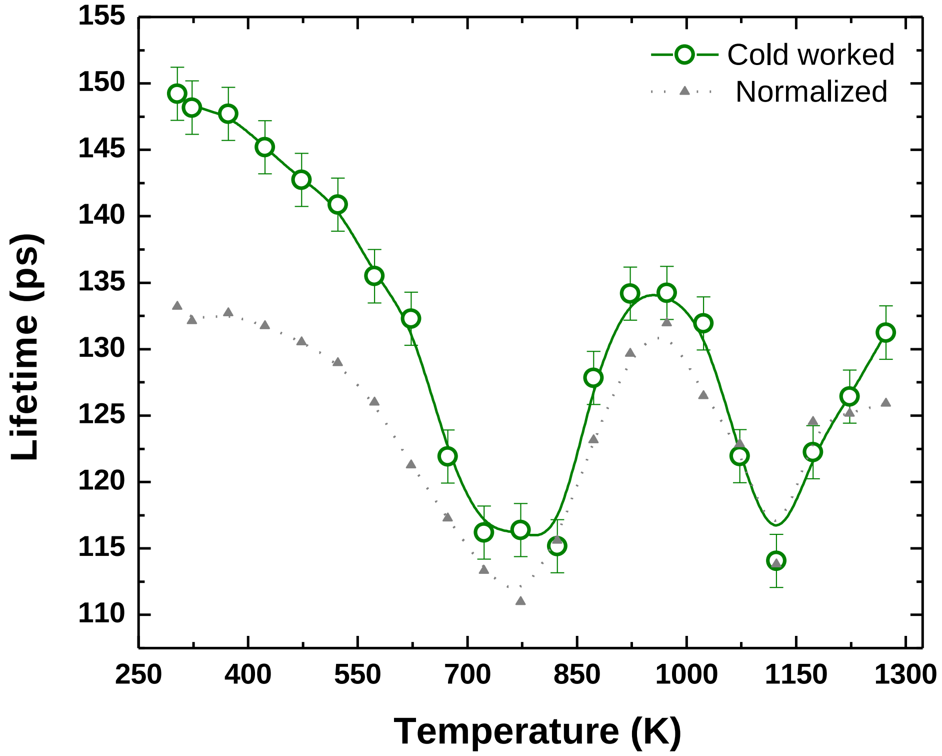

Figure-3.14: Positron lifetime as a function of treatment temperature in normalized and 10% cold worked EUROFER97 sample. For comparison, the lifetime results of normalized sample are also indicated.

The precipitation stages were also seen similar to normalized sample but with significant differences over the entire range between 823 K and 1073 K. Over this temperature range the lifetime in cold-worked samples is larger as compared to normalized samples (Figure-3.14). This indicates that the open volume defects are larger in this condition as compared to only normalized condition. Discussions in the previous part of the chapter proved that the defects are associated with the precipitate. The deformation induced defects acts as nucleation sites and the total volume fraction of precipitates, at a given temperature, depends on carbon content. Hence, the volume fraction of precipitates should be same in both the normalized sample and the cold-worked sample at a given temperature. Therefore, the precipitate number density should be higher in the case of deformed sample with relatively smaller average size. Because, the volume fraction remains same at a given temperature and both the precipitate number density and the lifetime increased, the defects responsible for higher lifetime must be precipitate-matrix interfaces.

3.5 SUMMARY

From the current study of PAS and electron microscopy on EUROFER97 steel the following observations are summarized.

- Positron lifetime studies on normalized EUROFER97 sample as a function of treatment temperature indicate distinct stages corresponding to quenched-in defect annealing (300 K–773 K), growth and coarsening of precipitates (773 K–1123 K) and martensitic phase formation above 1123 K.
- The quenched-in defects which anneal below 773 K are mostly dislocations and this argument is strengthened from the observations of lifetime in deformed pure iron.
- TEM studies of normalized sample showed presence of dense dislocations and a few TaC precipitates. Nucleation of M_2C precipitates are observed at 773 K. They are found to be Cr rich in nature. Growth of precipitates is observed in 973 K treated sample. Majority of the precipitates observed are $M_{23}C_6$ and the rest are VC, TaC and M_2C. Coarsening of the precipitates observed in 1073 K treated sample.
- From TEM micrographs of carbon replica, precipitate-matrix interfacial surface area and precipitate volume fraction are quantified. Positron lifetime values are consistent with both surface area and volume fraction.
- CDB studies confirmed that the higher lifetime between 773 K–1123 K is only due to vacancy kind of defects. Hypothesizing that vacancy defects will not be present inside precipitates in this case, the open volume defects are concluded as precipitate-matrix interfacial defects. Hence, relation between positron lifetime and precipitate-matrix interfacial defects in precipitate range is established.

- Lifetime variation in 10% cold-worked EUROFER97 sample suggests that the deformation increased the number of nucleation sites and hence, the precipitate density. It also strengthens the consideration of interfacial open volume defects as trapping centers.

3.6 REFERENCES

---

[1] Klueh, ORNL/TM-2044/176.

[2] Fujio Abe, Sci. Technol. Adv. Mater. **9**, 013002 (2008).

[3] Y. deCarlan, A. Alamo, M. H. Mathon, G. Geoffroy and A. Castaing, J. Nucl. Mater. **283-287**, 672 (2000).

[4] R. L. Klueh, J.M. Vitek, J. Nucl. Mater. **182**, 230 (1991).

[5] J. J. Kai, R. L. Klueh, J. Nucl. Mater. **230**, 116 (1996).

[6] T. F. Kelly and M. K. Miller, Rev. Sci. Instrum. **78**, 031101 (2007).

[7] C. A. Williams, E. A. Marquis, A. Cerezo, G. D.W. Smith, J. Nucl. Mater. **400**, 37 (2010).

[8] M.K. Miller , K.F. Russell, J. Nucl. Mater. **371**, 145 (2007).

[9] K. Seidel, R. A. Forrest, H. Freiesleben, V.D. Kovalchuk, D.V. Markovskij, D.V. Maximov, S. Unholzer, J. Nucl. Mater. **307-311**, 1037 (2002).

[10] J. Kansy, Nucl. Instr. Methods A **374**, 235 (1996).

[11] J. M. Campillo Robles, E Ogando, F. Plazaola, J. Phys.: Condens. Matter **19**, 176222 (2007).

[12] S. Hari Babu, R. Rajaraman, G. Amarendra, R. Govindaraj, N. P. Lalla, Arup Dasgupta, Gopal Bhalerao, C. S. Sundar, Philos. Mag. **92**, 2848 (2012).

[13] M. Rieth, M. Schirra, A. Falkenstein, P. Graf, S. Heger, H. Kemp, R. Lindau, H. Zimmermann, EUROFER97, Tensile, Charpy, Creep and Structural Test, FZKA 6911.

[14] P. Hautojarvi, J. Johansson, A. Vehanen, J. Yli-Kauppila, P. Moser, Phys. Rev. Lett. **44**, 1326 (1980).

[15] P. Hautojarvi, A. Vehanen, Appl. Phys. **11**, 192 (1976).

[16] L.C. Smedskjaer, M. Manninen, M.J. Fluss, J. Phys. F: Metal Phys. **10**, 223 (1980).

[17] K. Sato, T. Yoshiie, T. Ishizaki, Q. Xu, Phys. Rev. B **75**, 094109 (2007).

---

[18] L. Petrov, T. Troev, N. Nankov, E. Popov, J. Phys. Conf. Series **207**, 012037 (2010).

[19] C. Hidalgo, G. Gonzalez-Doncel, S. Linderoth, J.S. Juan, Phys. Rev. B **45**, 7017 (1992).

[20] A. Vehanen, P. Hautojarvi, J. Johansson, , J. Yli-Kauppila, P. Moser, Phys. Rev. B **25**, 762 (1982).

[21] Sung Ho Kim, Chang Hee Han, Woo-Seog Ryu, Solid State Phenomena **135**, 107 (2008).

[22] Wendell B. Jones, C. R. Hills, D. H. Polonis, Metall. Trans. A **22A**, 1049 (1991).

[23] M. J. Puska, M. Sob, G. Brauer, T. Korhonen Phys. Rev. B **49**, 00947 (1994).

[24] W. Kesternich, J. Nucl. Mater **127**, 153 (1985).

[25] W. Kesternich, D. Meertens, Acta metall. **34**,1071 (1986).

[26] R. Rajaraman, Padma Gopalan, B. Viswanathan, S. Venkadesan, J. Nucl. Mater. **217**, 325 (1994).

[27] Padma Gopalan, R. Rajaraman, B. Viswanathan, K.P. Gopinathan, S. Venkadesan, J. Nucl. Mater. **256**, 229 (1998).

Chapter - 4

Complementary Nature of Positron Annihilation Spectroscopy: Studies on Modified 9Cr-1Mo Steels

---

4.0 PREAMBLE

This chapter aims at demonstrating the complementary nature of Positron Annihilation Spectroscopy (PAS) as compared to ultrasonic velocity, hardness and X-ray diffraction techniques for probing microstructural changes in high chromium (9-12%) ferritic steels. It also presents the advantage of studying the microstructure of the steel by PAS in conjunction with ultrasonic velocity and hardness. Sensitivity of PAS to finer changes in the microstructure will be brought out.

4.1 INTRODUCTION

The prospect of using PAS as a Non-Destructive Evaluation (NDE) technique is quite promising due to its sensitivity and selectivity to vacancy kind of atomistic defects that are precursors to changes in microstructure and stresses during the usage of structural materials. PAS could probe the changes in microstructure and early stages of deformation in materials well before conventional NDE techniques could detect. Applicability of PAS in early stages of fatigue, deformation damage, hydrogen embrittlement, radiation damage, voids and bubble growth has been reviewed by Coleman [1].

Possibility of PAS to probe precipitate evolution in ferritic steels so as to use it as characterization tool during optimization of the steel treatment procedure is not studied explicitly. However, sensitivity of PAS for fine changes in microstructure is well known [2, 3, 4, 5, 6]. This chapter highlights the complementary information that PAS can provide about the microstructural changes due to various heat treatment procedures.

4.2 MODIFIED 9Cr-1Mo STEEL

9Cr-1Mo martensitic/ferritic steels are considered as candidate structural materials for high temperature applications in nuclear reactors. Compared to standard 9Cr-1Mo steels, modified 9Cr-1Mo steels have shown superior ultimate tensile strength and yield strength over a wide range of temperatures, 300-973 K [7]. Further, 9Cr-1Mo (both plain and modified) steels have yield strength higher than 304 stainless steel up to 973 K [7]. The aging between 663–823 K for 5000 h did not alter the strength and ductility of these steels as compared to unaged steels. Irradiation at 663 K causes an increase in the strength and ductility relative to unirradiated conditions. However, no change upon irradiation occurs above 723 K [8]. The addition of Nb and V in the modified 9Cr-1Mo steel favors the formation of finely distributed M(Nb,V)X(C,N) precipitates of the order of 10 nm in size, which are responsible for increasing the stability of the microstructure. Hence, it is a good candidate material as pressure vessel steel in very high temperature reactors (VHTR). The optimal properties have been identified with a tempered martensite condition resulting from austenitizing at approximately 1313 K for 1 h, followed by air cooling and subsequent tempering for 1 h at 1033 K [9]. The microstructural changes in modified 9Cr-1Mo steels have been well studied by many investigators using electron microscopy [7, 9, 10], ultrasonic velocity [11], magnetic techniques [12, 13]. Precipitation design studies for the creep strengthening of 9% Cr tempered martensitic steels have also been reported [14]. It has been found that a microstructure with dispersed fine MX precipitates, particularly carbides and nitrides of Nb, V, Ta and Ti, is stable against tensile creep at higher temperatures.

4.3 EXPERIMENTAL PROCEDURE

In the present study PAS, ultrasonic velocity, hardness and scanning electron microscopy were employed so as to probe various microstructural changes in modified 9Cr-1Mo steels brought about by different heat treatments. Positron lifetime studies alone were also carried out on plain 9Cr-1Mo steel samples, at representative temperatures, with similar treatments for comparison. Composition of the alloying elements (in wt %) in modified 9Cr-1Mo steel used in this study is given in Table-4.1. The chemical composition of plain 9Cr-1Mo steel is almost identical to shown in Table-4.1, except the absence of V and Nb.

Due to the similarity in chemical composition of modified 9Cr-1Mo steel and EUFROFER97 steel, the microstructural changes as a function of heat treatment are expected to be similar [9, 15].

Table-4.1 Chemical composition of modified 9Cr-1Mo steel

Element	**Cr**	**Mo**	**Mn**	**Si**	**V**	**Ni**	**Nb**
Wt%	8.5	0.95	0.40	0.25	0.22	0.20	0.08
Element	**C**	**N**	**Cu**	**S**	**P**	**Al**	**Fe**
Wt%	0.10	0.01	<0.006	<0.006	<0.006	<0.002	Balance

As-received samples are cut into (i) two pairs of samples (of size 6 x 8 x 1 mm^3) for positron lifetime measurements (ii) 20 samples (of size 30 x 15 x 13 m^3) for ultrasonic velocity and hardness measurements and (ii) 10 samples (of size 6 x 6 x 1 m^3) for scanning electron microscopy. Half of the samples in each group were used for studies with *normalized* condition and the rest for studies with *normalized and tempered* as initial condition.

4.3.1 Heat treatment

Normalized samples

After cutting, samples were normalized at 1313 K for 1 h. Pair of samples from first group were subjected to isochronal tempering treatment from 300 K to 1273 K in steps of 50 K with a holding time of 1 h in a vacuum of 10^{-6} Torr. After each treatment, positron lifetime measurements were carried out at room temperature.

Half of the samples from second group and third group were heat treated isochronally in steps of 50 K with a holding time of 1 h, cumulative, till the measurement temperature. For ultrasonic velocity and hardness, the measurements were conducted with heat treatment temperature intervals of 100 K. This identical heat treatment procedure for all the studies allows better comparison of these results with positron lifetime results. For SEM studies, the as-normalized sample, samples subsequently tempered till 373, 673, 873, 973 and 1073 K were used.

Normalized and tempered samples

The remaining samples of each group, after normalizing at 1313 K for 1 h, were tempered at 1033 K for 1 h. The resultant microstructure is tempered martensitic structure. Heat treatments similar to the previous case were carried between 300 K and 1273 K with a holding time of 1 h. For SEM studies, the normalized and tempered sample, samples subsequently aged till 923, 1023 and 1273 K were used.

4.3.2 Experimental details

Positron lifetime measurements were carried out at room temperature with a fast-fast coincidence lifetime spectrometer having a time resolution of 260 ps (FWHM). The acquired lifetime spectra were analyzed using LT program [16]. Only single lifetime was obtained over the entire treatment temperature range for all the measurements.

Positron Doppler broadening Measurements, Vickers microhardness and ultrasonic measurements were carried out at room temperatures, in the procedure explained in Chapter-2. Scanning electron microscopy was carried out using a Carl Zeiss FE SEM.

4.4 RESULTS

4.4.1 Normalized steel

The initial microstructure of normalized steels is expected to be martensitic with fine lath structure [9], similar to EUROFER97 results shown in the previous chapter. The same is observed in normalized sample (Figure-4.1). It consists of dispersed Nb rich precipitates which are spherical in shape. They are believed to be undissolved niobium carbide precipitates during treatment. Similar NbC precipitates undissolved during austenitization were reported earlier [9] and they are found to be advantageous to retard prior austenite grain growth during normalization.

The positron lifetime in normalized sample is 137 ± 2 ps (Figure-4.2). Similar to EUROFER97 case, this is higher than that of defect-free iron matrix. As rationalized in previous chapter, the positron annihilation sites responsible for higher lifetime are considered to be dislocations or/and vacancy decorated dislocations or/and vacancy-carbon complexes.

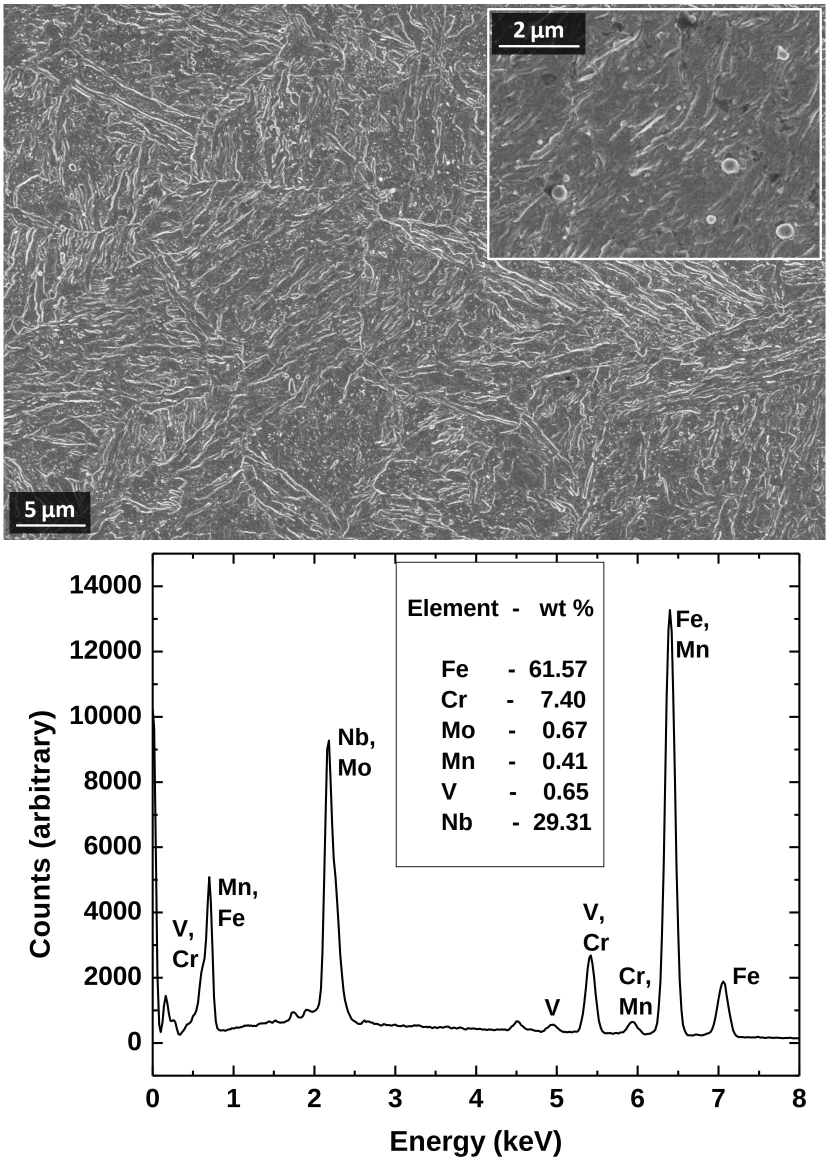

Figure-4.1: FESEM micrograph of normalized modified 9Cr-1Mo steel showing prioraustenite grain boundaries with lath structure inside. The circular precipitates shown in inset are Nb rich precipitates. The corresponding EDS spectrum for a representative Nb rich precipitate is shown. The chemical composition of precipitate is shown, indicating enrichment of Nb.

Lifetime decreased steeply till 673 K indicating annealing out of the quenched-in defects. By 773 K, lifetime started increasing indicating the formation of precipitates. Lifetime increases till 873 K indicating the growth of precipitates and then decrease till

1123 K indicating the coarsening of precipitation. Above 1123 K, the lifetime increases sharply as the structure results in martensite with quenched defects.

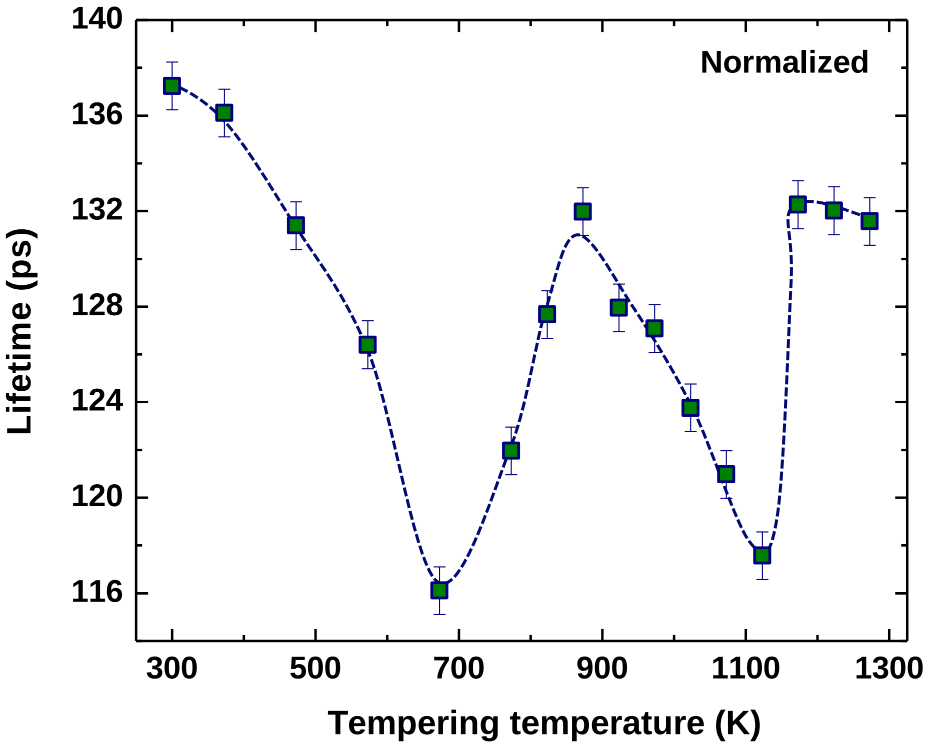

Figure-4.2: Positron lifetime as a function of tempering temperature in normalized modified 9Cr-1Mo steel sample. The increase in lifetime between 673 K-873 K indicates the growth dominated precipitation and the decrease between 873 K-1123 K indicate coarsening of precipitates. The line through the data points is a guide to the eye.

As it is explained in chapter-3, the lifetime stages between 673 and 1123 K are solely due to precipitation. The variation in total surface area between precipitates and matrix will be responsible for the changes in trapping rate of positrons and hence, the observed changes in lifetime. Above 673 K, the nucleation of precipitates takes place. They grow as a function of both time and temperature. Since the treatment time is fixed for 1 h, they grow at faster rate at higher temperatures. Consequently, the surface area of precipitates increases along with the volume fraction of precipitates. This precipitation process increases the positron trapping at open volume defects across the precipitate-matrix interfaces. Hence, the increase in lifetime between 673 and 873 K corresponds to increase in number density and size of precipitates. However, during coarsening process, i.e., above 873 K, the number density and volume fraction decrease as the solubility of alloying elements increases at higher temperatures. As a result, there is a significant decrease in relative surface area of precipitates during coarsening [17]. Consequently, the fraction of positrons trapped at interfaces increases during the growth and decreases during the coarsening. Microstructure of the steel, as observed using FESEM, corresponding to these stages is shown in Figure-4.3 and Figure-4.4. As-normalized (Figure-4.3(a)) and 673 K tempered (Figure-4.3(b)) samples show similar microstructure indicating the decrease in lifetime in first stage is not responsible for lath boundaries and grain boundaries. The nucleation of precipitates, their growth and coarsening can be found from the microstructures shown in Figure-4.4(a,b,c) respectively. Low magnification micrographs for corresponding tempering temperatures are shown in Figure-4.5 for overview of precipitation stages.

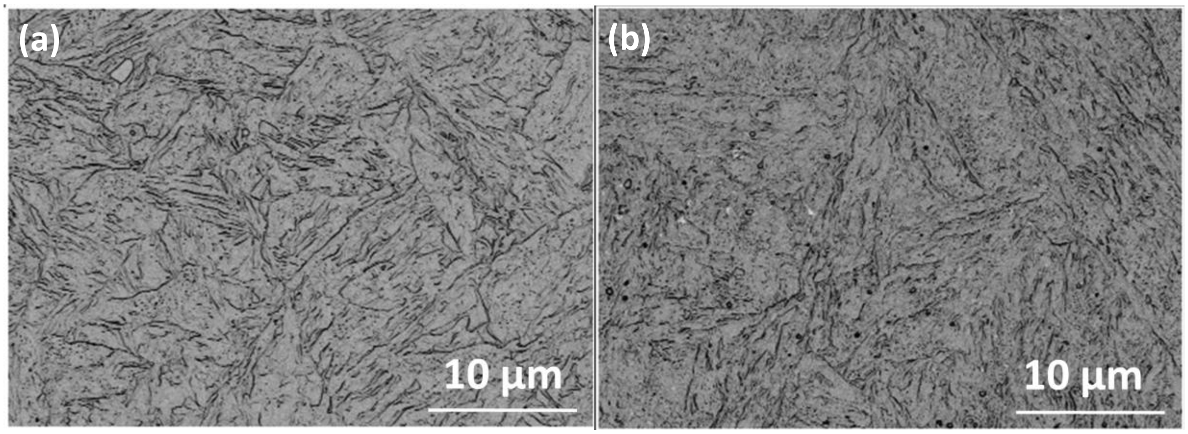

Figure-4.3: FESEM micrographs of modified 9Cr-1Mo steel in (a) as-normalized and (b) subsequently tempered at 673 K temperatures. Image colours inverted to increase the visibility of grain boundaries.

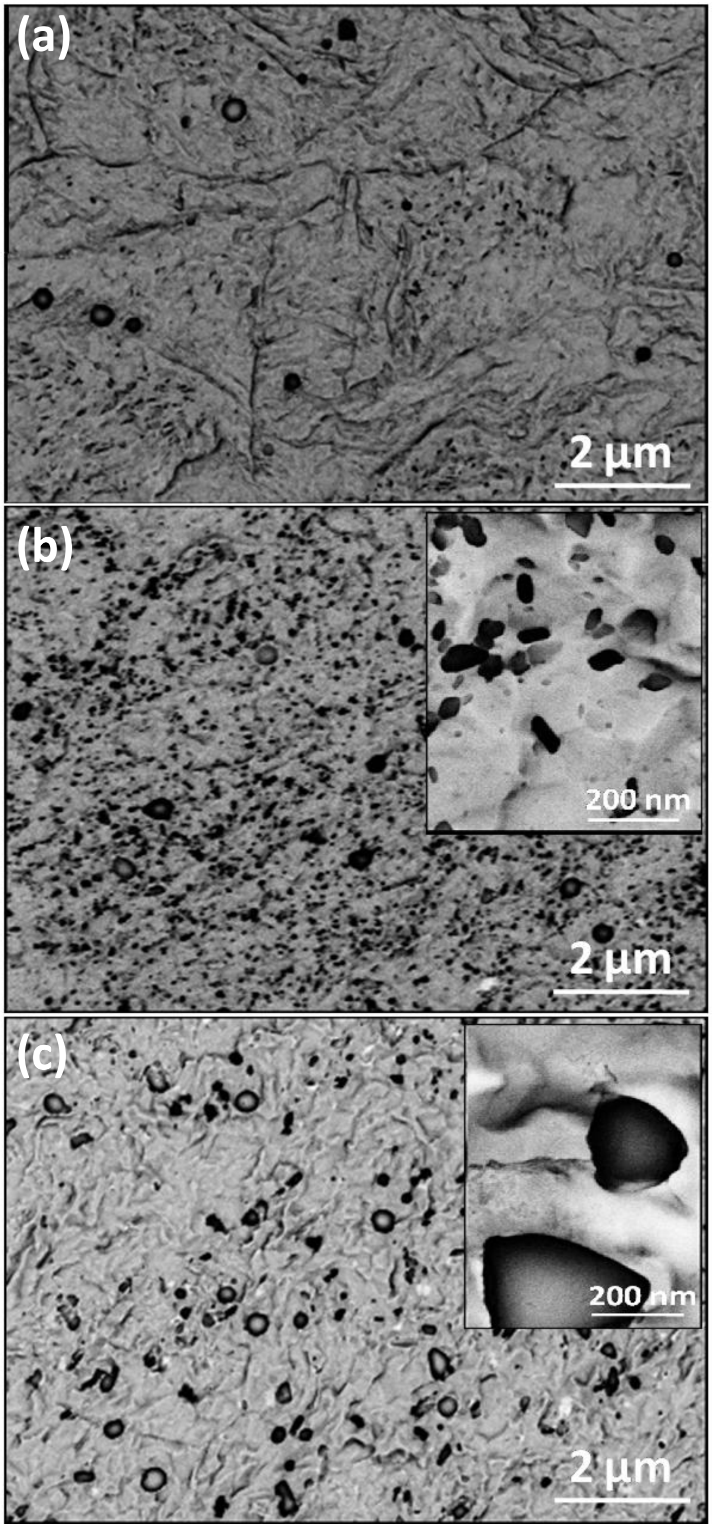

Figure-4.4: FESEM micrographs of samples tempered at (a) 773 K, (b) 873 K and (c) 1073 K indicating nucleation, growth and coarsening respectively. Image colours inverted to increase the visibility of precipitates.

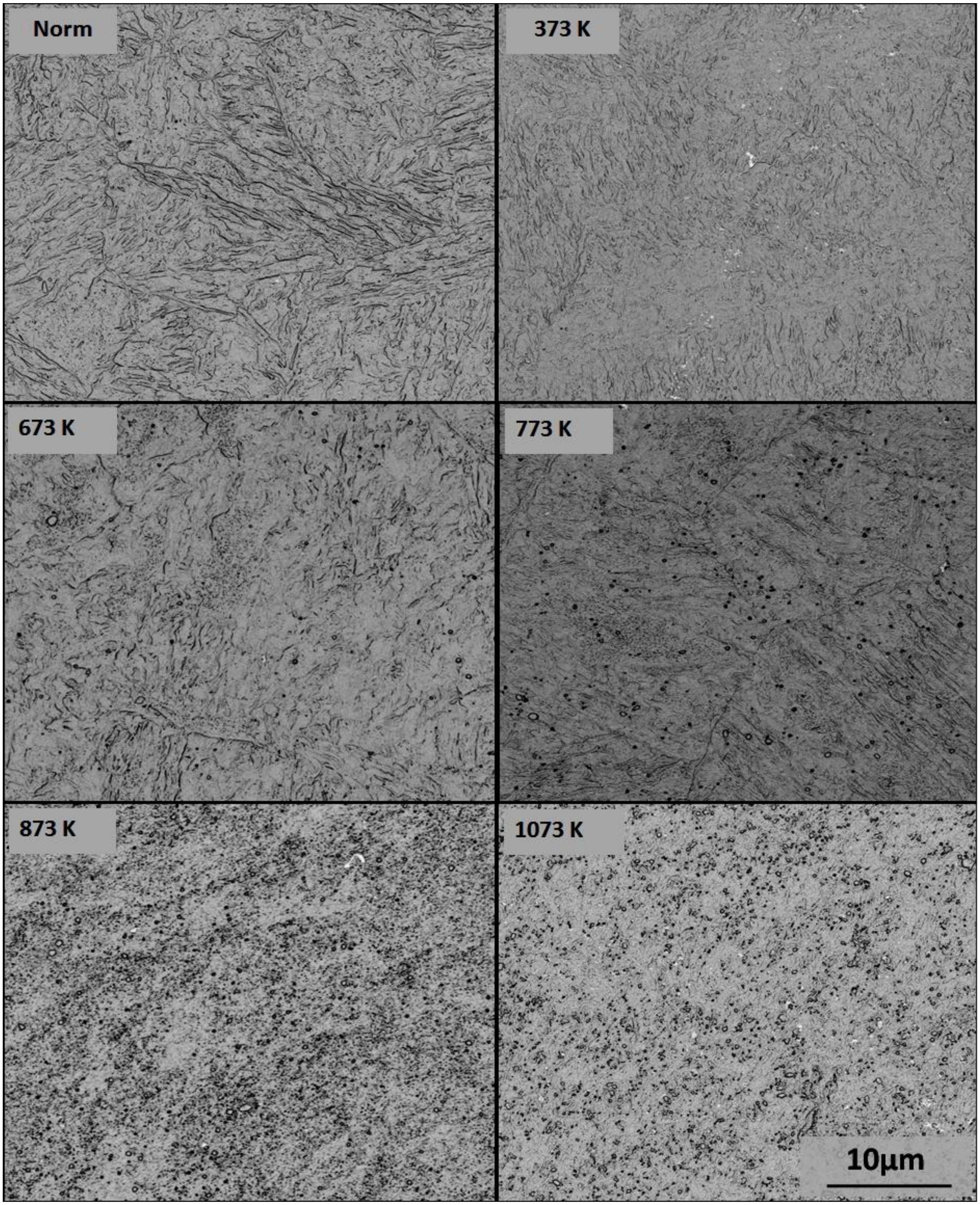

Figure-4.5: Low magnification FESEM micrographs of samples in as-normalized and subsequently tempered at 373 K, 673 K, 773 K, 873 K and 1023 K.

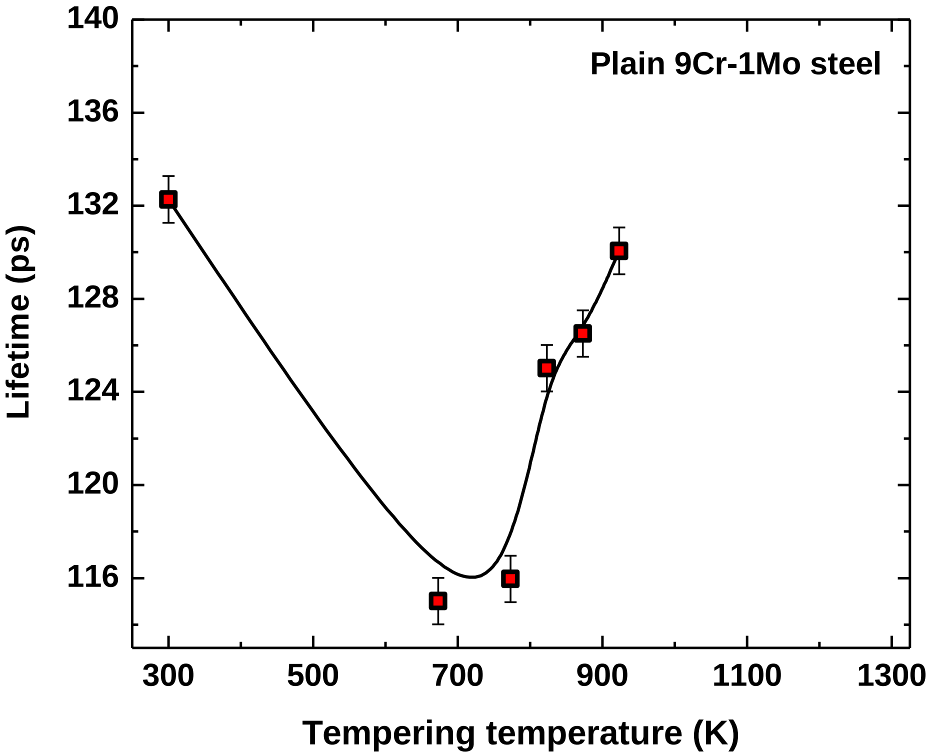

Figure-4.6: Positron lifetime, as a function of tempering temperature, in plain 9Cr-1Mo steel sample. The line through the data points is a guide to the eye. The variation in lifetime is similar to the variation lifetime in modified 9Cr-1Mo steel indicating $M_{23}C_6$ *are the dominating precipitates responsible for the increase in lifetime in both the cases.*

To identify the role of NbC and VC precipitates apart from $M_{23}C_6$ on positron lifetime, lifetime measurements were also carried on plane 9Cr-1Mo steel samples. Figure-4.6 shows the corresponding results. The results are similar to those of modified 9Cr-1Mo steel. This indicates the contribution to higher lifetime from NbC and VC is not significant due to the presence of $M_{23}C_6$ precipitates. It was also known that the concentration of $M_{23}C_6$ precipitates is an order larger than MC precipitates in both 9Cr-1Mo and 9Cr-2W steels [18]. Hence, the major contribution to higher lifetime could arise only from $M_{23}C_6$ precipitate interfaces. This study clarifies that the considerations of major contribution from vanadium carbide precipitates is not correct [19].

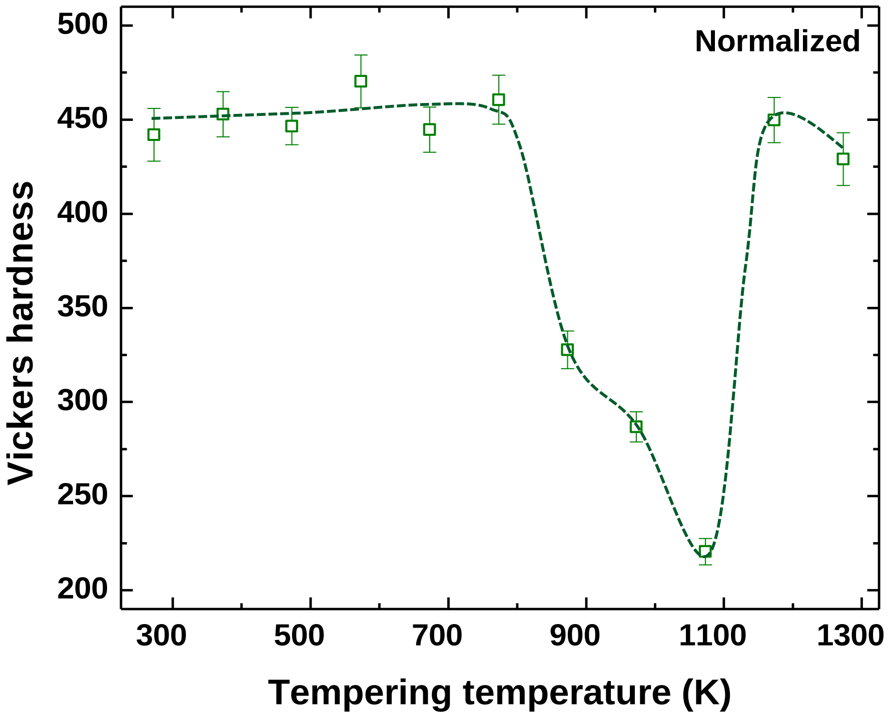

Figure-4.7: Vickers hardness as a function of tempering temperature in normalized modified 9Cr-1Mo steel sample. Recovery of lath structure resulted in decrease of hardness between 773 K and 1073 K. Precipitation hardening contribution is not explicitly seen in the hardness changes.

The corresponding variation in hardness as a function of tempering temperature is shown in Figure-4.7. Hardness is almost constant until 773 K indicating the martensitic phase is stable and it is consistent with earlier study that there is hardly any change in hardness till 823 K [20]. Then hardness decreases until 1073 K. The variation in hardness above 873 K was reported earlier [13] and our results are consistent with those. Because the martensite to ferrite conversion and precipitation are simultaneous, we could not see explicitly the precipitation stages in hardness results during 673-1073 K. The increase in hardness beyond 1073 K indicates the formation of martensite as the treatment temperature is above lower critical temperature.

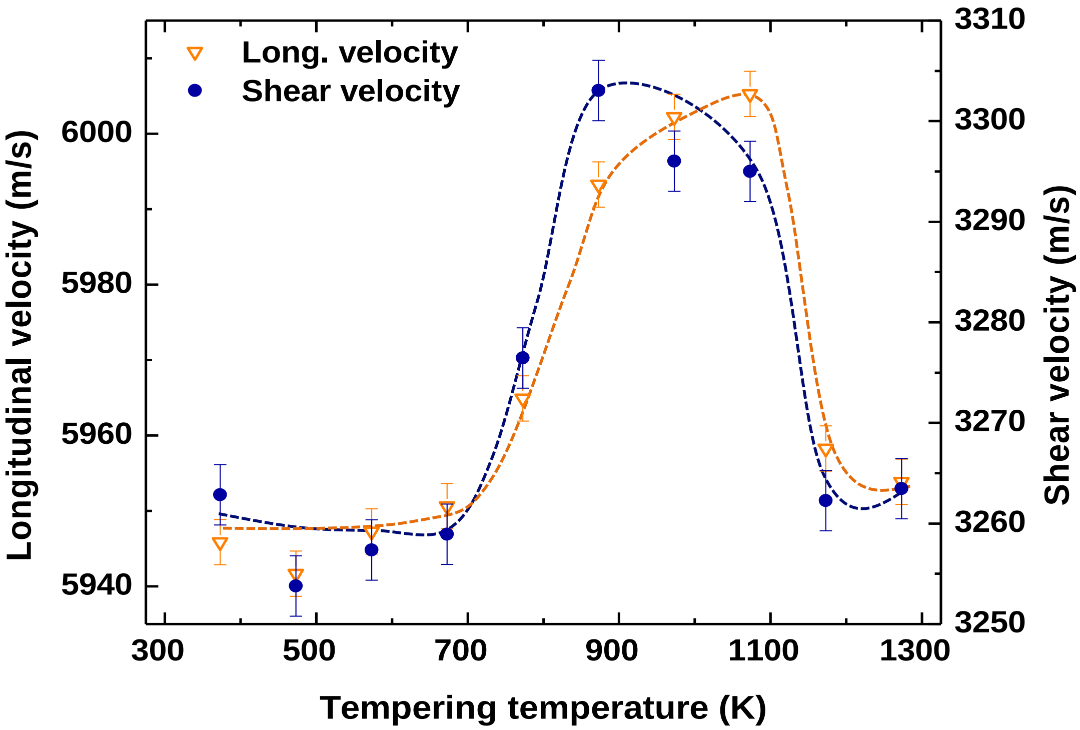

Figure-4.8: Ultrasonic longitudinal and shear velocities as a function of tempering temperature in normalized modified 9Cr-1Mo steel sample.

Figure-4.8 shows ultrasonic velocity (longitudinal and shear) variation as a function of tempering temperature. They remain constant until 673 K, increases up to 1073 K and steep reduction beyond 1073 K. These distinct changes are similar to those seen in hardness. It may be pointed out that ultrasonic velocities are sensitive to changes above 673 K while, hardness measurements are sensitive to changes only above 773 K. It was reported that in ferritic steels, the effect of dislocations on strengthening is generally smaller compared to the effect of grain size and shape [20]. Since the lath structure retains its shape and size upto 773 K, decrease in hardness was not expected to be pronounced until the treatment temperature is above 773 K. Even if there is any small decrease in hardness due to decrease in dislocation density, precipitation hardening due to nucleation of precipitates could compensate. Hence, we did not see any change in hardness below 773 K. However, the nucleation of precipitates causes changes in elastic moduli of the matrix as the alloying elements, especially carbon, composition starts changing. Hence, the ultrasonic velocity shows sensitivity from 673 K onwards to precipitation.

Unlike ultrasonic velocity and hardness variations, positron lifetime variation (Figure-4.2), brought out clearly distinct stages of microstructural changes corresponding to as-quenched defects annealing, growth of precipitates and their coarsening.

Even though positron lifetime results could bring more information regarding microstructural changes as shown in Figure-4.2, it is rather difficult to ascribe an unique microstructure to a specific lifetime i.e. lifetime alone is incapable to identify the microstructure of a sample with unknown treatment history. There could be as many as four different microstructural stages for a given lifetime, as evident from Figure-4.2 (a horizontal line intersects at four points for a fixed lifetime). Similarly, ultrasonic velocity or/and hardness alone could not distinguish microstructures independently. But, a combination of ultrasonic velocity and/or hardness along with positron lifetime could distinguish different microstructures, as no set of three parameters (positron lifetime, hardness and ultrasonic velocity) will be identical over all the temperatures.

Figure-4.9 shows the correlation between positron lifetime, ultrasonic velocity and Vickers hardness as a three-dimensional plot. The distribution can be mainly classified into two regions accordingly whether the structure is martensite or tempered martensite. As can be seen, the martensite has low ultrasonic velocity, large hardness values and within this microstructure, lifetime exhibited a variation over 132 ps to 116 ps corresponding to existence and annealing of point defects and dislocations. On the other hand, for the precipitation stage it is found that ultrasonic velocity is high, hardness exhibits a reducing trend and the lifetime exhibits 132 ps to 120 ps. Also, the point at 773 K showed its tendency towards precipitation region indicating the nucleation of precipitation. The distribution of points corresponding to different microstructures suggests that combination of ultrasonic velocity and hardness with complementary positron lifetime will enable more pointed identification of the microstructure. Considering the fact that ultrasonic velocity and positron lifetime are non-destructive techniques and use of these in conjunction with hardness will be useful methodology for application to various practical alloys.

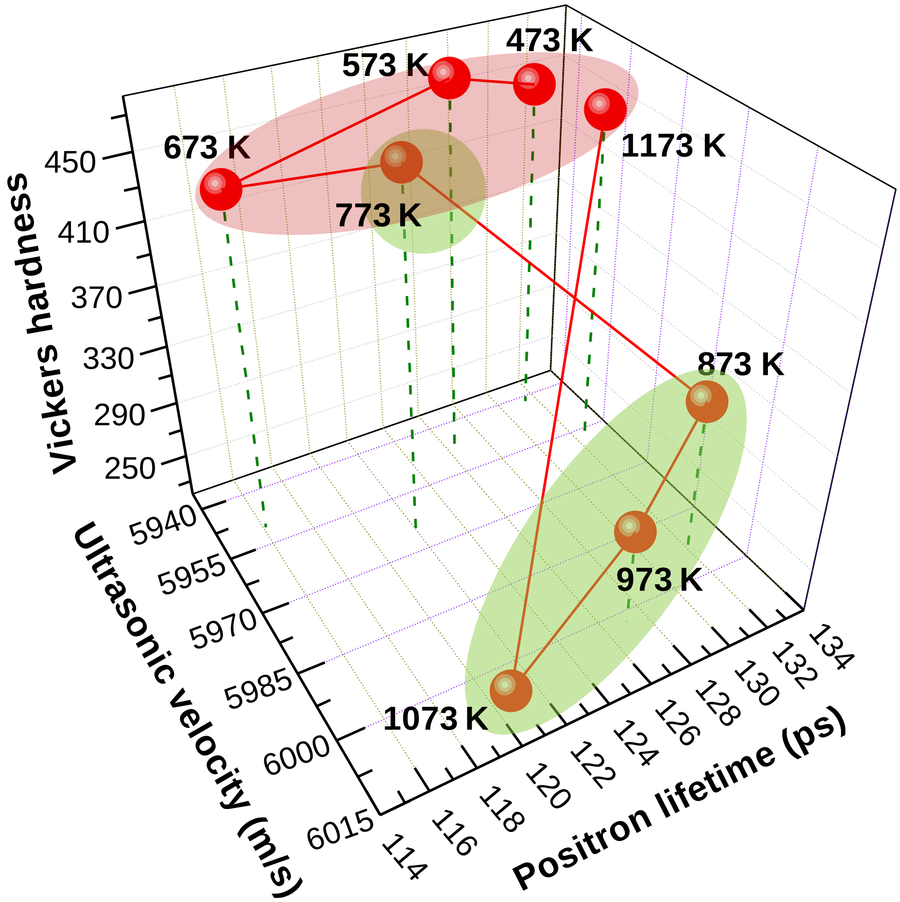

Figure-4.9: Correlation plot of observed positron lifetime, ultrasonic velocity and hardness for normalized steel sample at representative temperatures. The red region represents martensitic phase and the green region represents where precipitation was seen. The green region at temperature 773 K also shows its tendency towards precipitation. It should be noted that nucleation of precipitates is observed in SEM micrographs of 773 K tempered sample.

To bring out the selective nature of positrons to open volume defects associated with microstructural changes, X-ray diffraction studies were also carried out for comparison. XRD spectra of modified 9Cr-1Mo steel in as-normalized condition and subsequently tempered at 773 K, 873 K and 1073 K are shown in Figure-4.10. There are shifts in peak positions and decrease in peak broadening between martensite lath and ferrite recovery. Other than the shift, there are absolutely no indications with regard to precipitation. The diffraction peak corresponding to the major precipitate $M_{23}C_6$, in terms of volume fraction, was also not seen. It is known that at any stage, the total precipitates together will not be greater than 2-3 % in volume fraction [21]. Hence, the possibility of finding the corresponding peaks will be difficult through XRD. This study shows that XRD is not a suitable technique to study the precipitates in 9Cr ferritic/martensitic steels.

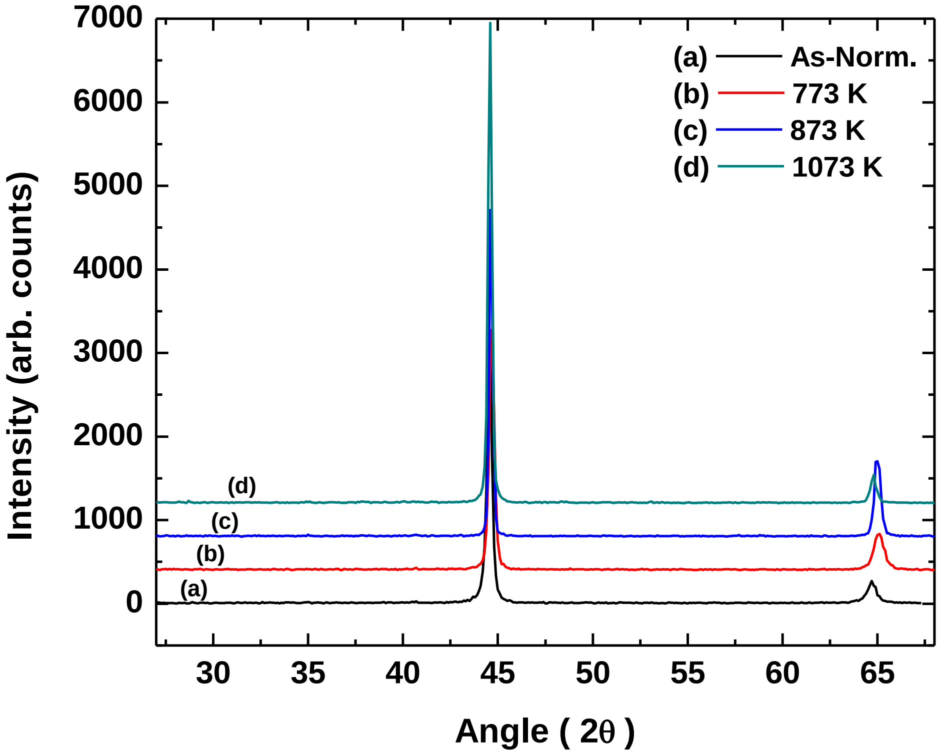

Figure-4.10: X-ray diffraction spectrum of normalized steel in (a) as-prepared and subsequently aged at (b) 773 K (c) 873 K and (d) 1073 K.

A comparison is now presented between the observed stages of microstructural changes of modified 9Cr-1Mo with that of EUROFER97. In the case of modified 9Cr-1Mo steel, lifetime is found to increase beyond 673 K while, in the case of EUROFER97 lifetime started increasing only beyond 773 K. Hence, precipitation in modified 9Cr-1Mo steel is at relatively lower temperature than EUROFER97 steel (Figure-3.1). The diffusivities of alloying elements in EUROFER97 could be lower than modified 9Cr-1Mo steels. Tungsten (W) only being the major difference in both the steels, the diffusivities of alloying elements are believed to be reduced by W alloying. The peak lifetime at which the growth dominated process and coarsening dominated precipitation transit is also off shifted as compared to EUROFER97 sample. In the case modified 9Cr-1Mo steel it is found at 873 K while, in EUROFER97 steel the peak lifetime is observed at 973 K. There is no noticeable change in lower critical temperature i.e., around 1123 K between modified 9Cr-1Mo and EUROFER97 steel, as seen by PAS within the measurement interval of 50 K.

4.4.2 Normalized and tempered steel

The as-prepared normalized and tempered sample consists of tempered martensite with precipitates decorating lath boundaries and grain boundaries. The majority of these precipitates will be $M_{23}C_6$. There exist also MX type precipitates both at lath boundaries and inside lath. A scanning electron microscopy micrograph of normalized and tempered structure is shown in Figure-4.11. Lath structure can be observed with precipitates decorating along the boundaries. Prior-austenite grain size will be in the order of 20 µm and hence is not seen in the micrograph. The lifetime in normalized and tempered steel is 123 ps, which matches well with 1023 K tempered sample in the previous section (Figure-4.2).

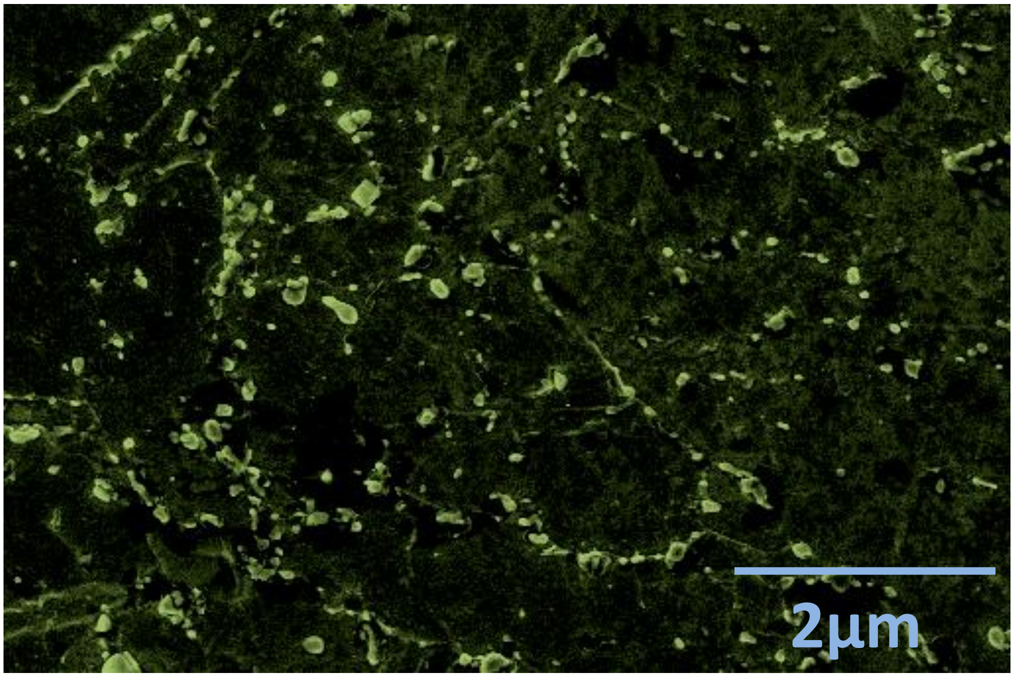

Figure-4.11: FE SEM micrograph of as-prepared normalized and tempered modified 9Cr-1Mo steel.

Figure-4.12(a, b and c) shows the Vickers hardness, ultrasonic velocity and positron lifetime in normalized and tempered sample as a function of aging temperature. The hardness of normalized and tempered steel is 245 VHN and it is almost constant till the aging temperature crosses the tempering temperature. At 1073 K a marginal decrease in hardness is observed. This softening could be due to coarsening of laths and precipitates resulting in the conversion of tempered martensite towards ferrite. For temperatures beyond lower critical temperature i.e. 1083 K, hardness increases as the resultant structure is martensitic. Similarly, ultrasonic velocities are constant till 1073 K and the velocities decreased above lower critical temperature. Martensitic structure, having relatively lower elastic moduli as compared to tempered martensitic structure, results in decrease of ultrasonic velocities. Ultrasonic velocities did not show sensitivity to softening observed in hardness at 1073 K.

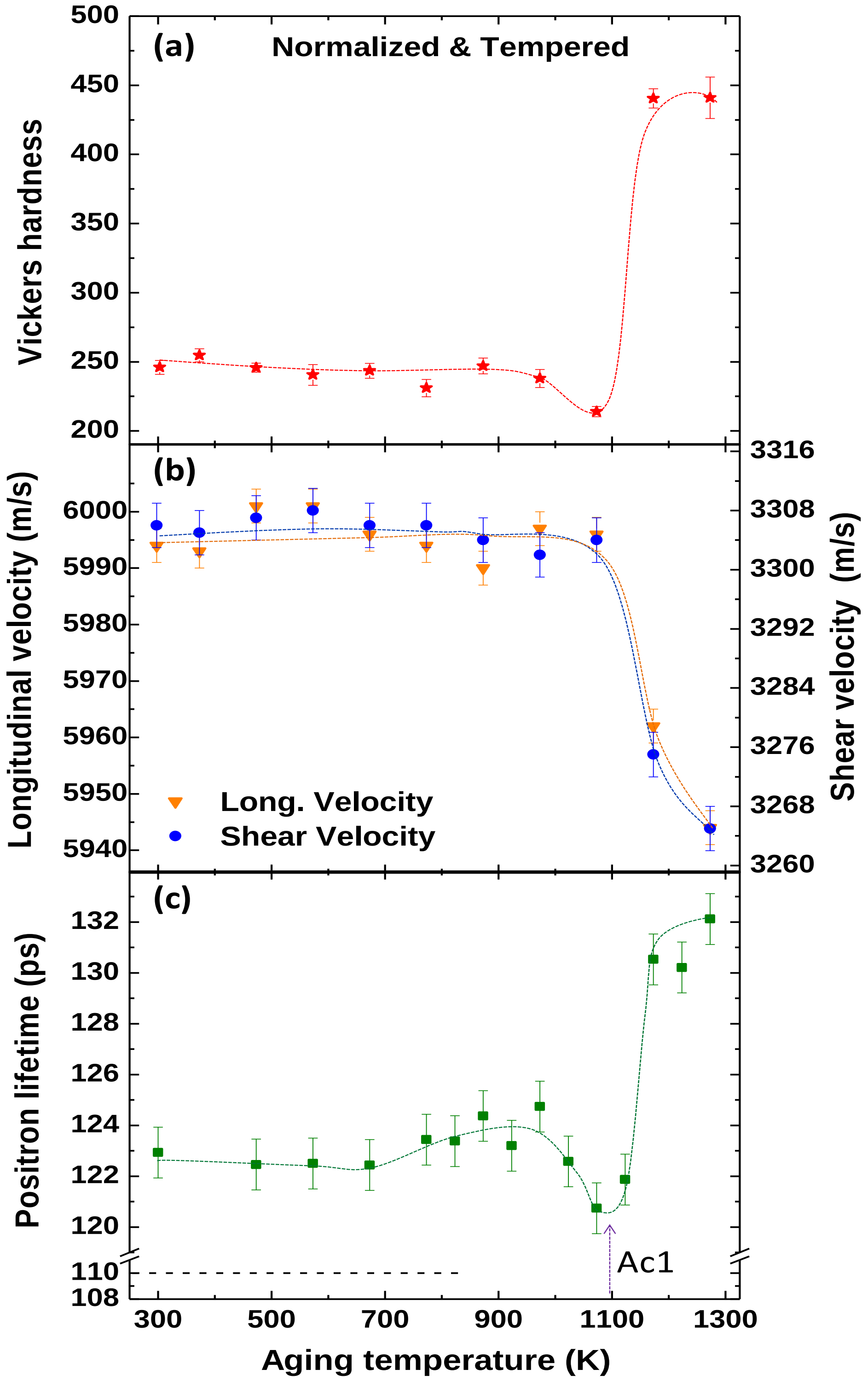

Figure-4.12: (a) Vickers hardness, (b) ultrasonic velocities and (c) positron lifetime as a function of aging temperature in normalized and tempered modified 9Cr-1Mo steel sample. Finer changes corresponding to secondary precipitation and coarsening seen in positron lifetime values between 673 K-1123 K.

In the case of positron lifetime also, the lifetime stays constant till 673 K (Figure-4.12 (c)) indicating no changes in microstructure occurred. However, as it can be noticed, between 673 and 873 K a marginal increase in lifetime is observed. This temperature range corresponds to diffusion of alloying elements that leads to precipitation of secondary precipitates.

This secondary precipitation can be understood by considering the solubility limits of carbon. The solubility of carbon is less at 873 K than at 1033 K (tempering temperature) in Fe. Hence, the volume fraction of precipitates will be higher at 873 K as compared to that of 1033 K. When the normalized and tempered steel is treated at 873 K, the carbon further precipitates as carbides to maintain the solubility limits. This range of temperature corresponding to increase in lifetime matches exactly with precipitation observed in normalized sample (Figure-4.2). New fine precipitation along with already existing primary precipitates causes an increase in the fraction of positrons trapping at precipitate-matrix interfaces and consequently the increase in lifetime. At temperature beyond 873 K these fine precipitates, being unstable, dissolve due to increase in solubility of the alloying elements. The resultant effect decreases the total surface area between precipitates and matrix which is proportional to fraction of positrons trapping at interfaces. Hence, the observed decrease in lifetime from 873 K to 1073 K corresponds to dissolution of secondary precipitates and coarsening of primary precipitates. Above lower critical temperature i.e. 1083 K, the increase in positron lifetime is in good agreement with increase in hardness and decrease in ultrasonic velocities corresponding to formation of martensite structure. Existence of dislocations, associated vacancies and vacancy-carbon complexes in martensite structure are responsible for the higher lifetime in this temperature range.

The scanning electron microscopy images for samples subsequently aged at 923 K, 1023 K and 1273 K are shown in Figure-4.13(a-c). As seen the microstructure is found to be stable up to 1023 K, as compared to as-prepared sample (Figure-4.11), and only beyond that noticeable changes in microstructure are observed due to martensite formation in 1273 K heat treated sample.

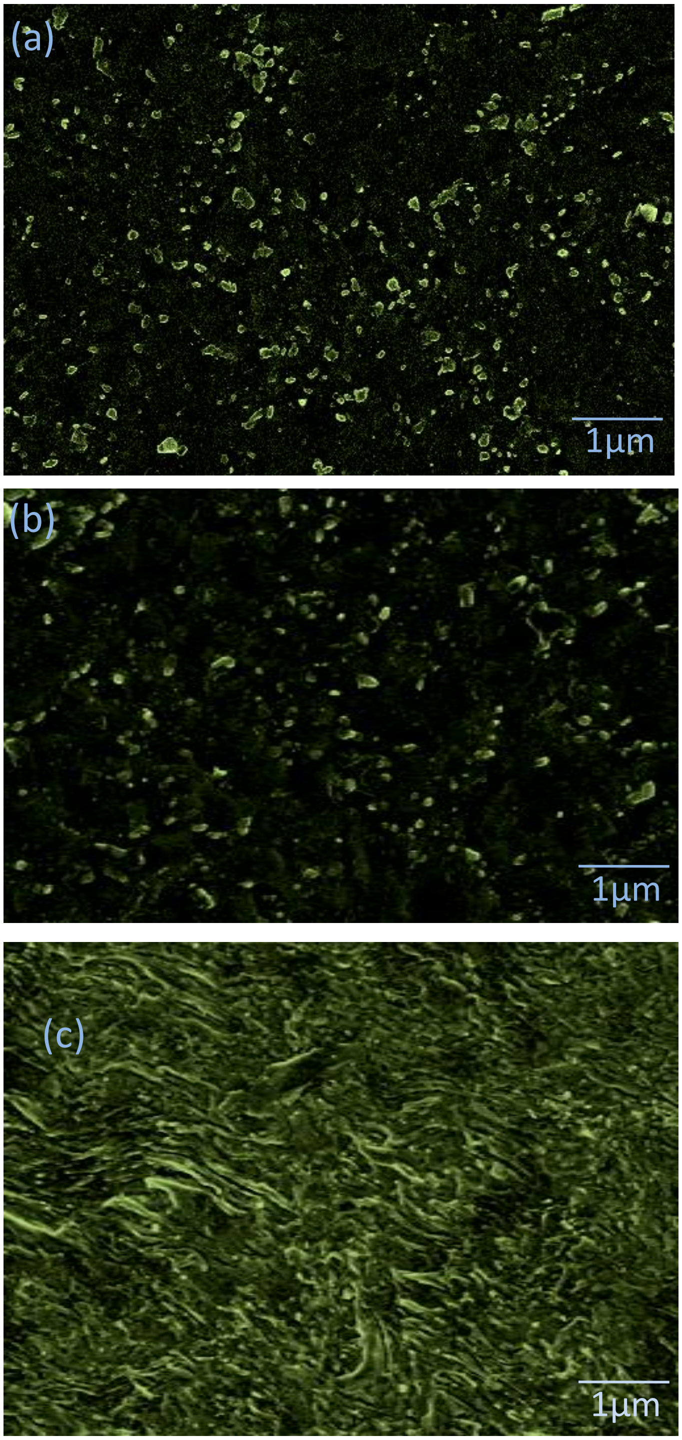

Figure-4.13: SEM images of normalized and tempered steel subsequently aged at (a) 923 K (b) 1023 K and (c) 1273 K.

While this secondary precipitation process, during 673-1073 K, could be seen in positron measurements, it is not seen clearly in ultrasonic velocities and hardness measurements. The reason for high sensitivity of positron measurements will be illustrated in terms of variation in positron traps at precipitate-matrix interfaces and variation in volume fraction of precipitates that cause change in precipitate hardening and elastic moduli which are responsible for the changes in hardness and ultrasonic velocities, respectively. A schematic diagram of normalized and tempered microstructure with precipitates along grain/lath boundaries and intra lath precipitates is shown in Figure-4.14. The precipitates along the grain boundaries are mostly $M_{23}C_6$, the intra lath precipitates are mostly MX in nature [9, 14].

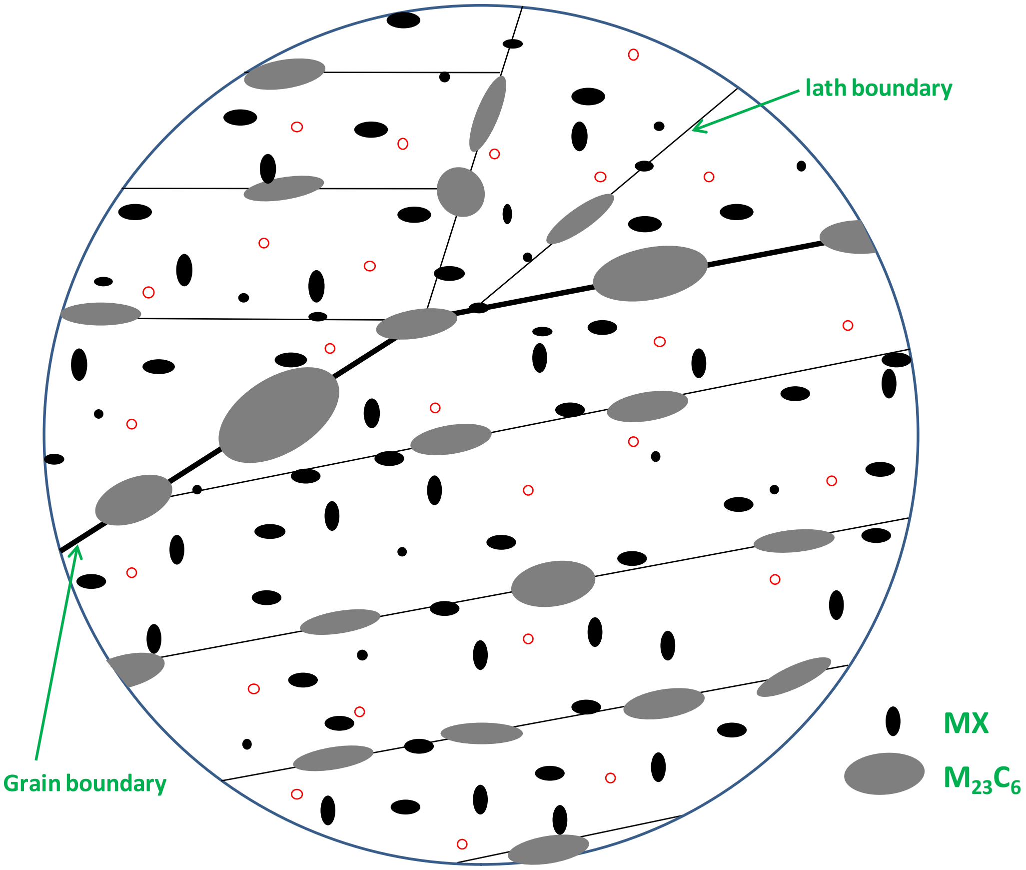

Figure-4.14: Schematic representation of microstructure of normalized and tempered steel aged between 723-1073 K. Open circles represent the formation of secondary precipitates during aging, which are probed by positrons during 723-1073 K.

Let the open circles in figure-4.14 be secondary precipitates formed during heat treatment between 673 and 1073 K. Positron diffusion length in metals and alloys is typically around 100 nm. A fraction of positrons gets trapped at precipitate-matrix interfaces and the rest annihilate in the matrix. Lifetime of positrons annihilating in open volumes at interfaces is higher than the lifetime in the matrix. In the present case, secondary precipitate formation will increase the fraction of positrons annihilating at interface open volumes. The relative change in surface area of precipitates with and without secondary precipitates is significant enough to trap extra fraction of positrons. Consequently, the increase in lifetime is observed during 673-1073 K. The volume changes in total precipitation are significantly small to bring any change in elastic moduli. Hence, no changes are seen in ultrasonic velocities. As the precipitates will be finer in size, they cannot hinder the dislocation motions significantly. Consequently, the changes are not seen in hardness measurements.

The sensitivity of PAS, along with ultrasonic velocity and hardness, can be utilized in identifying the microstructural changes rather uniquely in prolonged aging conditions. The correlation plot between the parameters in normalized and tempered sample results is shown in Figure-4.15. The aging treatment for 1 h did not bring any significant changes during 300 – 973 K. However, the expected softening around 1073 K resulted in variation in parameters, which can be distinctly seen in the correlation plot. The similar changes observed at 1073 K might be seen at lower temperature when the sample is aged at tensile stress, due to accelerated change in microstructure under stress. This demonstrates a methodology to identify microstructural changes during aging. This plot can be compared with that of normalized sample (Figure-4.9) at 1173 K for consistency in identifying martensitic phase identification.

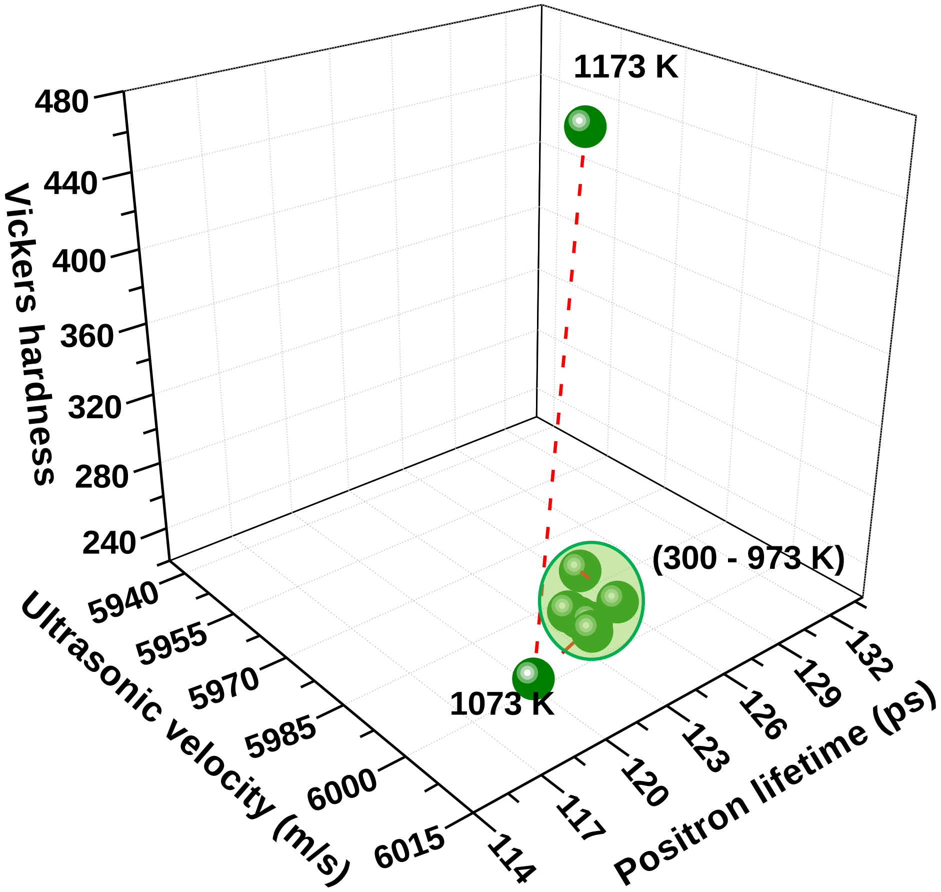

Figure-4.15: Correlation plot of observed positron lifetime, ultrasonic velocity and hardness for normalized and tempered steel sample at representative temperatures. The circled region represents the state of the sample during 300 - 973 K aging indicating minor changes in measured parameters. Significant microstructural changes can be seen only at 1073 K treatment.

4.5 SUMMARY

From the current study of PAS and other complementary techniques on modified 9Cr-1Mo steel the following observations are summarized.

- PAS is found to be unique in identifying annealing of quenched-in defects in normalized steel below 673 K, during which ultrasonic velocity and hardness stay constant.

- In normalized steel, as a function of tempering temperature (between 673 K – 1073 K) the growth dominated and the coarsening dominated stages of precipitation are distinguished using PAS and the results are substantiated with SEM studies. Ultrasonic velocity and hardness showed changes only due to changes in moduli and martensitic lath structure, respectively. Hence, the complementary nature of PAS in distinguishing precipitation is brought out.
- Comparison of the positron lifetime variation as a function of tempering temperature between the plain 9Cr-1Mo steel and the modified 9Cr-1Mo steel found that the $M_{23}C_6$ precipitates are predominantly responsible for the increase in lifetime above 673 K.
- PAS showed the signatures of fine secondary precipitation during aging of the normalized and tempered steel between 673 K–1073 K. Ultrasonic velocity, hardness and scanning electron microscopy are found to be ineffective for identifying these finer changes.
- Correlation between PAS, ultrasonic velocity and hardness showed that the set of three parameters is an unique combination for distinguishing distinct microstructure. Hence, it is found that the usage of PAS in conjunction with the ultrasonic velocity or/and the hardness can identify the microstructure of ferritic steels better.

4.6 REFERENCES

---

[1] C. F. Coleman, NDT Int. **10**, 235 (1977).

[2] R Ferragut, A Somoza, A Dupasquier, J. Phys.: Condens. Matter. **8**, 8945 (1996).

[3] A. Dupasquier, R. Ferragut, M. M. Iglesias, M. Massazza, G. Riontino, P. Mengucci, G. Barucca, C. E. Macchi, A. Somoza, Phil. Mag. A **87**, 3297 (2007).

[4] R. Rajaraman, Padma Gopalan, B. Viswanathan, S.Venkadesan, J. Nucl. Mater. **217**, 325 (1994).

---

[5] P. Gopalan, R. Rajaraman, G. Amarendra, C. S. Sundar, B. Viswanathan, T. Jayakumar, Palanichamy, B. Raj. J. Nucl. Mater. **345**, 162 (2005).

[6] K. V. Rajkumar, R. Rajaraman, Anish Kumar, G. Amarendra, T. Jayakumar, Philos. Mag. **89**, 1597 (2009).

[7] M.K. Booker, V. K. Sikka, B. L. P. Booker, Proc. of ASM International conference on ferritic steels for High Temperature Applications, Warrendale. PA. Ashok K. Khare (Eds.). ASM, Metals Park, OH , 257 (1981).

[8] R. L. Klueh, J. M. Vitek, J. Nucl. Mater. **132**, 27 (1985).

[9] Wendell B. Jones, C. R. Hills, D. H. Polonis, Metall. Trans. A **22A**, 1049 (1991).

[10] V. Thomas Paul, S. Saroja, M. Vijayalakshmi, J. Nucl. Mater. **378**, 273 (2008).

[11] Anish Kumar, K. Laha, T. Jayakumar, K. Bhanu Sankara Rao, Baldev Raj, Metall. Mater. Trans. A **33**, 1617 (2002).

[12] Baldev Raj, D. K. Bhattacharya, T. Jayakumar, Met. Mater. Process. **7**, 19 (1995).

[13] Harendra Kumar, J. N. Mohapatra, Rajat Kumar Roy, R. Justin Joseyphus, Amitava Mitra, J. Mater. Process. Tech. **210**, 669 (2010).

[14] Fujio Abe, Sci. Technol. Adv. Mater. **9**, 013002 (2008).

[15] M. Rieth, M. Schirra, A. Falkenstein, P. Graf, S. Heger,. H. Kempe, R. Lindau, H. Zimmermann, EUROFER97, Tensile, charpy, creep and structural test, FZKA 6911.

[16] J. Kansy, Nucl. Instrum. Meth A **374**, 235 (1996).

[17] S. Hari Babu, K. V. Rajkumar, S. Hussain, G. Amarendra, C. S. Sundar, T. Jayakumar, J. Nucl. Mater. **432**, 266 (2012).

[18] J. J. Kai, R. L. Klueh, J. Nucl. Mater. **230**, 116 (1996).

[19] V. Ragunanthan, S. Hari Babu, Varghese Anto Chirayath, R. Rajaraman, G. Amarendra, S. Saroja, C.S. Sundar, Ana Alamo, Baldev Raj, Phys. Status Solidi C **6**, 2307 (2009).

[20] B. Mintz, E. M. Maina, W. B. Morrison, Mater. Sci. Technol. **24**, 177 (2008).

[21] P. Fernandez, M. Garcia-Mazario, A. M. Lancha, J. Lapena, J. Nucl. Mater. **329-333**, 273 (2004).

Chapter - 5

Cr Segregation in Fe-Cr Alloys

5.0 PREAMBLE

This chapter aims at bringing out the influence of initial non-equilibrium conditions on the formation of Cr precipitates in Fe-9Cr alloys, investigated using positron lifetime measurements along with complementary studies. Effect of dislocations and grain boundaries on segregation of Cr will be discussed. Results of detailed isothermal studies will be presented to indicate the range of temperature where the Cr precipitates are stable. Further, results on Fe-Cr alloys with concentration ranging from 2 - 20 wt% will be presented to discuss and debate regarding the nature of precipitates.

5.1 INTRODUCTION

Due to irradiation, the increase in hardness and hence, embrittlement of Fe-Cr alloys with Cr concentration higher than 9% is known. It is qualitatively understood that the hardening is due to Cr segregation and it is found to be in the form of coherent, Cr rich α' phase, as described in review of Malerba et. al. [1]. The Cr rich α' phase formation is known for hardening of steels with Cr concentration greater than 12% [2]. However, it is not still clear about the exact mechanism of increase in hardness in Fe-Cr alloys [1]. Also, there are no studies carried out on Fe-Cr alloys to rationalize the effects of dislocations on Cr segregation during pure thermal ageing. This chapter aims at studying the effect of dislocations and the nature of Cr precipitates formed during ageing.

5.2 EXPERIMENTAL PROCEDURE

5.2.1 Sample preparation and chemical characterization

Fe-Cr binary alloys are prepared as two batches, using arc furnace. In first batch, Fe-9Cr, Fe-12Cr were prepared from 99.99 purity Fe and Cr metals. The chemical composition of as prepared alloys, analysed using Electron Probe Micro-Analyzer (EPMA), is shown in Table-5.1. No other impurities were observed within the detectable limit (0.01 at%). Owing to the importance of carbon content on the formation of vacancy-carbon complexes [3] and carbides [4], carbon content was further measured using combustion method. The average carbon content measured over three iterations was found to be 65 ± 10, 78 ± 10 and 79 ± 10 ppm in Fe-9Cr, Fe-12Cr and pure Fe samples, respectively. It is to be noted that the solubility of carbon in pure Fe at room temperature is about 450 ppm (0.008 wt%). Carbon content was also measured from a sample after a set of isochronal heat treatment experiments so as to find out any carbon addition during heat treatments. It was found that the carbon concentration remains same. The arc melted samples were homogenized at 1090 K for 144 h in vacuum sealed quartz tubes. The samples were cold rolled so as to make sheets.

Second batch of samples, Fe-(2, 5, 9, 15, 20 wt%) Cr were also prepared and homogenized in similar way. Post-preparation chemical characterization using Auger electron spectroscopy (AES) is shown in Table-5.2. No other impurity elements found within the detectable limits of the technique i.e., 0.5 at%.

Table-5.1: Chemical composition of Fe-9Cr, Fe-12Cr alloys as measured by EPMA.

Alloy	Fe-9Cr	Fe-12 Cr
Element	**Composition (wt %)**	
C	< 0.01	< 0.01
Cr	9.50 ± 0.23	11.66 ± 0.24
Fe	Bal.	Bal.

Table-5.2: Chemical composition of Fe-(2-20)Cr alloys as measured by AES.

Alloy	Fe-2Cr	Fe-5 Cr	Fe-9Cr	Fe-15Cr	Fe-20Cr
Element	**Composition (wt %)**				
Cr	3.3 ± 0.5	5.4 ± 0.5	7.3 ± 0.5	15.3 ± 0.5	16.7 ± 0.5
Fe	96.7 ± 0.5	94.6 ± 0.5	92.7 ± 0.5	84.7 ± 0.5	83.3 ± 0.5

5.2.2 Heat treatments

Isochronal and isothermal studies of Fe-Cr alloys were carried out mainly with four different initial conditions. The four initial conditions and the criteria are as follows.

(a) *Deformed condition*: Heat treated at 1313 K (inside γ–loop) for 1 h and air-cooled followed by heat treatment at 923 K for 3 h. Finally the samples were deformed by cold rolling to 20 % thickness reduction in steps. Isochronal studies with this initial condition were aimed at studying the differences in the recovery stages of deformation induced defects which will be compared with deformed pure Fe.

(b) *Quenched condition*: Heat treated at 1423 K (inside γ–loop) for 1 h and then quenched to room temperature by air cooling. The phase transition from FCC to BCC, during quenching, results in the formation of martensitic structure [5]. The treatment and the resultant morphology being similar to practical ferritic steels, the recovery of lath structure and the effect of dislocations during recovery are important for understanding Cr segregation. Henceforth, if mentioned ‘quenched’ it is under this condition.

(c) *Homogenized condition*: The alloys were homogenized at 1073 K, just below γ–α phase boundary, for 2 h. This treatment results in the formation of dislocation-free coarse grained BCC structure (α-phase). Studies with this condition, having no dislocations and lath boundaries, will rationalize the effect of dislocations in quenched condition.

(d) *Deformation from defect-free condition:* The homogenized alloys in the defect-free condition, mentioned above, were deformed by 20% cold-working. This deformation is different from first condition with respect to its condition prior to deformation.

With the initial conditions mentioned above, alloys were heat treated isochronally and isothermally for various experimental studies. Otherwise mentioned, the holding time in isochronal treatment is 1 h in all the cases.

5.2.3 Experimental details

Positron lifetime measurements were carried out at room temperature with a fast-fast coincidence lifetime spectrometer having a time resolution of 260 ps (FWHM). Generally, for each lifetime measurement > 2 x 10^6 counts were accumulated. However, isothermal studies were carried with counts > 0.3 x 10^6, after cross checking the accuracy of lifetime as compared to spectrum with large counts. The acquired lifetime spectra were analyzed using LT program [6]. Positron Doppler broadening Measurements, Vickers microhardness measurements are carried out at room temperatures, in the same procedure explained in Chapter-2.

TEM studies were carried out, using a Tecnai-G^2 - 20 TEM facility operating at 200 kV. The specimens for TEM study were prepared by mechanical grinding until 100 μm followed by dimpling until 30 μm. Final thinning of the sample was done using Ar ion-beam polishing at 3–5 kV/20–40 mA and at a grazing incidence of 3° with respect to the sample surface. Analytical Transmission Electron Microscopy (ATEM), Philips CM 200 microscope, with operating voltage of 200 kV was used for SAD and EDS on Fe–Cr alloys aged at 973K.

X-ray diffraction measurements were carried using a STOE diffractometer in powder diffraction mode using Cu K-alpha source.

5.3 RESULTS

5.3.1 Isochronal studies

Positron lifetime studies were carried out on two alloys, Fe-9Cr and Fe-12Cr, in deformed condition. Figure-5.1 shows the isochronal heat treatment studies along with deformation recovery curve of pure Fe. The interest is to see the effect of Cr on recovery and possible segregation of Cr at defect sinks.

In as-deformed condition, the positron lifetimes in Fe-Cr and pure Fe samples are 147 ps and 154 ps, respectively. Since the lifetime of positron in defect-free Fe and Fe-Cr alloys is 108 ± 2 ps, the higher lifetimes in as-deformed condition is due to vacancies and dislocations produced during deformation.

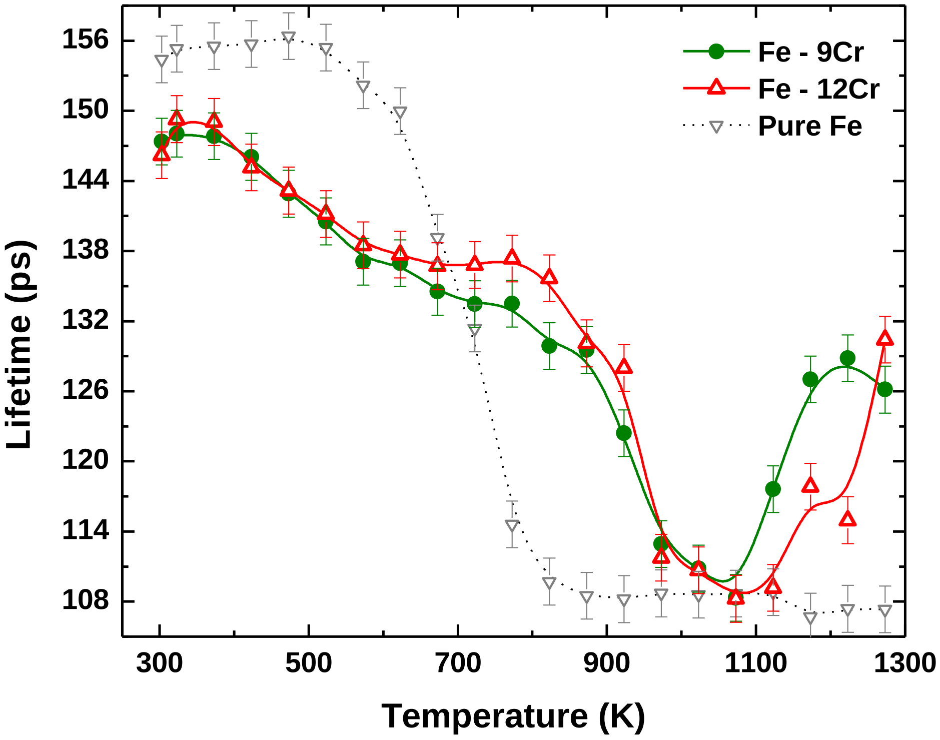

Figure-5.1: Positron lifetime in Fe-9Cr, Fe-12Cr alloys in deformed condition, as a function of treatment temperature. Also, plotted is lifetime in deformed pure Iron as a function of treatment temperature. The line through the data point is a guide to the eye.

The calculated lifetime of positron in edge dislocation and in jog on the edge dislocation in Fe is found to be 119 ± 3 and 117 ps [7, 8, 9, 10], respectively. Hence, pure dislocations cannot explain the observed positron lifetime in pure Fe. On the other hand, the lifetime value of vacancies trapped at a dislocation core, 145 ± 2 ps [7, 11], compares well with our experimental value and hence, the saturation positron lifetime observed in cold worked Fe is assigned to vacancies trapped in dislocations. Henceforth, it is implied that positron trapping or annihilation at a dislocation means annihilation at vacancies associated with dislocations. The present lifetime value is also consistent with reported experimental value of 158 ps for deformed Fe [12]. Similarly, vacancy trapped dislocations are considered responsible for higher lifetime in Fe-Cr alloys also.

In the case of pure Fe, the lifetime remains constant until 523 K and starts decreasing sharply beyond 673 K. The decrease in lifetime between 523 and 823 K can be understood as annealing of dislocations along with associated vacancies. It reaches the defect-free Fe value, i.e. 108 ps, beyond 823 K, indicating recovery of deformation defects. Above 1185 K iron will be converted to the FCC phase. Though there is a structural phase transition from FCC to BCC in the cooling process, when the heat treatment temperature is beyond 1185 K, lifetime shows only a marginal change from the bulk value of the BCC phase.

However, recovery stages as shown by positron lifetime in Fe-(9, 12)Cr alloys showed mainly three differences as compared to pure Fe samples. (i) The decrease in lifetime is apparent at temperature as low as 423 K unlike the case of pure Fe. (ii) The recovery of deformation defects showed distinct changes in Fe-Cr alloys with respect to pure Fe between temperatures 673 K and 973 K. It should also be noted that the lifetime is higher in Fe-12 Cr alloy during this stage as compared to Fe-9Cr alloy. (iii) Formation of fresh open volume defects for treatment temperature ≥ 1123 K.

Regarding the open volume defects formation for treatment above 1123 K, it was known that Fe-Cr alloys with Cr concentration between 7 – 12 wt% form FCC γ-phase above 1119 K. During the quenching, the alloy transforms to BCC with sub-structure similar to martensitic structure of ferritic steels, distinct from austenitic coarse grain structure. It also consists of high density of dislocations. Therefore, these quenched-in defects during phase transformation are responsible for the higher lifetime observed for treatment temperatures above 1123 K. For temperature as low as 423 K, the decrease in lifetime is noticeable. It could be possible that the deformed Fe contains large number of defects causing saturation trapping while the production of defects is less in Fe-Cr alloys. Hence, the annealing of defects cause change in lifetime at relatively lower temperature in the Fe-Cr alloys.

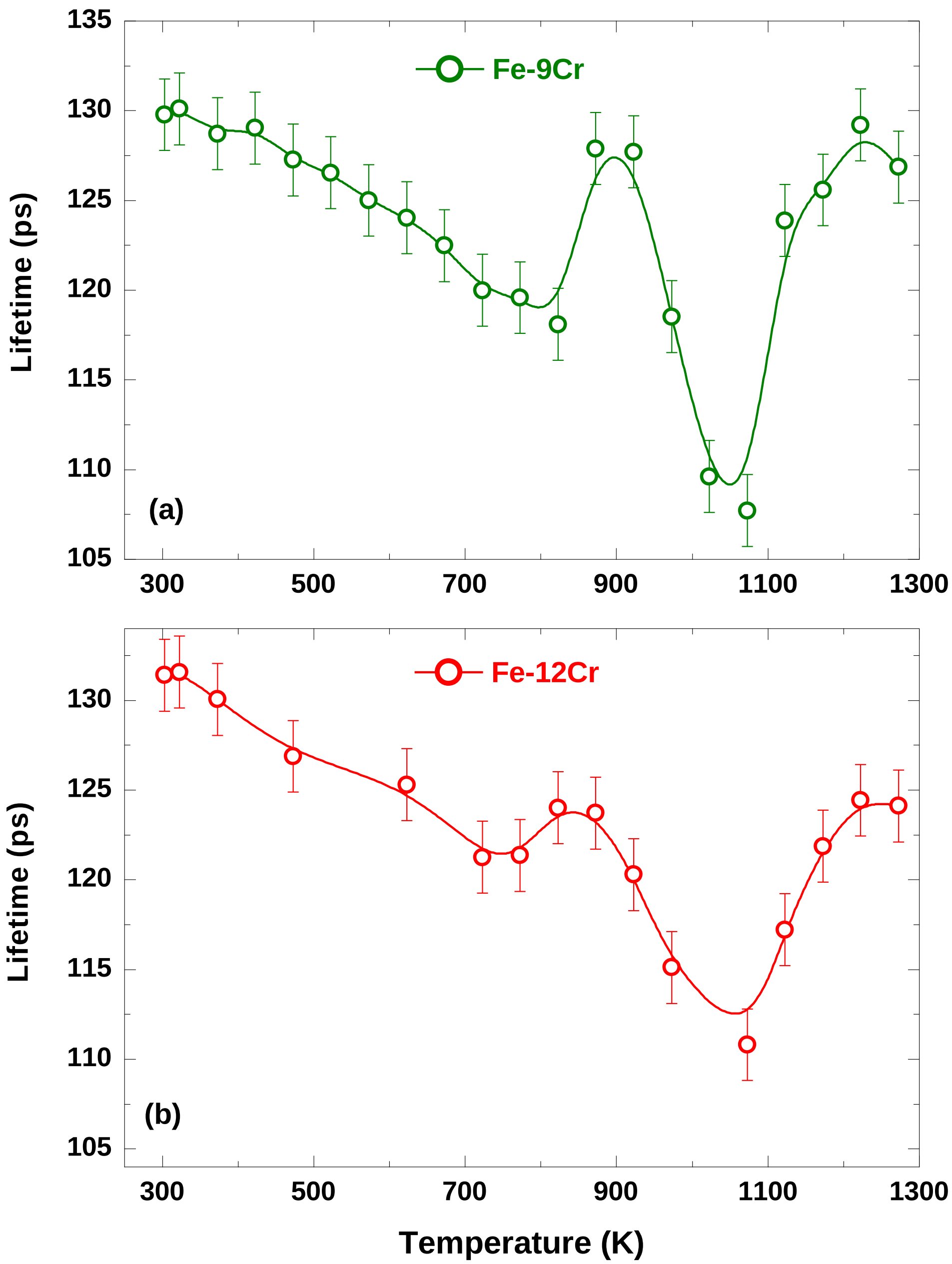

Figure-5.2: Positron lifetime as a function of isochronal heat treatment in (a) Fe-9Cr and (b) Fe-12 Cr alloy quenched from high temperature FCC phase at 1423 K. Explicit stage of increase in lifetime above 773 K indicates the formation of fresh open volume defects corresponding to precipitate-matrix interfaces.

The extended higher lifetime between temperatures 673 K and 973 K is considered either sluggish dislocation motion due to presence of Cr in solid solution or fresh formation of open volume defects of different kind. To identify the exact reason, isochronal studies with initial condition of quenching are carried. The positron lifetime in Fe-9Cr and Fe-12Cr samples as a function of isochronal heat treatment temperature is shown in Figure-5.2(a, b). The result showed the annealing out of quenched-in defects below 773 K and an explicit stage where an increase in positron lifetime is observed above 773 K, indicating the formation of fresh open volume defects in the temperature range of 823 - 973 K and 773 - 973 K in Fe-9Cr and Fe-12 Cr alloys, respectively. If the extended higher lifetime is only due to Cr in solid solution, it should only retard the annealing out of dislocations. However, increase in lifetime strengthens the consideration of possibility of associated defects with Cr precipitation. These defects are, however, found decreasing above 973 K in both the alloys.

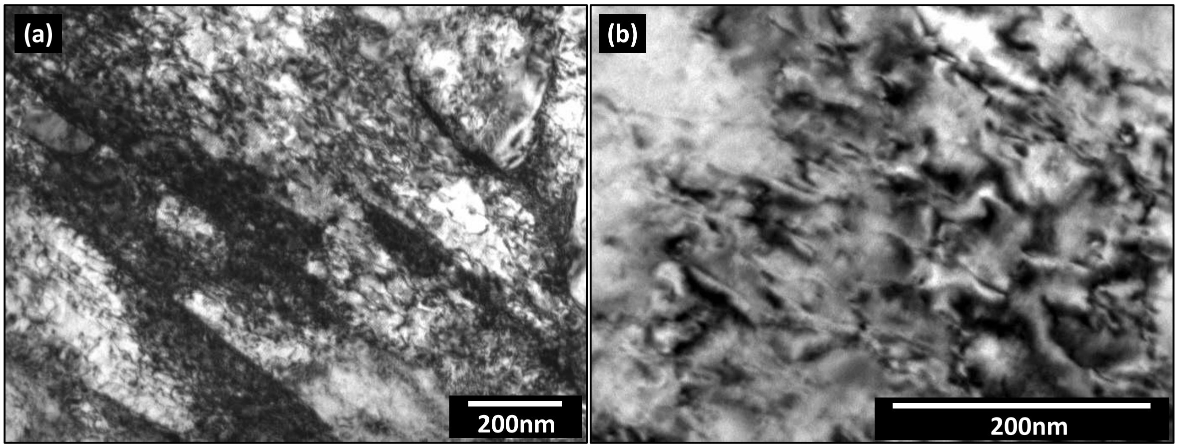

Figure-5.3: TEM micrographs of (a) lath structure and (b) high density of random dislocations in as-quenched Fe-9Cr alloy. The contrast seen suggests high concentration of randomly oriented dislocations in the alloy.

It should be noted that the increase in lifetime is seen at 773 K in the case of Fe-12Cr alloy, where as in Fe-9Cr alloy it is observed only beyond 823 K. On the other hand, the lifetime of Fe-9Cr alloy corresponding to formation of open volume defects during 823 – 973

K is larger than that in the case of Fe-12Cr for the same stage. Cr rich α' phase formation is know in ferritic steels containing Cr concentration above 12% [2] however, the surprising similarity in results of Fe-9Cr alloy promoted TEM studies of Fe-9Cr alloys at representative temperatures, corresponding to lifetime variations. The TEM micrographs of as-quenched alloy are seen in Figure-5.3. The structure of as-quenched sample is seen with martensitic laths of 150 nm width. The lath structure consisted of high number density of dislocations inside and at the boundaries of laths. These observations are consistent with literature [5, 13, 14].

The TEM micrograph of sample annealed at 773 K is shown in Figure-5.4. The lath structure is retained at this temperature but, the dislocation density decreased significantly. This is consistent with the decrease in positron lifetime until 773 K, indicating that dislocations are responsible for higher lifetime in as-quenched state. It should also be noted that significant number of dislocation loops (Figure-5.4(b)) are found in this sample following annealing out of random dislocations.

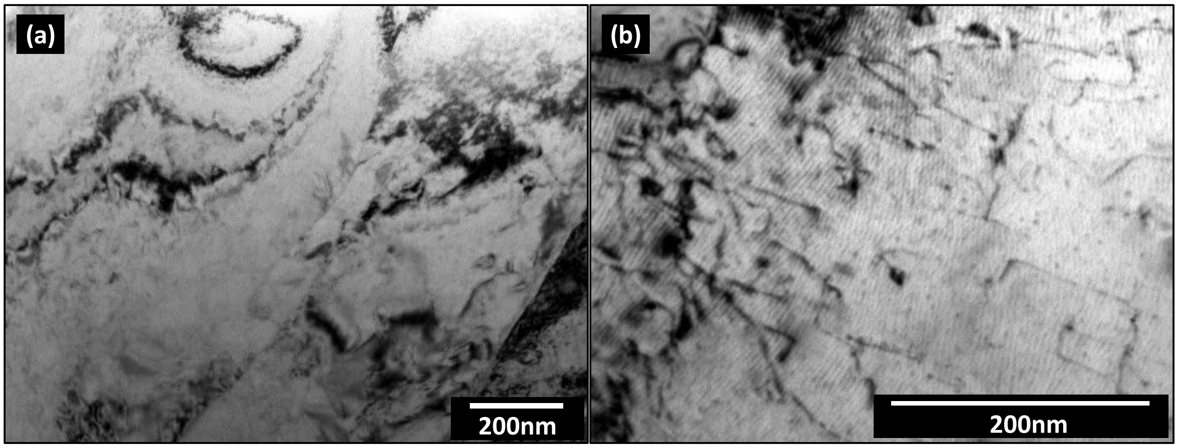

Figure-5.4: TEM micrographs of quenched Fe-9Cr alloy after treatment at 773 K. Significant decrease in random dislocations can be seen. Formation of dislocation loops can be observed in micrograph (b).

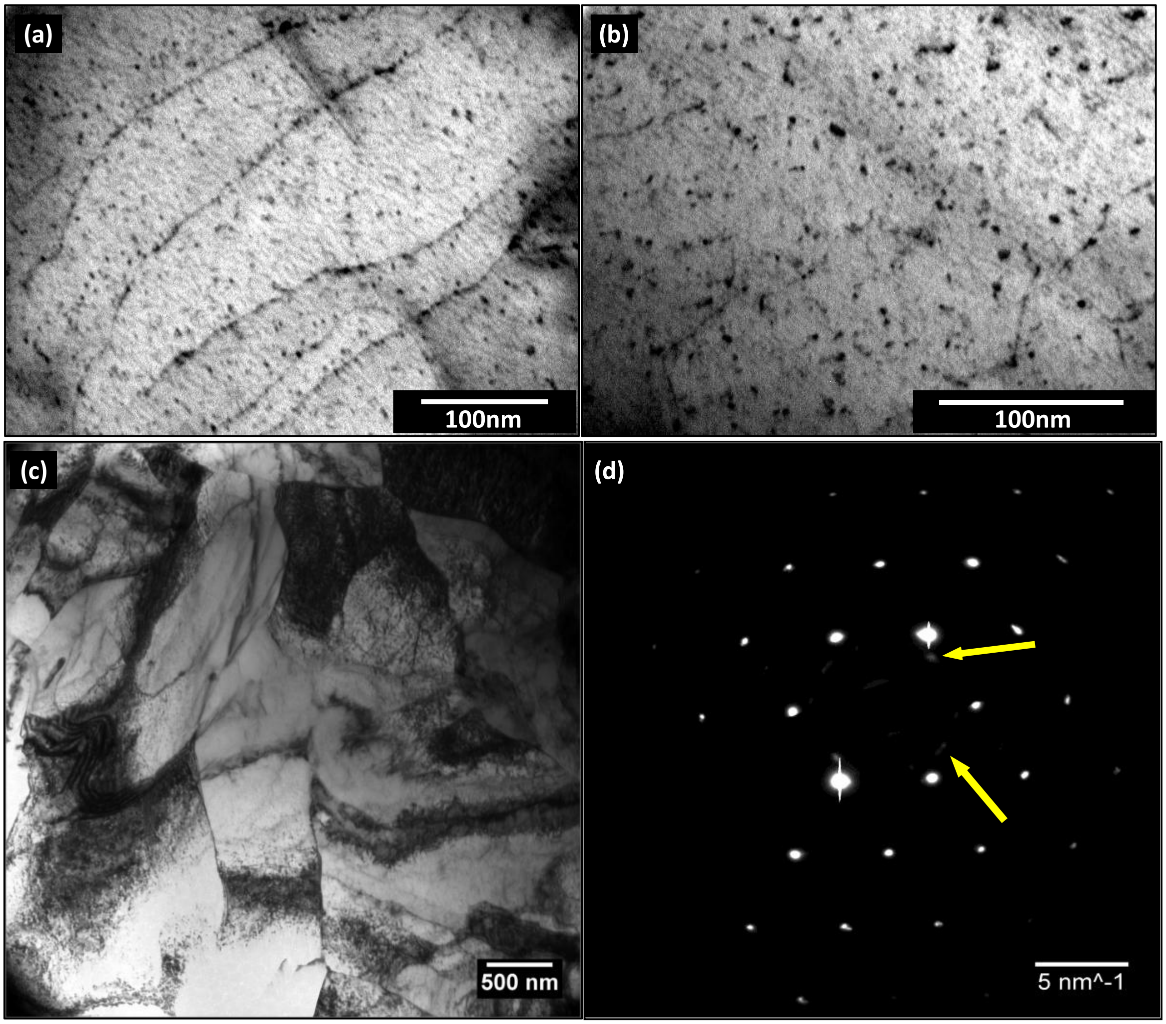

Figure-5.5: TEM micrographs of quenched Fe-9Cr alloys after treatment at 900 K. (a, b) Precipitates are dispersed in the matrix and also at boundaries. (c) The lath structure is converted into sub-grain structure. Dislocation concentration is reduced drastically, especially, where precipitates are formed extensively. (d) SAD pattern of matrix with embedded precipitates, showing signatures of additional phase other than BCC α-phase.

TEM micrographs of sample treated at 900 K are shown in Figure-5.5. As expected, dispersed precipitation is seen throughout the matrix and is found frequently along lath, sub-grain boundaries. It also shows a negligible amount of dislocations. The micrographs suggest that the precipitates are of average size between 4 and 7 nm. The observed increase in lifetime beyond 823 K (Figure-5.2(a)) can be understood in terms of these precipitates. The interfaces between these precipitates and matrix can act as positron trapping sites, thereby increasing the mean positron lifetime. It is also found from Figure-5.5(c) that the lath structure change to sub-grain structure at 900 K. Figure-5.5(d) shows the SAD pattern of the matrix with embedded precipitates. The details will be discussed later.

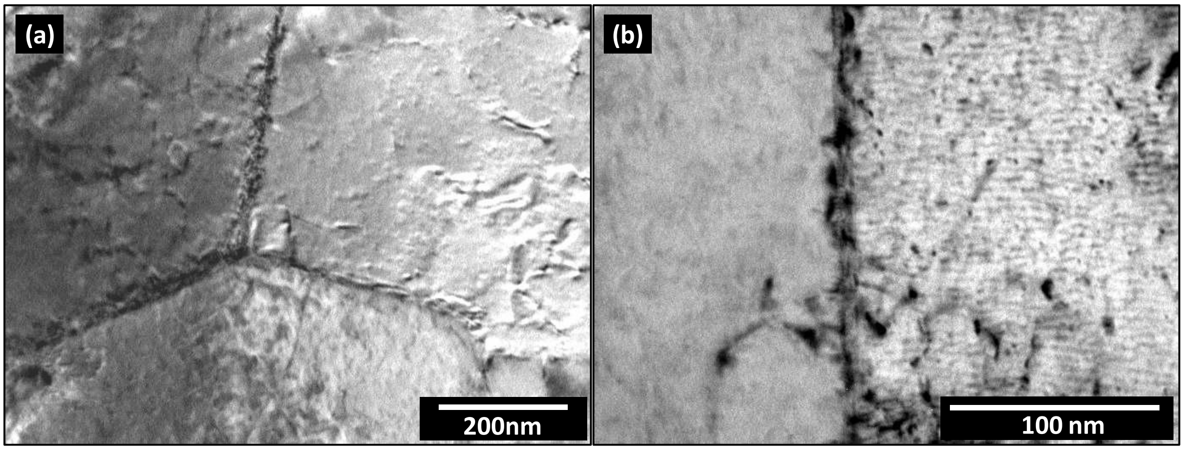

Figure-5.6: TEM micrographs of quenched Fe-9Cr alloy after treatment at 973 K. (a) Equiaxed grain formation is seen with precipitates dissolved in to the matrix. (b) Occasionally the sub-structure is observed with precipitates. However the precipitates are fewer in number density.

To enhance the understanding of the nature of possible interfacial traps, positron lifetime calculations were carried out for the defect-free Fe–Cr [100] oriented interface as well as for Cr and Fe vacancies at the interfacial region [10]. These calculations are carried out using the atomic superposition method, as implemented in MIKA Doppler code [15]. For the defect-free Fe–Cr interface, positron lifetime is observed to be 112 ps and positrons preferentially annihilate in the Fe region. Based on this, it is understood that defect-free coherent Cr precipitates cannot trap positrons, owing to lesser positron affinity for Cr than Fe [16]. The presence of vacancies, either in a Cr cluster or at the Fe/Cr interface region, are possible trapping sites, according to the positron lifetime calculation results (178 – 188 ps).

However, the experimental lifetime could not be resolved into components indicating no such higher lifetime component, corresponding to pure vacancies, exists. The observed experimental lifetime at 900 K is rather large compared to the bulk Fe–Cr defect-free value (112 ps), indicating open volume trapping sites at the interface. In this context, these precipitates are considered to be incoherent with the matrix.

Figure-5.6(a, b) shows the microstructure of sample treated at 973 K. It shows significant recovery of grain structure along with dissolution of precipitates. However, occasionally, the sub-grain structure still persists with precipitates dispersed. Figure-5.6(b) shows one such interface where, at one side the precipitates are dissolved and grain growth occurred and on the other side precipitates exist. Almost complete dissolution observed in sample treated at 1073 K.

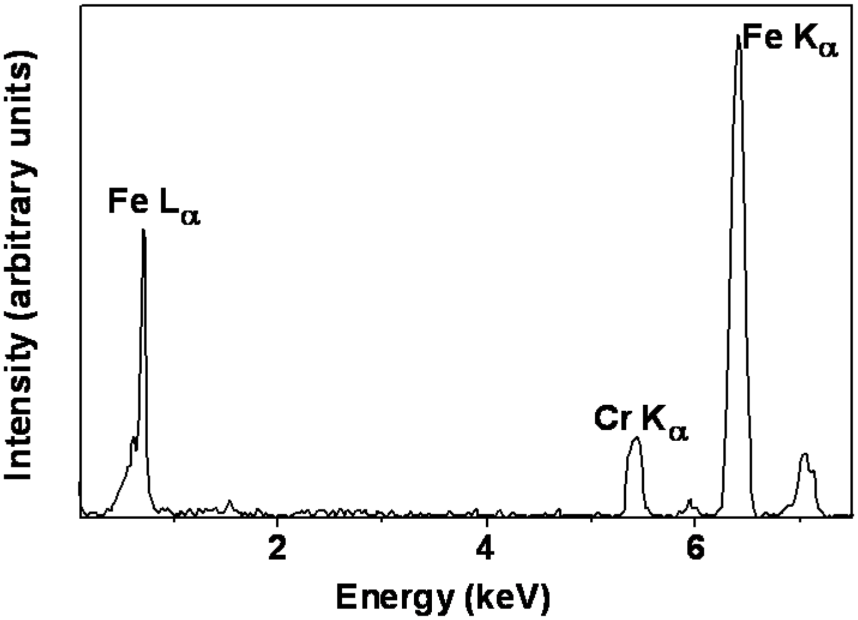

Figure-5.7: Energy-dispersed X-ray spectrum of a precipitate embedded in matrix of Fe-9Cr alloy treated at 900 K.

The decrease in lifetime above 923 K and dissolution of precipitates at temperature ≥ 973 K are consistent to show that these precipitates are responsible for higher lifetime.

To understand the nature of precipitates observed at 900 K treated Fe-9Cr alloy, EDS and SAD structures were carried using ATEM. The EDS spectrum obtained with a beam spot size of 7.5 nm (taken on a specific precipitate of size around 5 nm) is shown in Figure-5.7 with characteristic Fe and Cr peaks. The Cr concentration obtained is 12.6 ± 1.0 wt%, while the Cr concentration away from the precipitate in the matrix is found to be 8.9 ± 0.7 wt%. As the size of precipitates is smaller than the beam spot size and the film thickness is of the order of a few tens of nm, the effective volume of precipitate is smaller compared to the matrix volume probed by EDS. Given the above considerations, for the variation in the observed Cr concentration it is reasonable to ascribe that these precipitates are Cr rich in nature.

Figure-5.5(d) shows the SAD pattern of the matrix with embedded precipitates. The diffraction pattern shows an additional phase, other than BCC α-Fe/Cr, with a d-spacing value of 1.26 ± 0.12 Å. From JCPDS data, this value is consistent with both σ-phases of Fe-Cr as well as Fe–Cr carbides. In either case, the observation is consistent with positron trapping at interfaces as they cannot be coherent with the matrix. Formation of carbides is known due to supersaturation of carbon in the BCC phase. In the present case, the concentration of carbon is well below the solubility limits and further, carbide precipitates are known to be stable and cannot dissolve around 973 K, as observed in the present case. Thus, the current observations indicate that these are not carbide precipitates. Therefore, we attribute these precipitates to be Cr rich clusters occurring in the Fe matrix. It is also interesting to note that the lower and upper limits of formation of the σ-phase in the Fe-Cr system, as discussed in the recent review [17], is in good agreement with the temperature range of Cr clustering in the present study (Figure-5.2). However, the nature of phase will be further discussed in later part of this chapter.

Figure-5.8 shows the hardness of Fe-9Cr alloys, with initial condition of air-quenching, measured at representative treatment temperatures corresponding to lifetime changes. The as-quenched alloy is harder (~ 290 HV), as compared to solid solution strength, due to martensitic lath structure. It gradually decreased until 1023 K, indicating recovery of the lath structure into equiaxed coarse grain structure with increasing temperature. The apparent effect of precipitates is not noticed. It is consistent with the literature that, in ferritic/martensitic alloys the lath/sub-grain structure contribute significantly larger to hardness/strength, as compared to the precipitates [18, 19]. Also, the observed precipitates are very fine in size to effectively hinder the dislocation motion.

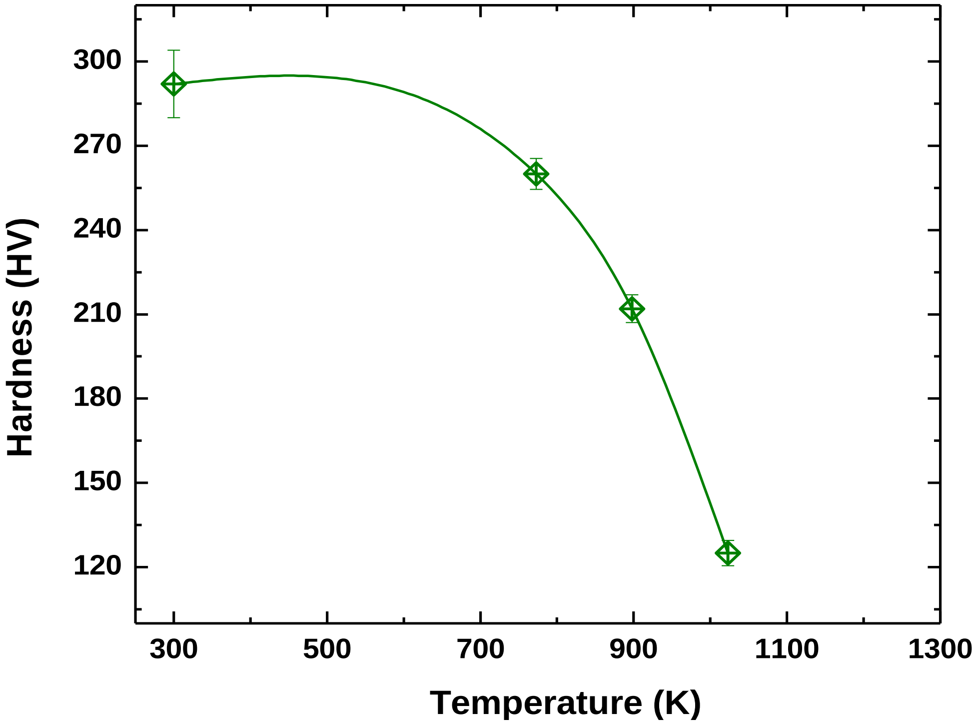

Figure-5.8: Hardness of Fe-9Cr alloy in as-quenched and subsequently heat treated at 773, 873, 1023 K. The line through the data point is a guide to the eye.

XRD spectrum also showed evidence towards the recovery of martensitic structure from variations in peak broadening (Figure-5.9). The peak broadening decreased from as-quenched alloy to 873 K and 1073 K treated alloy.

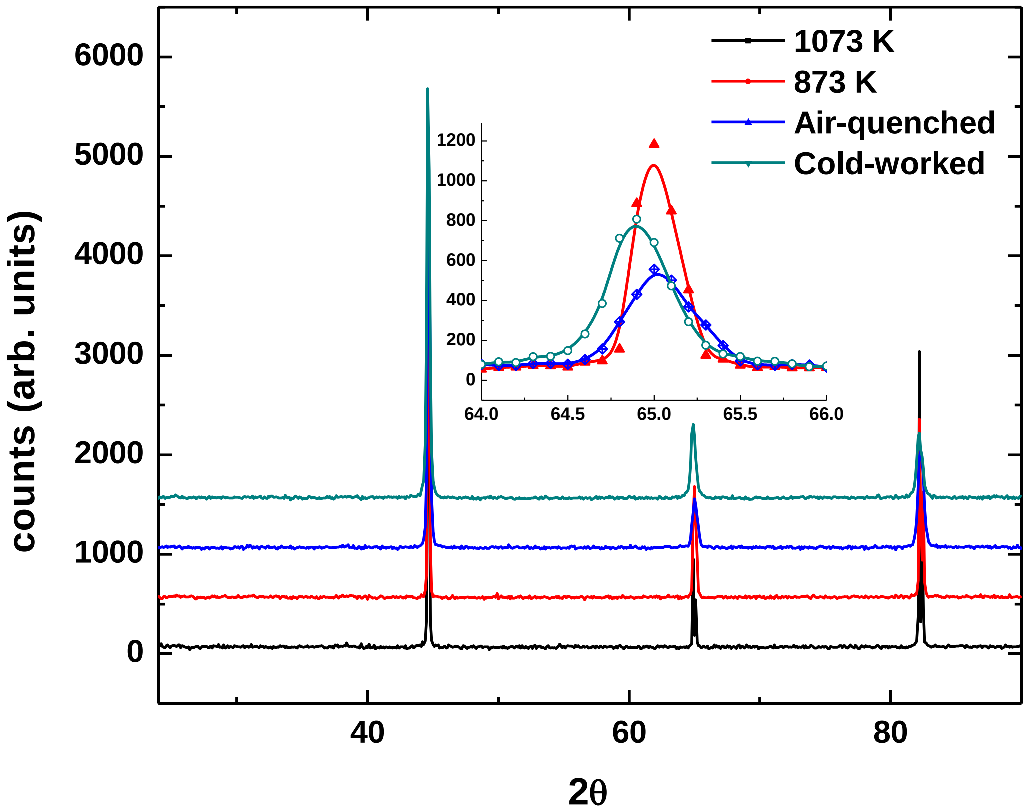

Figure-5.9: X-ray diffraction pattern of Fe-9Cr alloy in quenched state, subsequently treated at 873 and 1073 K. Peak broadening (inset) is shown as evidence for fine lath structure in quenched alloy. 20% deformed alloy also shown for comparison. The quenched sample showed relatively larger broadening than deformed alloy. No signature of precipitation is observed in the XRD pattern.

Further, to bring out the effects of dislocations and martensitic lath structure on Cr precipitation, lifetime studies with isochronal heat treatments are carried out on Fe-9Cr alloy with the homogenized condition i.e., dislocation-free coarse grain structure, as initial condition. The results are shown in Figure-5.10. The as-prepared defect-free alloy showed bulk lifetime and it remained constant until the treatment temperature is above 1073 K. Due to absence of dislocations and associated vacancy-defects, reduction in lifetime is not seen below 823 K. Further, the lifetime did not show any changes during 823 and 1023 K, as seen in air-quenched alloy (Figure-5.2(a)), indicating the absence of the precipitation stage. These results show that dislocation-free coarse grained structure did not lead to Cr precipitation.

This also suggests that the precipitates observed are not carbides, as they are expected to form with this initial condition also, if it is due to supersaturation of carbon.

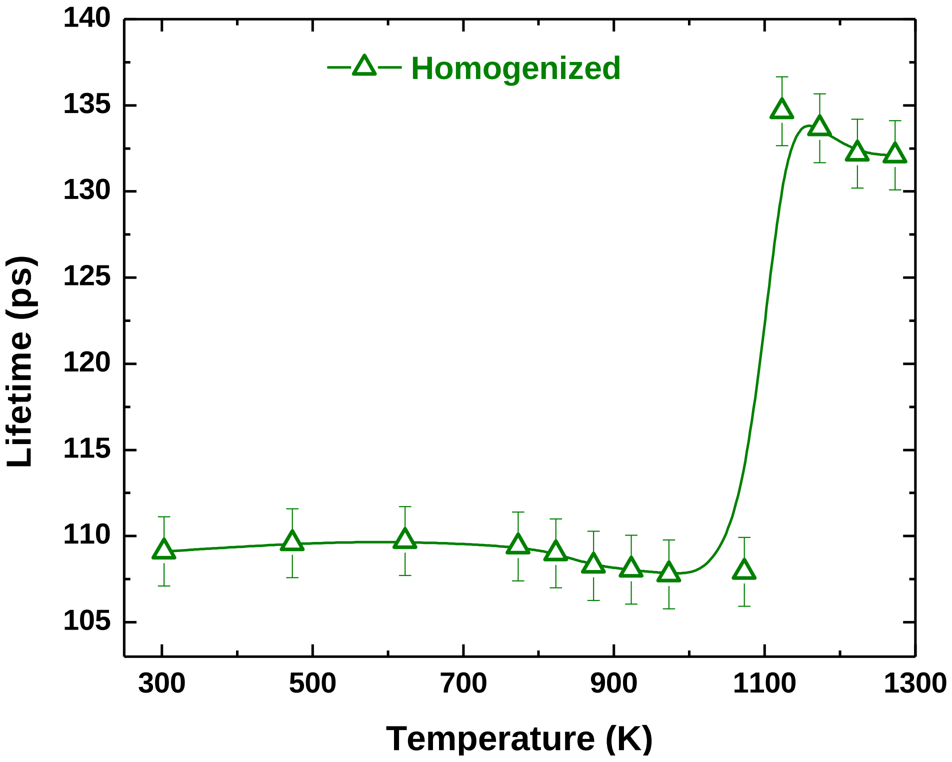

Figure-5.10: Positron lifetime as a function of isochronal heat treatment in homogenized Fe-9Cr alloy. The stage corresponding to the precipitation is not observed.

With regard to the observations of Cr precipitates in air-quenched alloys (Figure-5.5), Matijasevic and Almazouzi [13] found similar TEM contrast in neutron irradiated samples and ascribed them as radiation induced solute-defect clusters and their initial microstructure is similar to the microstructure observed in the present study. Incoherent precipitate formation at grain boundaries can be understood as fresh nucleation and growth. However, intra-granular incoherent precipitation is surprising. The mechanism of formation is believed to be dislocations acting as nucleating sites and by solute sweeping during dislocation recovery similar to a proposal by Kesternich [20]. Accordingly, the precipitation of Cr is observed during the annealing out of pre-existing dislocations. According to the proposed mechanism moving dislocations sweep along solute atoms (if the solute atoms binding energy with dislocations is positive) until they react or two dislocations annihilate leaving a locally enhanced concentration. The observed higher precipitate density along lath boundaries can be understood due to annealing of dislocations at lath boundaries.

The above observations confirm that the precipitation is followed by dislocation motion/annealing. The precipitates are Cr rich in nature and they are associated with open volume defects i.e. the precipitates are incoherent with matrix.

5.3.2 Isothermal Studies

The fact that the treatment time is 1 h during isochronal studies prompted further isothermal studies to investigate the temperature range at which the precipitates are stable. Figure-5.11(a, b, c, d) showed lifetime values in isothermally (at 723, 748, 773 and 873 K) treated Fe-9Cr alloys, with air-quenching as initial condition. Figure-5.11(a, b, c), for treatment temperatures of 723, 748 and 773 K, showed similar nature of decreasing lifetime followed by increase and saturation, with time. The decrease and increase can be understood as dislocation annealing dominated and precipitation dominated stages, respectively. It is found that isothermal treatment at 748 K and 773 K saturated the lifetime before 70 and 28 h, respectively. However, lifetime did not saturate in alloy treated at 723 K for 103 h. Saturation (128 ± 2 ps) occurred by treating further at 773 K for 2 h and additional treatment for 13 h at 773 K did not change lifetime. It indicates that the segregation process is significantly slow below 723 K.

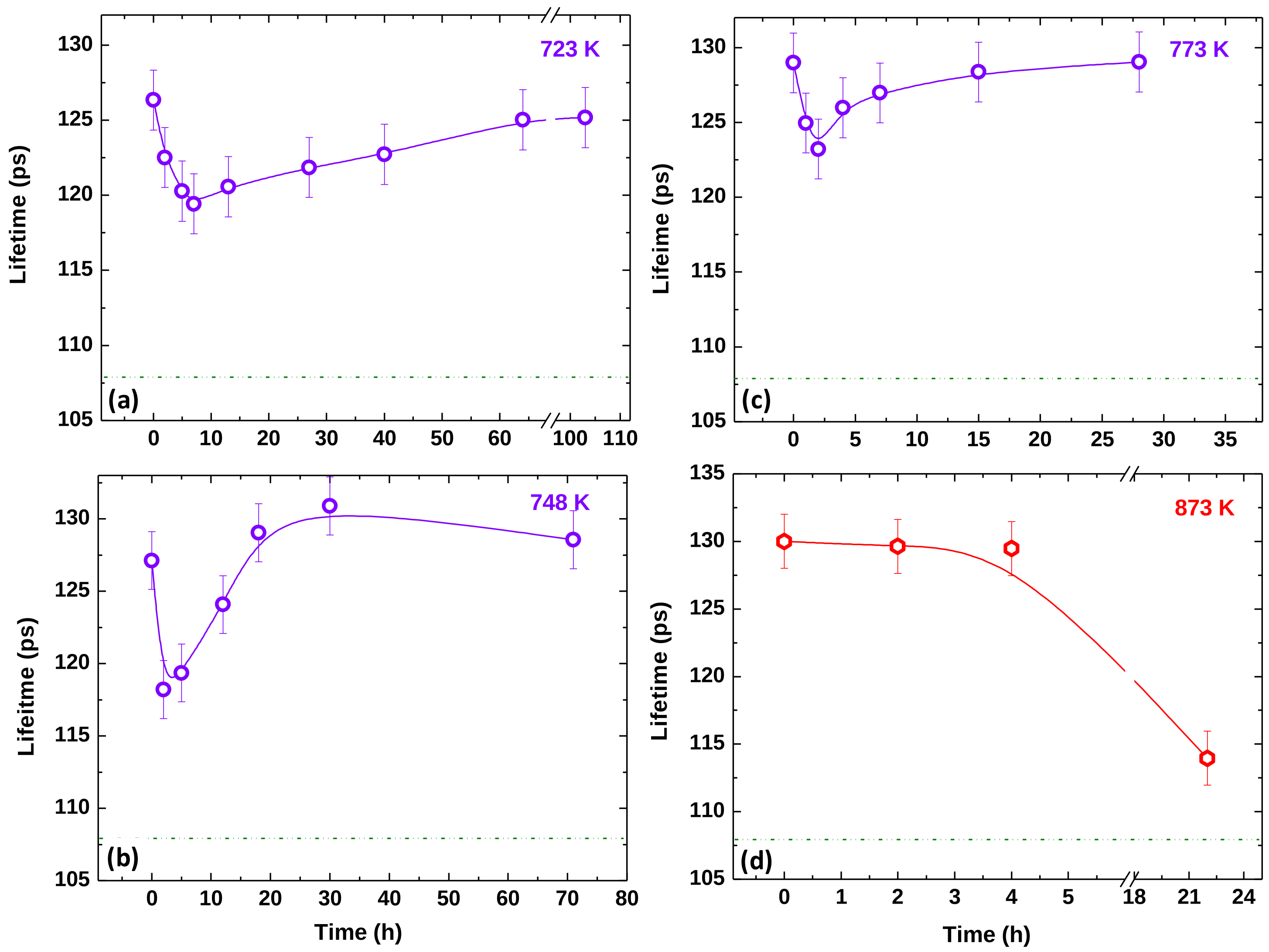

Figure-5.11: Positron lifetime as a function of isothermal heat treatment in air-quenched Fe-9Cr alloy at (a) 723 K (b) 748 K (c) 773 K and (d) 873 K. The line through the data point is a guide to the eye. The initial decrease is due to annealing of quenched in defects and increase corresponds to precipitation. Dashed line in the graph shows defect free bulk lifetime value.

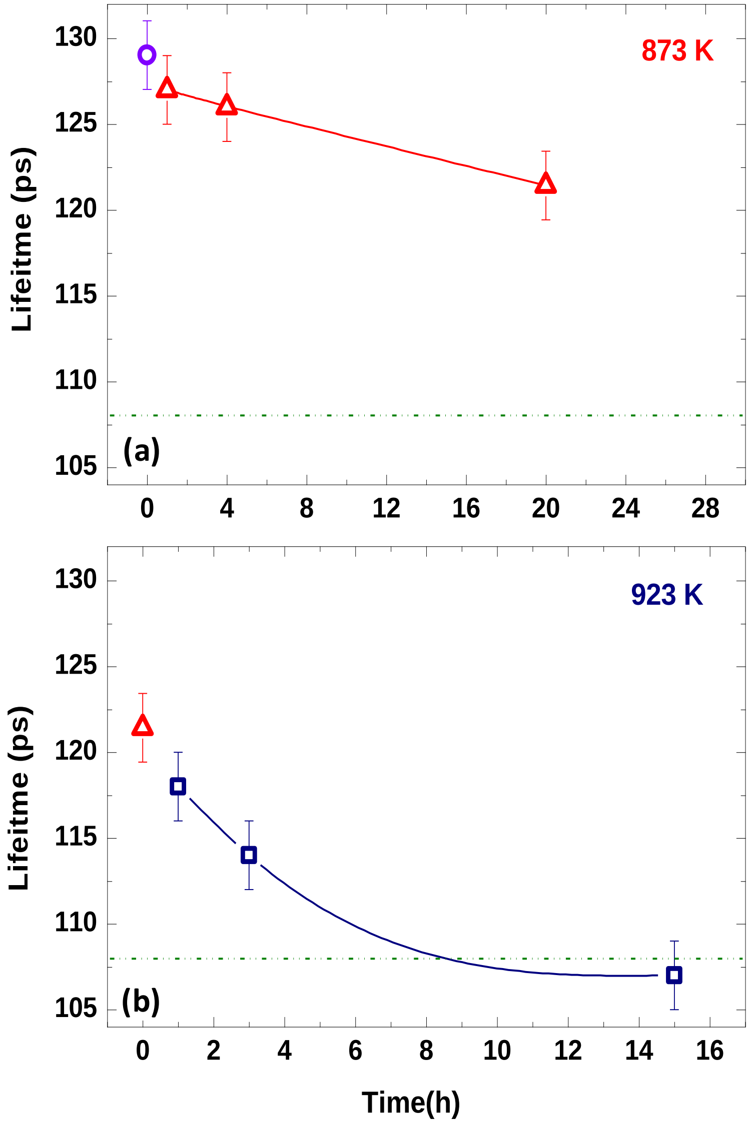

Figure-5.12: (a) Positron lifetime in Fe-9Cr alloy as a function of isothermal heat treatment at 873 K (which is treated prior at 773 K for 28 h, shown in figure-5.11(c)). (b) After 20 h of treatment at 873 K, the same sample is treated isothermally at 923 K. The initial values of lifetime indicate the lifetime in alloy at the end of previous treatment. Dashed line in the graph shows defect-free bulk lifetime value.

Unlike at other three temperatures, isothermal treatment at 873 K (Figure-5.11(d)) showed saturation of lifetime for just 2 h and starts decreasing for ageing time higher than 4 h, indicating that the precipitates are unstable at 873 K. To show that the precipitates formed at 873 K are not stable, the alloy treated at 773 K for 28 h is further treated at 873 K. The results are presented in Figure-5.12(a). The results show that the decrease in lifetime is slow in alloy treated prior at 773 K i.e. the lifetime reached 114 ps after 22 h in the case of 873 K isothermally treated alloy (Figure-5.11(d)) but, the lifetime retained above 120 ps after 20 h in the case of alloy prior treated at 773 K. Further treatment at 923 K (Figure-5.12(b)) for more than 3 h brought the lifetime equal to bulk lifetime indicating almost complete dissolution of precipitates into the matrix. These results suggest that the precipitates are unstable at temperature above 873 K and the alloy tends towards homogenized α-phase as known in Fe-Cr equilibrium phase diagram.

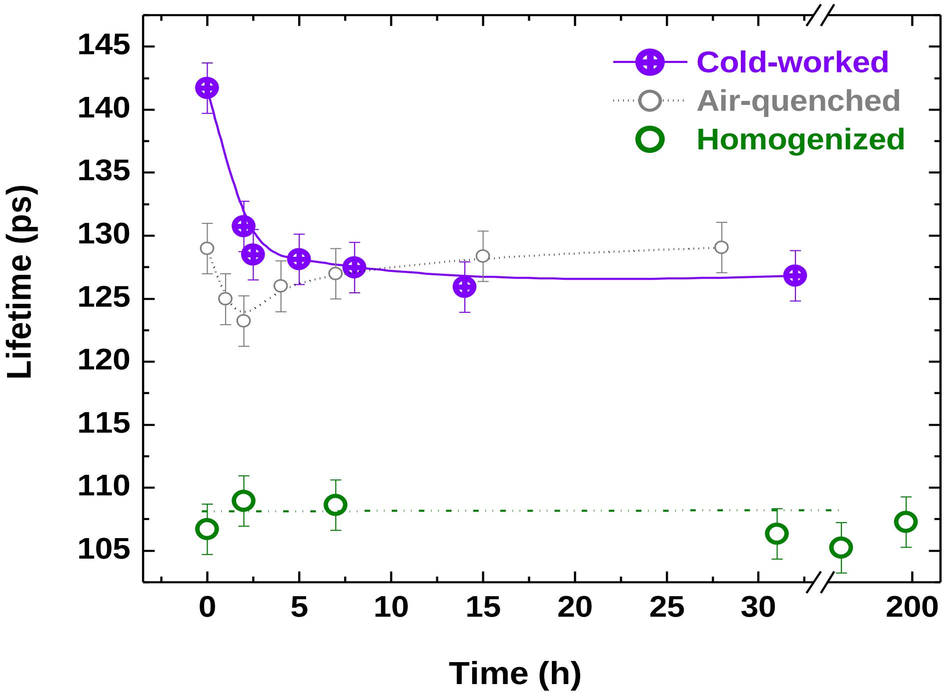

Figure-5.13: Positron lifetime in Fe-9Cr alloy, as a function ageing time, with three initial conditions i.e. (i) quenched (ii) homogenized and (iii) homogenization followed by deformation. Ageing was carried at 773 K for quenched and deformed alloys while for homogenized condition ageing was carried out at 748 K. Dashed line in the graph shows defect-free bulk lifetime value. While dislocation containing alloys showed precipitation, homogenized alloy did not show precipitation even for 184 h.

To explicitly show that the dislocations drive the Cr clustering, lifetime in isothermally aged Fe-9Cr alloys with dislocations and without dislocations are compared. Alloys in three different initial conditions (i) quenched (ii) homogenized at 1073 K and (iii) deformed after homogenization at 1073 K are isothermally aged and lifetime measured at different intervals. Figure-5.13 shows the results. Lifetime in dislocation-free homogenized alloy did not show changes with ageing up to 184 h while deformed and air-quenched alloys showed decrease in open volume defects and saturation of lifetime, below 15 h of ageing, corresponding to precipitates.

These results suggest that dislocations play a crucial role in Cr precipitation, to accelerate the Cr segregation. It should also be noted that saturation occurred faster in quenched alloy as compared to deformed alloy indicating that the martensitic structure accelerates precipitation process.

5.3.3 Verification test

From the results of isothermal studies at 873 K (Figure-5-11(d)), it is understandable that with martensitic lath structure as initial structure, precipitates form at lower ageing times and they dissolve at higher ageing times to attain equilibrium for treatment at 873 K. If it is the case, isochronal studies of deformed Fe-(9, 12)Cr alloys (Figure-5.1) should contain precipitates prior to deformation. So, to prove that and to verify the positron lifetime variations with only deformation defects as initial condition, isochronal studies are carried on alloys which are homogenized at 1073 K followed by deformation. The results are shown in Figure-5.14. As expected, there are differences in lifetimes over temperature range up to 1023 K, as compared to alloy quenched and treated at 873 K for 3 h before deformation (Figure-5.1). The lifetime in alloy with this condition is less compared to alloy containing precipitates in the initial state (Figure-5.1) over a wide temperature range. It is explicitly seen that when the treatment temperature is beyond 823 K, where the lifetime decreases sharply indicating that the fresh precipitates formed are not stable at higher temperatures.

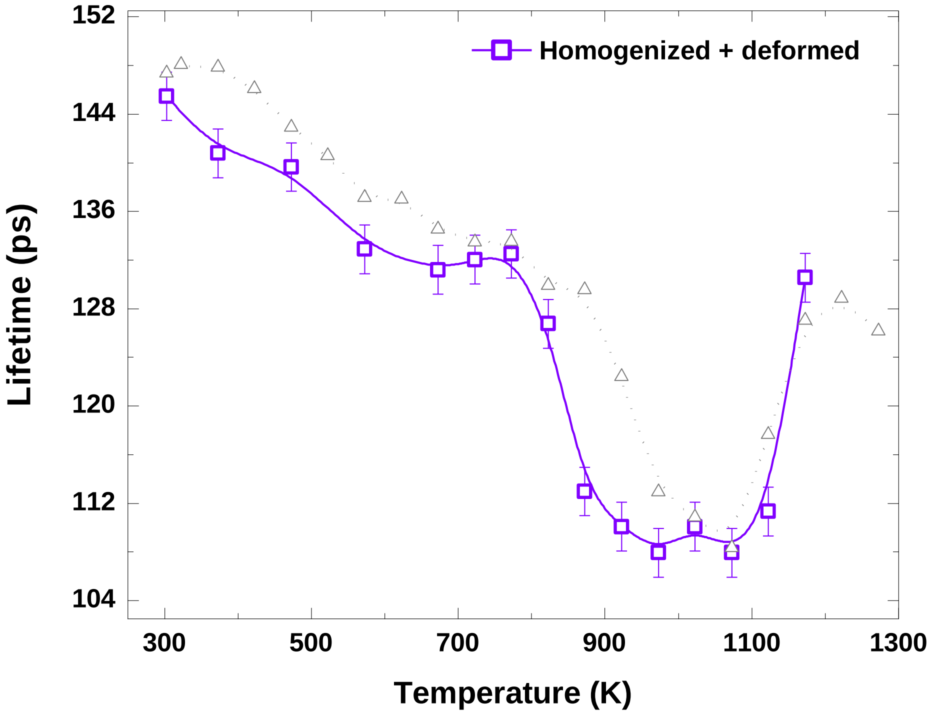

Figure-5.14: Positron lifetime in Fe-9Cr alloy in homogenized and deformed condition, as a function of treatment temperature. Results of deformed alloy, after air-quenched + 873 K (3h) treatment (open triangles) are also presented for reference.

As a summary, it is found that quenched-in defects and deformation defects leads to accelerated precipitation of Cr in Fe-(9, 12)Cr alloys. The quenched-in defects with martensitic lath structure are found to be more effective than deformation induced defects in Cr segregation.

5.3.4 On the nature of Cr precipitates

Having found that dislocations influence Cr segregation, the nature of phase formed due to segregation of Cr is investigated. It also discusses the dependence of Cr concentration on segregation.

The effect of Cr concentration on quenching from 1273 K to room temperature is discussed to classify the sample. Figure-5.15(a) shows the hardness of Fe-Cr alloys, as a function of Cr concentration, in homogenized condition (dislocation-free coarse grained structure) and in quenched condition. In Fe-9Cr and Fe-9.5Cr alloys the quenched condition produced significant deviation in hardness, as compared to homogenized condition. The increase in hardness can be understood due to the formation of martensitic lath structure in Fe-Cr binary alloys with Cr concentration around 10 wt% [5]. It is known that the cooling kinetics is slow around 10% Cr binary alloys and result in martensitic phase formation for air-quenching [5]. Correspondingly, the positron lifetime (Figure-5.15(b)) also showed higher values for quenched condition, for the same concentration range. The open volume defects associated with martensitic structure are responsible for larger lifetime. They are further pronounced in area normalized Doppler broadening spectra which are subtracted from area normalized annealed pure Fe spectrum (Figure-5.16). The increase in low momentum (close to 511 keV) distribution corresponds to increase in open volume defects. Effect of Cr atoms on the distribution was measured using defect-free homogenized samples and found that it is significantly low compared to changes noticed in Figure-5.16. Hence, the change in positron annihilation characteristics is only due to the defects. As it is seen in lifetime, significant difference is seen in Fe-9Cr, Fe-9.5Cr and Fe 12Cr samples showing the signature of open volume defects with increase in low momentum distribution.

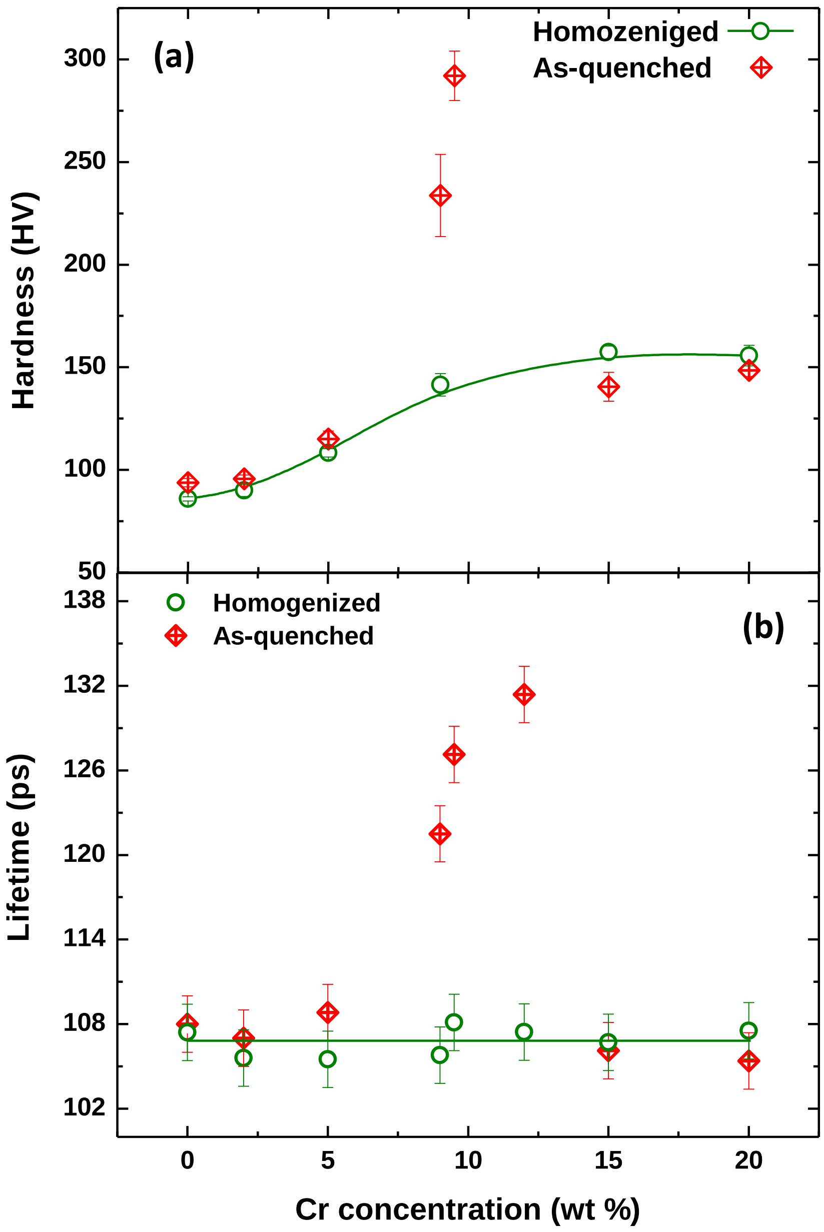

Figure-5.15: (a) Hardness of Fe-Cr alloys as a function of Cr concentration is presented in homogenized condition and in quenched (from 1273 K) condition. Samples with Cr concentration above 5% only showed increase in hardness due to sub-structures inside prior austenitic grains due to slow kinetics during γ (FCC) to α (BCC) phase transition during air-quenching. However, alloys with Cr concentration above 14 wt% will be at BCC α-phase even at 1273 K. Hence, there will not be any sub-structure formation. Hardness of Fe-12Cr was not measured due to availability of limited samples. Same is the case with Fe-9.5Cr alloy in homogenized condition. (b) Corresponding lifetime values are shown for homogenized and quenched condition. Lifetime values also showed similar changes due to open volume defects associated with sub-structure.

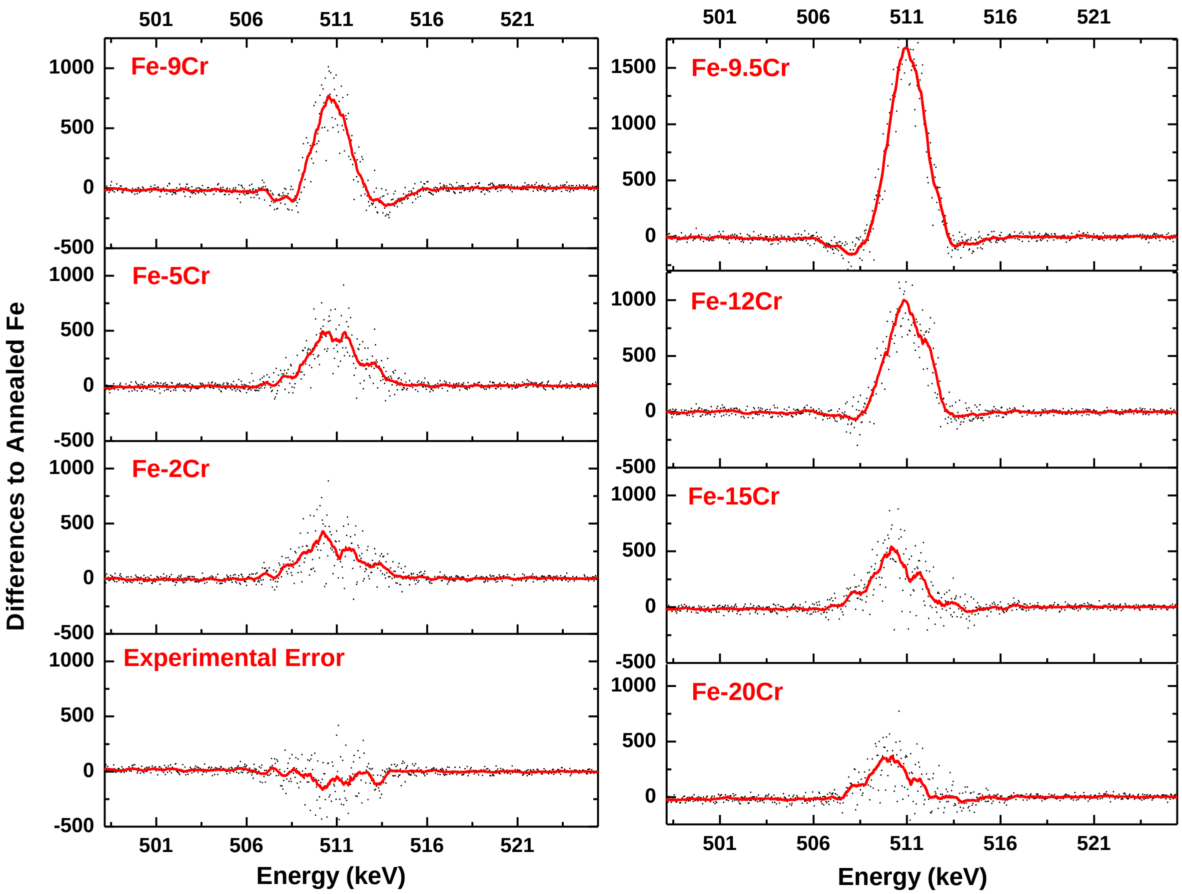

Figure-5.16: Weighted differences between counts of positron annihilation Doppler broadening spectra of quenched Fe-Cr alloys with respect to annealed pure Fe. 'Experimental error' is the difference plotted for repeat measurement of annealed pure Fe. Pronounced difference observed for alloys of 9, 9.5 and 12% Cr concentration, due to associated defects with martensitic structure. It should be noted that unlike lifetime, small but consistent change is observed in other alloys also. Thus, Doppler broadening is found to exhibit better sensitivity than positron lifetime.

For pure Fe and alloys of Fe-(2, 5)% Cr the hardness retained as in the case of homogenized samples, indicating that the FCC to BCC transition during quenching did not result in fine sub-grain structure that contribute to hardness. Larger ferrite grains, order of few µm, with randomly oriented grain boundaries are reported for Fe-(2, 5)% Cr alloys [13]. Lifetime values and Doppler broadening also suggest that no significant concentration

($> 10^{-7}$) of open volume defects resulted due to phase transition. Fe-(15, 20)% Cr alloys also did not show any significant changes in hardness, lifetime and Doppler broadening, because the phase at treatment temperature and the quenched temperature (300 K) is same i.e. BCC and there is no FCC phase between these temperatures (Figure-5.17). Hence, no change in microstructure is expected.

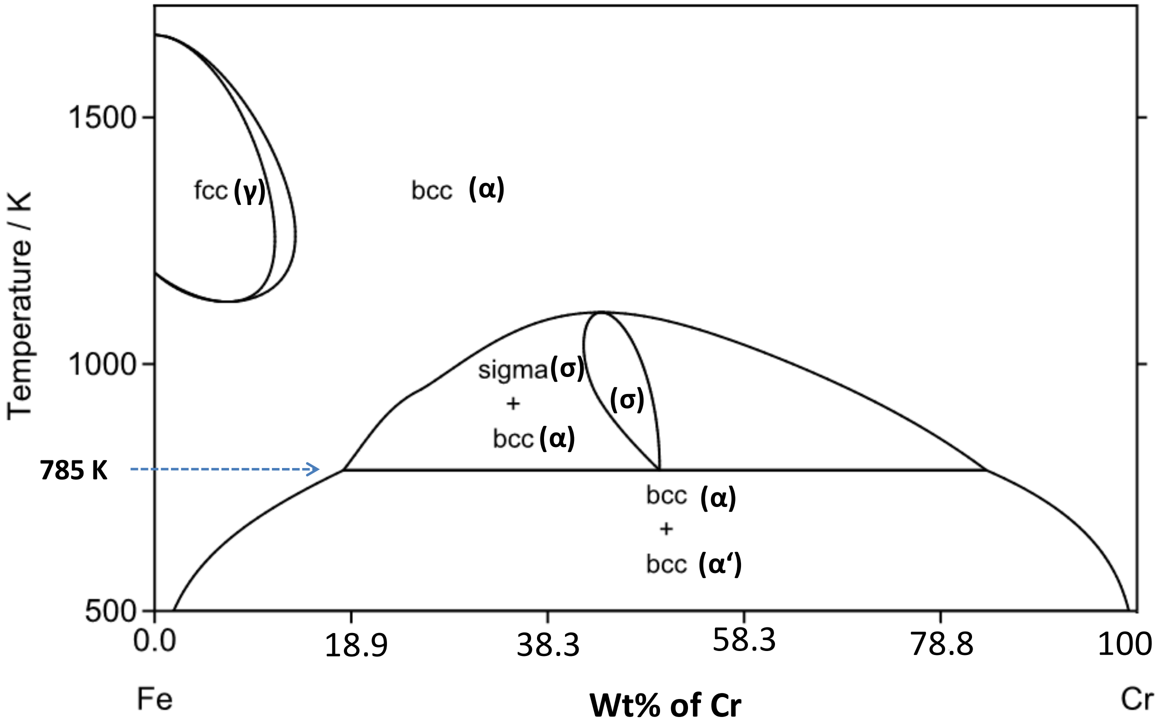

Figure-5.17: Low temperature part of Fe-Cr equilibrium phase diagram describing BCC, FCC and tetragonal (σ) phases. Fe-15Cr, Fe-20Cr alloys are out of FCC loop for 1273 K heat treatment and hence, no effect on microstructure during cooling.

For the alloys chosen for this study, there exists no equilibrium σ-phase at any temperature. However, Cr rich BCC phase i.e. α'-phase is expected for these samples at temperatures below 785 K (Figure-5.17). The kinetics of α'-phase formation increases with increase in Cr concentration. The possibility of conversion of this α'-phase into non-equilibrium σ-phase for short heat treatment at temperature above 785 K is studied.

Hence, the as-quenched Fe-(2, 5, 9, 9.5, 12, 15, 20)% Cr alloys are subsequently aged at 748 K up to 203 h and lifetime measurements were carried out at room temperature at different intervals of time. The ageing temperature of 748 K is chosen according to the results of isothermal studies in section 5.3.2 and because the temperature is within α'-phase formation region of Fe-Cr equilibrium phase diagram. With inputs from hardness, lifetime and Doppler broadening, the results are classified as three classes with respect to Cr concentration (i) Fe-(2,5)% Cr (ii) Fe-(15, 20)% Cr and (iii) Fe-(9, 9.5, 12)% Cr.

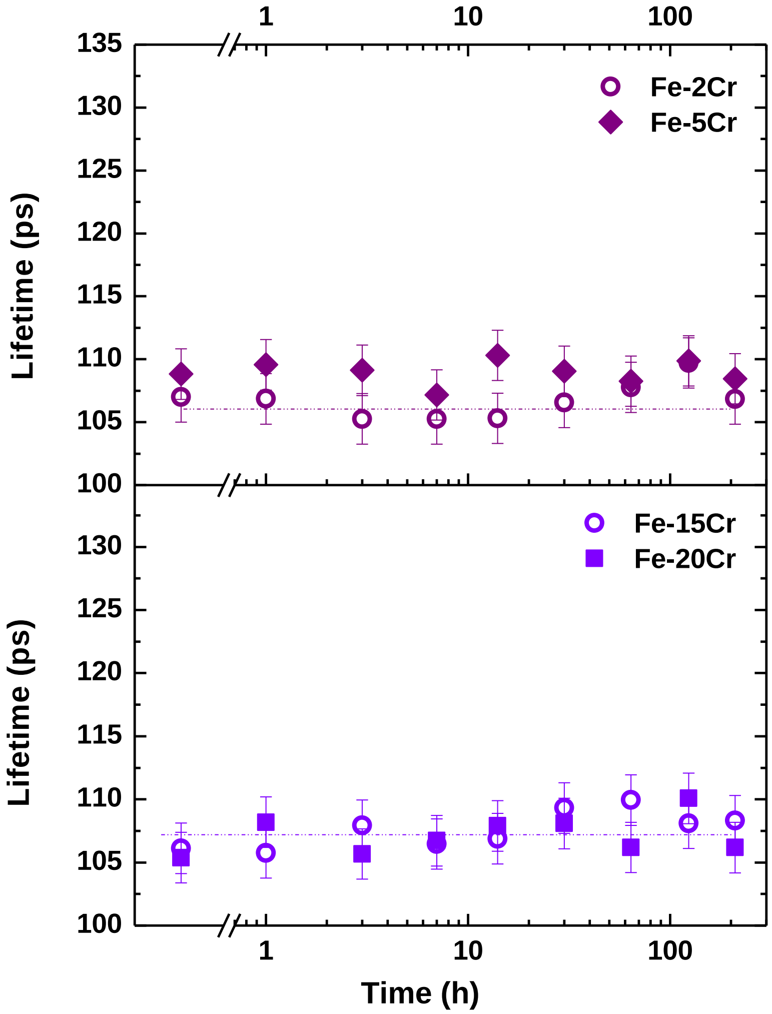

Figure-5.18: Positron lifetime in Fe-2Cr, Fe-5Cr, Fe-15Cr and Fe-20Cr alloys as a function of ageing time at 748 K. The initial state of the alloys is air-quenching from 1273 K. The dashed line shows the positron lifetime in defect-free alloy. The lifetime is same as bulk with ageing, indicating no formation of open volume defects.

Results of Fe-(2, 5)% Cr alloys and Fe-(15, 20)% Cr alloys are shown in Figure-5.18. No change in lifetime observed till 203 h in these alloys. It should be noted that the observed lifetimes are always found to be closer to defect-free bulk lifetime.

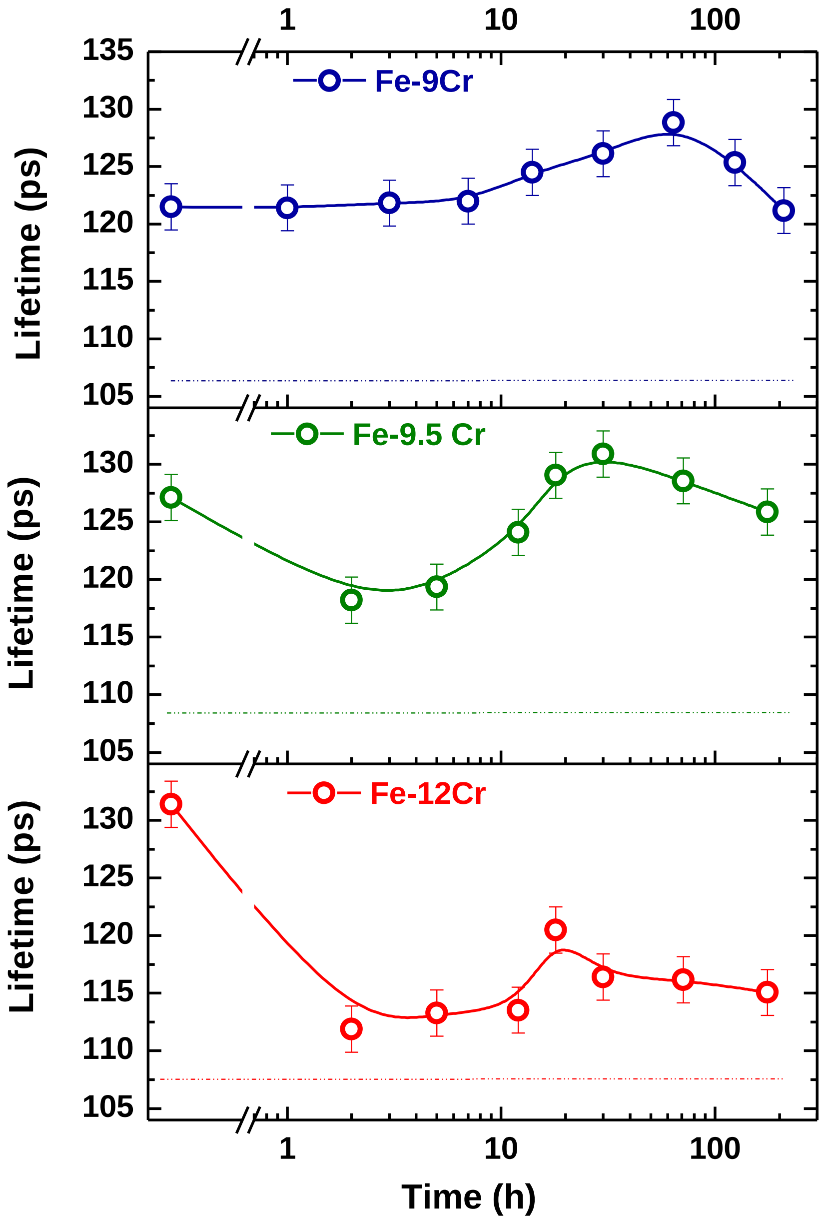

Figure-5.19: Positron lifetime in Fe-9Cr, Fe-9.5Cr and Fe-12Cr alloys as a function of ageing time, up to 210 h. Ageing carried at 748 K. The initial state of the alloys is air-quenching from FCC γ-phase. The dashed line indicates the lifetime in defect-free alloy. Precipitation stage is seen in all three alloys following dislocation annealing.

The Fe-(9, 9.5, 12)% Cr alloys (Figure-5.19) containing quenched in defects showed stages corresponding to (i) decrease in open volume defects at short ageing times (ii) fresh formation of new open volume defects after ageing times greater than 5 h, corresponding to precipitates formation and (iii) gradual, marginal reduction in lifetime for larger ageing times, probably, due to dissolution of precipitates gradually to attain equilibrium phase.

Previous literature is consistent with results of Fe-(2, 5)% Cr alloys that Cr rich α'-phase will not form for ageing times carried in this study, at least for pure ageing [21]. But, alloys with Cr concentration > 9% Cr are expected to form α'-phase during ageing. Considering that and hypothesizing α'-phase is accompanied by misfit dislocations that can trap positrons, the precipitation stage in Fe-(9, 9.5, 12)% Cr alloys can be considered as α'-phase formation. Considering this hypothesis, and the previous literature which says thermal ageing causes α'-phase formation for Fe-Cr alloys with Cr concentration above 13 % [1, 22], increase in lifetime is expected for Fe-(15, 20)% Cr alloys also. However, it is not seen in our results suggesting that the precipitates may not be α'-phase. However, it would be ambiguous at this stage to conclude that traps are not misfit dislocations of α' precipitates. The ambiguity comes from possible accelerated segregation in Fe-(9, 9.5, 12)% Cr alloys due to dislocations and no significant segregation in Fe-(15, 20)% Cr alloys for the ageing time of 203 h. However, the later results resolve the ambiguity.

Equilibrium phase diagram of Fe-Cr suggest the formation of σ-phase for high Cr concentration at temperature greater the 785 K (Figure-5.17). Hence, the alloys aged at 748 K until 203 h are subsequently aged at 873 K up to 28 h and lifetime of positron measured at different intervals. The results are shown in Figure-5.20, Figure-5.21, and Figure-5.22. The positron lifetime is found to be the same as bulk in Fe-2Cr alloy and a small deviation (increase and decrease) observed in Fe-5Cr alloys.

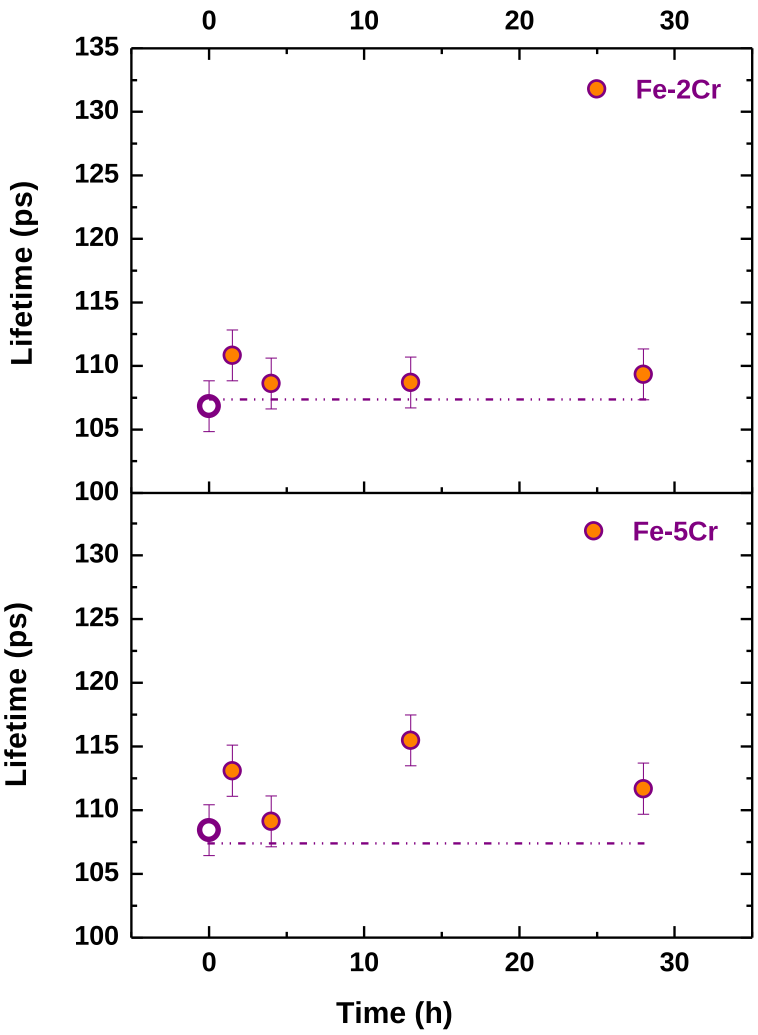

Figure-5.20: Positron lifetime in Fe-2Cr and Fe-5Cr alloy as a function of ageing time. Ageing carried at 873 K. The initial state of the alloys is air-quenching from FCC γ-loop, followed by ageing at 748 for 210 h. The dashed line indicates the positron lifetime in defect-free alloy.

Lifetime decreased with ageing time in Fe-(9, 9.5, 12)Cr alloys (Figure-5.21), indicating gradual dissolution of precipitates. It is to be noted that, in Fe-12Cr alloy, lifetime increased after first 1.5 h treatment at 873 K and then decreased with ageing time. Also, the rate of decrease of lifetime is less in Fe-12Cr alloys as compared to Fe-(9, 9.5)Cr alloys. A further treatment of these alloys at 973 K for 2 h caused lifetime to reach bilk value in

Fe-(9, 9.5)Cr. However, the lifetime is still higher than bulk value in Fe-12Cr alloy, indicating that a few precipitates retained. These observations of precipitate dissolution are consistent with recovery of much of the original toughness in irradiated high Cr steel by heat treating for 2 h at 873 K [2].

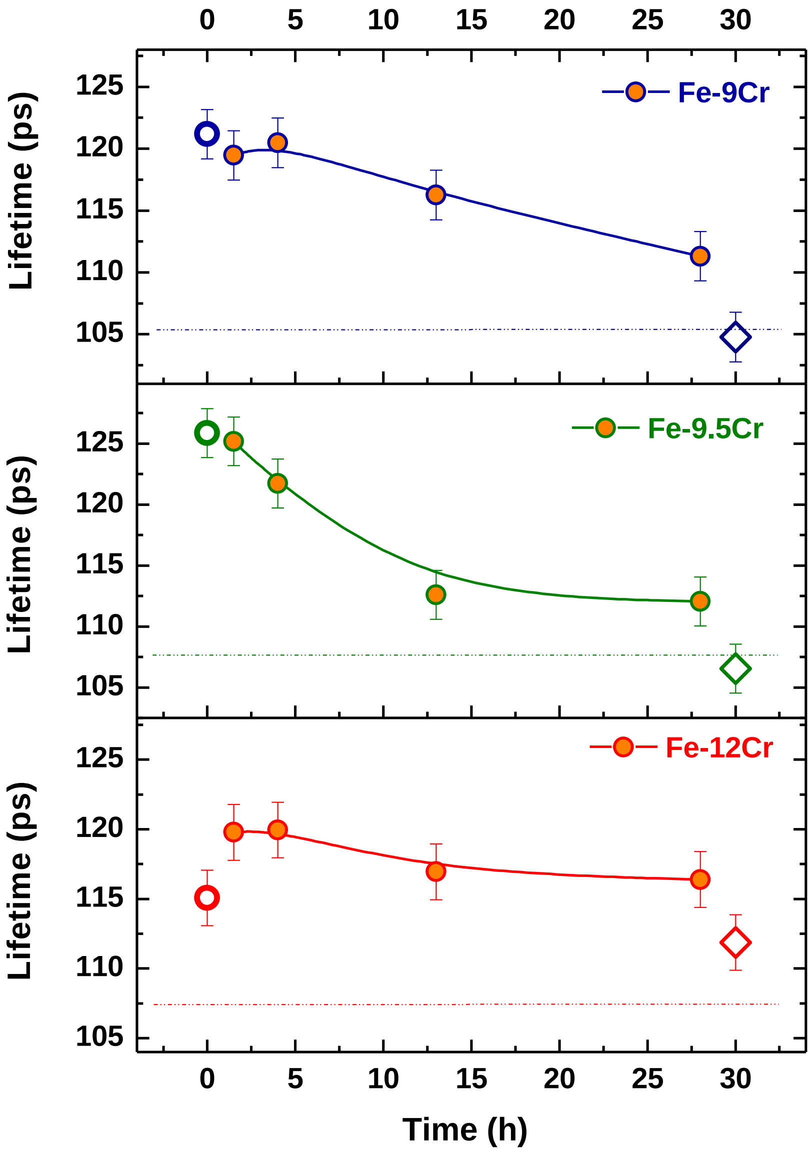

Figure-5.21: Positron lifetime in Fe-9Cr, Fe-9.5Cr and Fe-12Cr alloys as a function of ageing time at 873 K. The initial state of the alloys is air-quenching from FCC γ-loop, followed by ageing at 748 K up to 210 h and is shown as open circle symbol. The dashed line indicates the positron lifetime in defect-free alloy. Lifetime in alloys with additional treatment of 2 h at 973 K is shown as open diamond symbols.

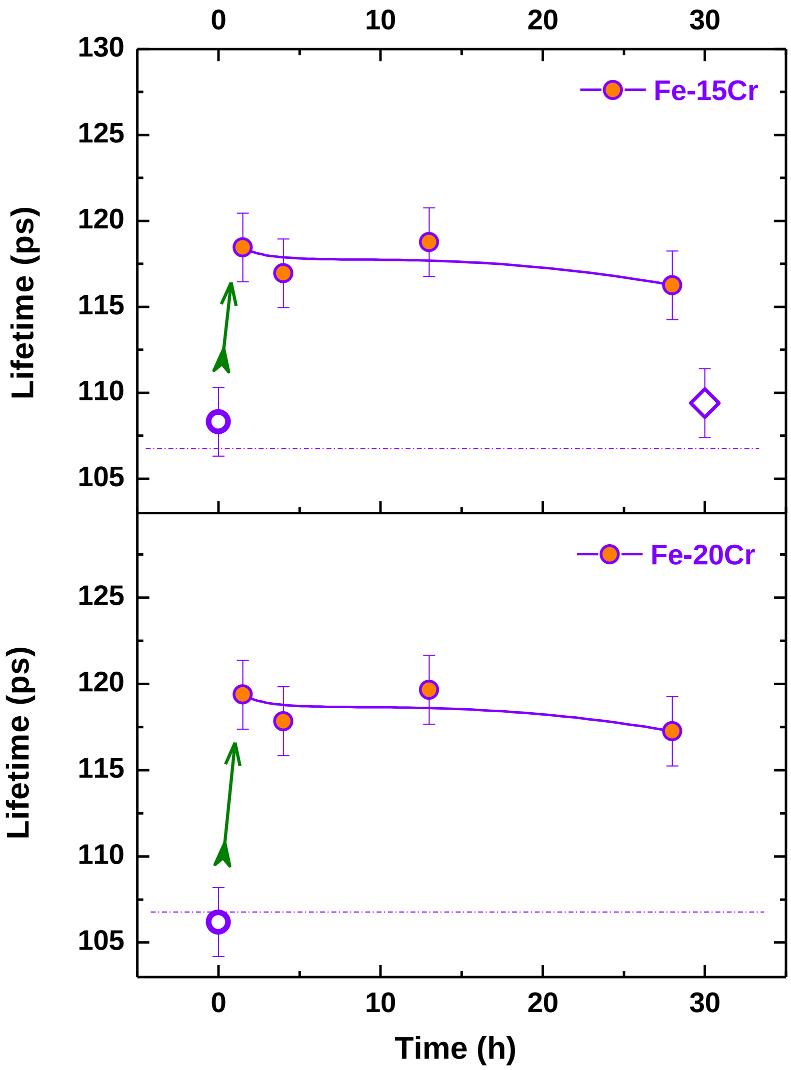

Figure-5.22: Positron lifetime in Fe-15Cr and Fe-20Cr alloy as a function of ageing time at 873 K. The initial state of the alloys is air-quenching from 1273 K, followed by ageing at 748 for 210 h. The dashed line indicates the positron lifetime in defect-free alloy. Lifetime in Fe-15Cr alloy with additional treatment of 2h at 973 K is shown as open diamond symbols.

On the other hand, interestingly, Fe-(15, 20)Cr alloys (Fugure-5.22) showed a significant increase in lifetime from bulk value with mere 1.5 h of ageing and further ageing up to 28 h caused only a small reduction in lifetime. Since, increase in the lifetime indicate formation of the open volume defects from the defect-free alloys and the Fe-Cr phase diagram [1, 23] suggests formation of the intermetallic σ-phase for temperature greater than

785 K, formation of σ-phase is believed to be the reason for increase in lifetime with precipitate-matrix interfacial defects as trapping centres.

Further, to rationalize the effect of heat treatment at 748 K, the Fe-(15, 20)Cr alloys in homogenized form (with no prior treatment at 748 K) are treated at 873 K up to 31.5 h (Figure-5.23) with positron lifetime measurements at intermediate steps.

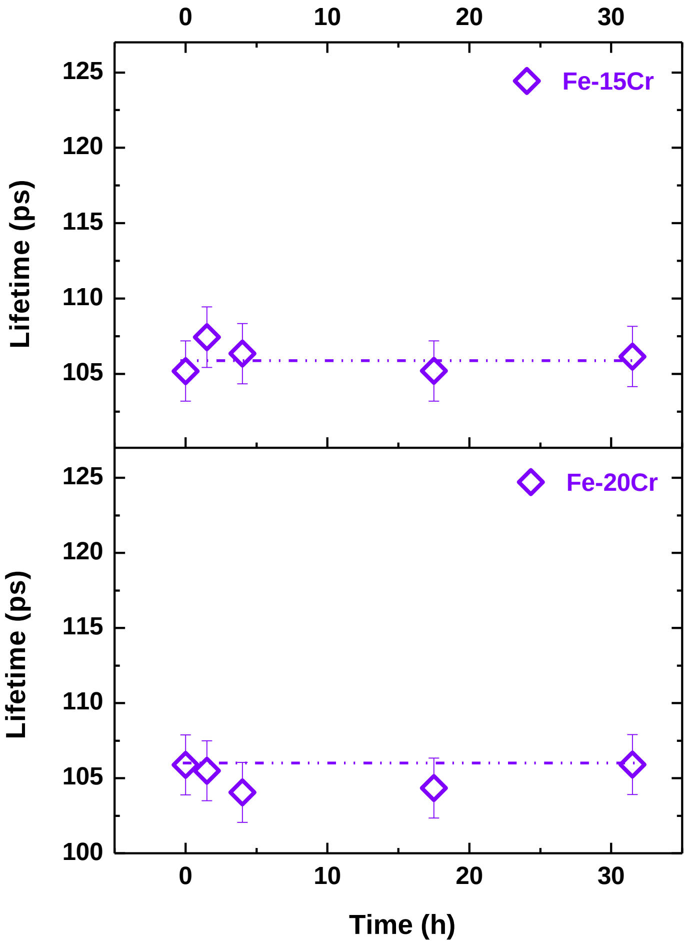

Figure-5.23: Positron lifetime in Fe-15Cr and Fe-20Cr alloy as a function of ageing time at 873 K. The initial state of the alloys is air-quenching from 1273 K. The dashed line indicates the positron lifetime in defect-free alloy.

The results show that the lifetime remains same as bulk lifetime indicating no precipitation. These observation shows that treatment at 748 K induced Cr segregation. These combined results suggest the following mechanism. The low temperature heat treatment caused segregation of Cr by bulk diffusion process i.e. formation of α'-phase. During the treatment at 873 K, the Cr rich α'-phase convert into intermetallic σ-phase. This mechanism will also explain the increase in lifetime Fe-(9, 9.5, 12)Cr alloys though they are treated at only 748 K. The extra energy for the formation of σ-phase will be provided by the defect sinks which will be having excess Gibbs free energy.

The crystal structure of both Fe and Cr is BCC and the lattice parameters are 2.8665 Å and 2.91 Å, respectively. The lattice parameter of BCC phase of Fe-Cr alloys is between the two values. This shows that α'-phase form coherently with matrix without any interfacial defects. However, crystal structure of σ-phase is tetragonal, indicating that it will be incoherent with matrix at interfaces, leading to defect formation. It is believed that these defects are responsible for higher lifetime observed over phase transition from α' to σ in Fe-(15, 20)Cr alloys after 873 K heat treatment.

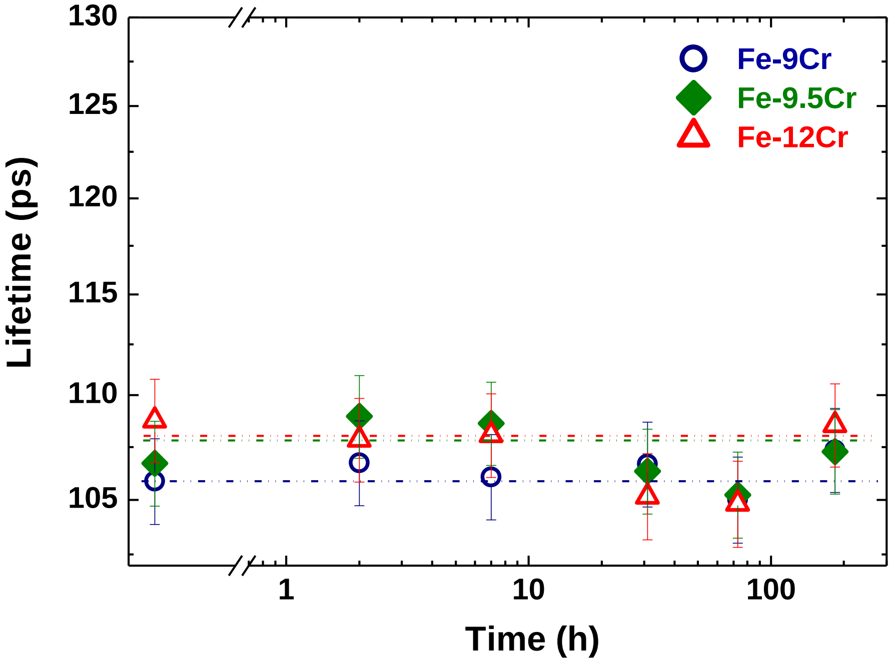

Figure-5.24: Positron lifetime in Fe-9Cr, Fe-9.5Cr and Fe-12Cr alloy as a function of ageing time at 748 K. The initial state of the alloys is homogenization at 1073 K (BCC α-phase). The dashed line indicates the positron lifetime in defect-free alloy.

To find out the similar Cr segregation in Fe-(9, 9.5, 12)Cr alloys at 748 K, the corresponding alloys are homogenized in defect-free coarse grained form and aged at 748 K up to 184 h with lifetime measured at different intervals. The lifetime showed no changes (Figure-5.24) indicating that no open volume defects formed. Subsequent ageing at 873 K for 1.5 h did not result in increase in lifetime, indicating that Cr segregation is not significant in the absence of dislocations. These results suggest that the Cr precipitates observed in ageing after quenching (from FCC) are resultant of segregation accelerated by quenched in defects.

5.4 SUMMARY

Positron lifetime studies carried on Fe-Cr alloys to find out the effects of non-equilibrium conditions, in particular dislocations, on Cr segregation. The following observations are made.

- Signatures of Cr segregation observed in isochronally heat treated Fe-9Cr and Fe-12Cr alloys following annealing of quenched-in defects. Fine precipitates are observed in TEM micrographs of Fe-9Cr alloy heat treated at 900 K and they are found to be Cr rich from EDS study. Annealing of quenched-in dislocations also evidenced from the variation in dislocation densities from the micrographs of as-quenched and 773 K treated alloys. The precipitation signatures are not observed in isochronal studies of Fe-9Cr alloys with homogenization as initial condition, which consists of dislocation-free coarse equiaxed grains.
- These results are substantiated by finding more accurate temperature ranges of precipitation using isothermal studies. It is found that precipitation occurs at temperatures as low as 723 K. The precipitation is found to be unstable above 873 K, even for ageing time of 5 h. It is also observed that quenched condition is more effective in inducing the precipitate formation as compared to deformed condition.

- Quenched-in Fe-Cr alloys with Cr concentration ranging from 2-20% showed that alloys with concentration around 10% resulted in non-equilibrium, hard martensitic structure with associated defects. These non-equilibrium conditions are found to be effective in acceleration of Cr segregation.
- Studies on Fe-15Cr and Fe-20Cr alloys showed that Cr segregate as α'-precipitates during ageing at 748 K and that will not result in the increase in lifetime. However, during subsequent treatment at 873 K, the α'-phase converted into intermetallic σ-phase. These σ-precipitates being incoherent with the matrix, an increase in lifetime is observed due to interfacial open volume defects.
- By analogy and observation of SAD pattern from Fe-9Cr alloys (Figure-5.5(d)), it is believed that the precipitates formed in Fe-(9, 9.5, 12)Cr alloys are intermetallic σ-precipitates.

5.6 REFERENCES

---

[1] L. Malerba , A. Caro, J. Wallenius, J. Nucl. Mater. **382**, 112 (2008).

[2] T. Angeliu, E. L. Hall, M. Larsen, A. Linsebigler, C. Mukira, Metall. Mater. Trans. A **34A**, 927 (2003).

[3] P. Hautojarvi, J. Johansson, A. Vehanen, J. Yli-Kauppila, P. Moser, Phys. Rev. Let. **44**, 1326 (1980).

[4] S. Hari Babu, K. V. Rajkumar, S. Hussain, G. Amarendra, C. S. Sundar, T. Jayakumar, J. Nucl. Mater. **432**, 266 (2012).

[5] J. V. Bee, R. W. K. Honeycombe, Metall. Trans. A **9A**, 587 (1978).

[6] J. Kansy, Nucl. Instrum. Meth A **374**, 235 (1996).

[7] L. petrov, T. Troev, N. Nankov, E. Popov, J. Phys. Conf. Series **207**, 012037 (2010).

[8] Y. Kamimura, T. Tsutsumi, E. Kuramoto, Phys. Rev. B **52**, 879 (1995).

---

[9] K. Sato, T. Yoshiie, T. Ishizaki, Q. Xu, Phys. Rev. B **75**, 094109 (2007).

[10] S. Hari Babu, R. Rajaraman, G. Amarendra, R. Govindaraj, N. P. Lalla, Arup Dasgupta, Gopal Bhalerao, C. S. Sundar, Philos. Mag. **92**, 2848 (2012).

[11] K. Sato, T. Yoshiie, T. Ishizaki, Q. Xu, Phys. Rev. B **75**, 094109 (2007).

[12] R. Krause-Rehberg, W. Anwand, G. Brauer, M. Butterling, T. Cowan, A. Hartmann, M. Jungmann, A. Krille, R. Schwengner, A. Wagner, Phys. Status Solidi C **6**, 2451 (2009).

[13] M. Matijasevic, A. Almazouzi, J. Nucl. Mater. **377**, 147 (2008).

[14] K. –G. Tak, U. Schulz, G. Eggeler, Mat. Sci. Eng. A **510-511**, 121 (2009).

[15] T. Torsti, M. Heiskanen, M.J. Puska, R.M. Nieminen, Int. J. Quantum Chem. **91**, 171 (2003). Available at http:www.fyslab.hut.fiepmpositronmikadoppler.html.

[16] M.J. Puska, P. Lanki, R.M. Nieminen, J. Phys.: Condens. Matter **1** 6081 (1989).

[17] S.M. Dubiel and J. Cieslak, arXiv:1105.2179v1 [cond-mat.mtrl-sci] (2011).

[18] F. Abe, Sci. Technol. Adv. Mater. **9**, 013002 (2008).

[19] B. Mintz, E. M. Maina, W. b. Morrison, Mater. Sci. Technol. **24**, 177 (2008).

[20] W. Kesternich, Phil. Mag. **52**, 533 (1985).

[21] Wei Xiong, Malin Selleby, Qing Chen, Joakim Odqvist, Yong Du, Crit. Rev. Solid. State **35**, 125 (2010).

[22] V. V. Sagaradze, I. I. Kositsyna, V. L. Arbuzov, V. A. Shabashov, Yu. I. Filippov, Phys. Met. Metall. **92**, 89 (2001).

[23] H. Okamoto, Cr-Fe, in ASM Handbook: Volume 3: Alloy Phase Diagrams, H. Baker, Ed. ASM International: Materials Park, OH. 1991.

Chapter - 6

Summary and Future Scope

6.0 PREAMBLE

This chapter highlights the important conclusions drawn from this study on ferritic/martensitic steel and Fe-Cr model alloys. A few suggestions for future work are mentioned.

6.1 SUMMARY

Positron annihilation spectroscopy studies have been carried out on two ferritic/martensitic steels i.e. EUROFER97 and modified 9Cr-1Mo, to investigate the correlation between the microstructure and positron annihilation characteristics. Studies on the dependence of non-equilibrium conditions for the formation of Cr precipitates in Fe-Cr binary alloys are carried out. The results are substantiated with other corroborative techniques such as electron microscopy, hardness and ultrasonic velocity.

6.1.1 Ferritic Steels

Positron annihilation studies (PAS) on normalized EUROFER97 and modified 9Cr-1Mo steel samples indicate distinct microstructural changes corresponding to annealing of quenched-in defects, nucleation, growth and coarsening of precipitates between 300 K - 1073 K and martensitic phase formation above lower critical temperature (Ac_1).

By comparing the lifetime studies of deformed pure iron and ferritic steels with the microstructural changes as seen in transmission electron microscopy (TEM) and secondary electron microscopy (SEM) micrographs, the quenched-in defects which anneal at lower temperatures are identified as dislocations. PAS turned out to be an unique technique to identify this annealing stage because, electron microscopy, ultrasonic velocity, XRD and hardness techniques are found to be insensitive to probe this stage.

Using the quantified precipitate size and the number density from the TEM studies, the volume fraction and the precipitate-matrix interfacial surface area are deduced and compared with positron lifetime results in the case of EUROFER97 steel. The comparison suggests that the open volume defects responsible for higher lifetime during the precipitation stage are associated with the precipitates. By hypothesizing that vacancy defects will not be present inside precipitates, the observation from the coincidence Doppler broadening spectra and lifetime studies of post-normalization deformed EUROFER97 samples suggest that the trapping sites are precipitate-matrix interfaces.

Electron microscopy studies of both EUROFER97 and modified 9Cr-1Mo steels showed the nucleation, growth and coarsening stages of precipitation. Comparison of isochronal positron lifetime results of plain 9Cr-1Mo and modified 9Cr-1Mo steel indicates that the $M_{23}C_6$ precipitates are predominantly responsible for the trapping of the positrons.

In normalized and tempered modified 9Cr-1Mo steel, PAS has exhibited clear signatures of fine secondary precipitates as compared to other techniques.

Correlation between positron lifetime, ultrasonic velocity and hardness of modified 9Cr-1Mo steel showed that the set of three parameters is an unique combination for distinguishing distinct microstructural changes in ferritic steels.

6.1.2 Fe-Cr alloys

Signatures of Cr segregation are observed in the isochronal studies of quenched Fe-9Cr and Fe-12Cr alloys, following annealing of quenched-in defects. TEM studies on Fe-9Cr alloy confirmed annealing of dislocations below 773 K, precipitates at 900 K and dissolution of precipitates above 973 K. The Cr rich nature of precipitates is found from EDS study. In the absence of prior dislocations, precipitation stage is not observed in Fe-9Cr alloy, which is an interesting observation.

Isothermal studies indicate that the precipitation occurs at temperatures as low as 723 K. The precipitates are found to be unstable at 873 K and above. Quenched condition is found to be more effective in precipitate formation as compared to deformed condition.

Studies on quenched Fe-Cr alloys with Cr concentration ranging between 2-20% Cr showed that the alloys with concentration around 10% result in martensitic structure. Hence, they showed accelerated Cr segregation. Studies on Fe-15 Cr and Fe-20 Cr alloys showed that the Cr segregate as α' during ageing at 748 K. Since the lattice structure is similar with small difference in lattice parameter, these precipitates do not trap positrons and hence, no variation in lifetime. However, during subsequent treatment at higher temperature (873 K) the α' converts into intermetallic σ-phase, which is tetragonal in structure. From these observations and selected are diffraction studies on Fe-9.5Cr alloy, it is ascertained that the precipitates formed in Fe-(9, 9.5, 12)Cr alloys are also intermetallic σ-precipitates.

6.2 FUTURE SCOPE

Isothermal studies using PAS on normalized and tempered ferritic/martensitic steels at temperature close to the operating temperatures can generate data that can be used for practical applications. This study on modified 9Cr-1Mo steel would be more appropriate, as it is chosen as steam generator structure material in some of the recent nuclear reactors [1]. For example, modified 9Cr-1Mo steel had been chosen for steam generator of prototype fast breeder reactor (PFBR), Kalpakkam [2].

Further, isothermal studies on normalized ferritic steels at temperatures close to the range of tempering temperature will give kinetics of precipitate evolution. Having known that precipitates such as M_2X, $M_{23}C_6$ and MX evolve at different temperatures, the isothermal studies could access the relative contribution to positron lifetime. This information can be used to study precipitate evolution in newly designed ferritic steels.

Detailed transmission electron microscopy, atom probe tomography and Mossbauer spectroscopy can be carried out to quantify Cr segregation in Fe-Cr binary alloys. Mechanical properties such as hardness can be studied with varying precipitate density and size to understand their effect on ductility.

6.3 REFERENCES

---

[1] R. L. Klueh, ORNL/TM-2004/176.

[2] S. L Manan, S.C. Chetal, B. Raj, S.B. Bhoje, Trans. Ind. Inst. Metals **56**, 155 (2003).

Appendix

Doppler Broadening Based Positron NDT

A.0 PREAMBLE

A Doppler broadening based positron annihilation technique for Non-Destructive Evaluation (NDE) applications is attempted. It uses a special geometry of source-sample-detector to preferentially suppress the background to get large change in S-parameter for a given change in defect characteristics in the test sample. Preliminary observations of the effectiveness of geometry are presented here, in comparison with conventional method. A methodology to understand the signal-to-background ratio improvement is presented.

A.1 INTRODUCTION

The working life of practical alloys is usually restricted to smaller than the predicted lifetime for avoiding failure during usage. A number of non-destructive evaluation (NDE) techniques such as ultrasonic velocity, eddy currents, Magnetic Barkhausen noise and X-ray diffraction works well after significant changes take place in the material properties such as moduli, electrical resistivity, magnetization and lattice parameter. However, these property changes are resultant of the significant changes in the atomistic defects such as the point defects and the line defects. The above mentioned techniques are insensitive to early stages of the atomistic defect productions and accumulation, which covers large fraction of working lifetime before material failure [1, 2]. Hence, probing the minor changes of material properties is of great interest for the optimum utilization of working lifetime of structural materials.

Positron annihilation spectroscopy (PAS), being sensitive to atomistic defects, has promising potential. It was a dream for the last three decades to develop positron NDE techniques for a broad range of applications. A detailed review of Coleman [2] brought out the advantages and limitations of PAS techniques in the NDE and different applications, where it can contribute significantly. The production of dislocations and vacancies during the deformation allow PAS to probe degree of deformation during tensile and compressive stresses [3, 4, 5]. Fatigue is one of the highly demanding applications for the positron NDE and hence, extensively reported [3 5, 6, 7, 8, 9, 10, 11]. Hydrogen embrittlement is another area where PAS can serve as a NDE technique. Hydrogen content and its accumulation affect the defect production in steels and hence, the positron annihilation parameters can get altered [12]. Radiation damage, voids and bubble growth is yet another area of application where positron annihilation could significantly contribute [13, 14, 15, 16, 17].

Positron annihilation technique is a non-destructive technique in the sense that the sample is not modified in any means. However, there exist limitations on the sample dimensions that can be probed and further, the spectrometer is generally laboratory based. Earlier, a number of developments is reported towards NDE positron systems, based on both lifetime [7, 18, 19] and Doppler broadening [3, 20]. In this work, positron annihilation technique is defined as NDE technique if it satisfies three conditions. (i) It should be possible to probe annihilation characteristics of single sample, (ii) Possibility to carry out measurements in relatively short duration of time, (iii) A fewer geometrical constraints for the measurements.

Doppler broadening based system is chosen because it has a fewer geometrical constraints and relatively short test duration. Earlier, AEA Harwell had developed a Doppler broadening based NDE system [20], where the source was encapsulated in an aluminium holder and the sample can be moved in front of the source by a XY slider. This system was reported to have a spatial resolution of 1 mm^2. Due to source holder geometry mentioned, there will be a constant contribution from the annihilations inside aluminium, which will be about 50% of the total annihilation counts detected. Hence, this geometry had a poor signal-to-background ratio of less than or equal to 1.

A.2 DETAILS OF THE NDE SYSTEM

In the present work, a Doppler broadening based NDE positron system designed with a special geometry of source-sample-detector to reduce the constant background to improve the variation in S-parameter. The basic idea is to preferentially suppress the background counts, which are generated due to annihilations at source holder and surrounding materials other than the sample. Hence, the detector detects annihilation counts from the sample whose fraction is considerably larger than the background. However, to test the successful implementation of the idea, the lateral resolution is compromised significantly in this case. The schematic diagram of the system and the details of source holder geometry are shown in Figure-A.1 and Figure-A.2, respectively. Photograph of the setup is shown in Figure-A.3.

A 10 % efficiency HPGe planar detector (M/S Baltic Scientific Instruments) with a compact digital multi-channel-analyzer, MCA 527, including high voltage power supply and a set of Li-accumulators is used for the detection of gamma rays and spectroscopic amplification of the signals. The distance between the source and the sample is maintained at a distance of 10 mm using a specially designed source holder such that the illumination of positrons is limited to a circle of diameter 20 mm at the sample. The distance between the source-sample assembly is maintained at a distance of 200 mm from the detector. The detector resolution is 1.24 keV at 661 keV (Cs-137) with a 2 % dead time. For a 6 % dead time, the resolution deteriorates to 1.27 keV.

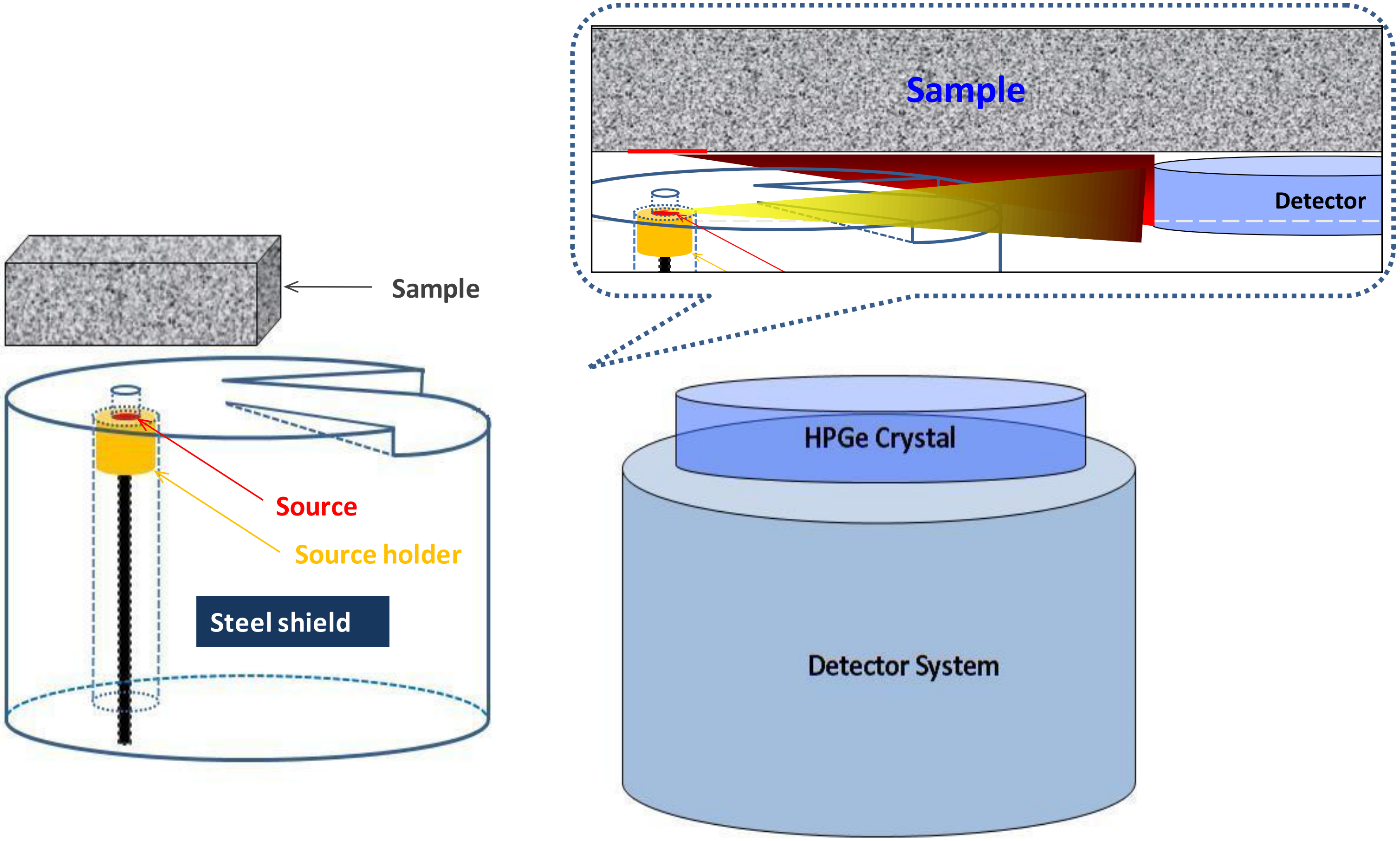

Figure-A.1: Schematic picture of source-sample-detector geometry. The front face of the stainless steel shield is maintained parallel to the surface of HPGe crystal of a planar detector. Sample position is about 10 mm from the source. Presented in the inset, the simplified schematic where, only the solid angle of gamma rays that reach the detector crystal is shown. The annihilated gamma rays from the sample will have direct line-of-sight while the annihilated gamma rays from source holder and 1274 keV gamma rays from source will be attenuated in the shield and hence, reducing their contribution.

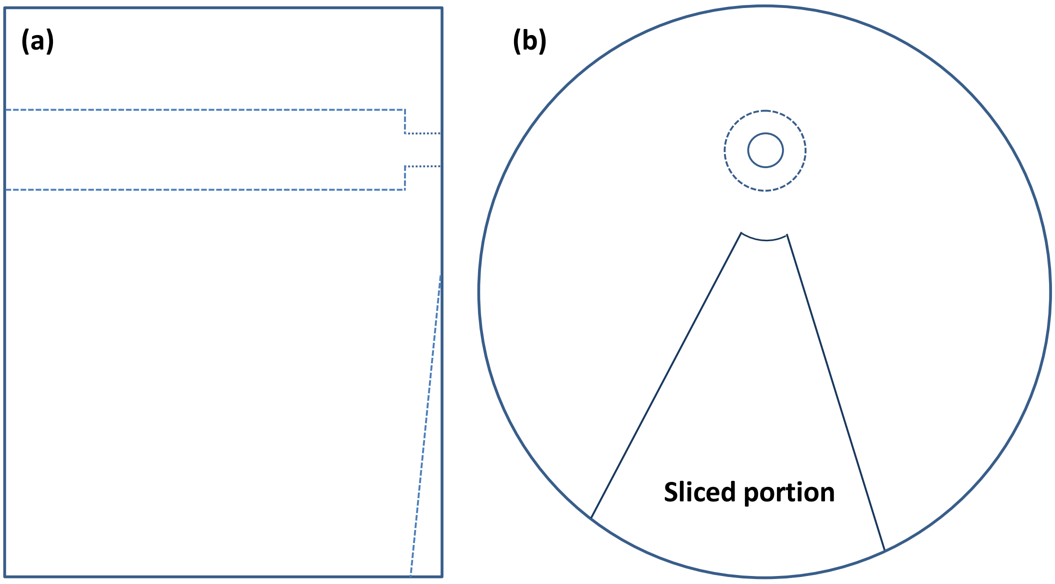

Figure-A.2: (a) Cross sectional view and (b) top view of the stainless steel shield. The sliced portion is intended to make line-of-sight for the annihilated gamma rays from sample to active area of the detector.

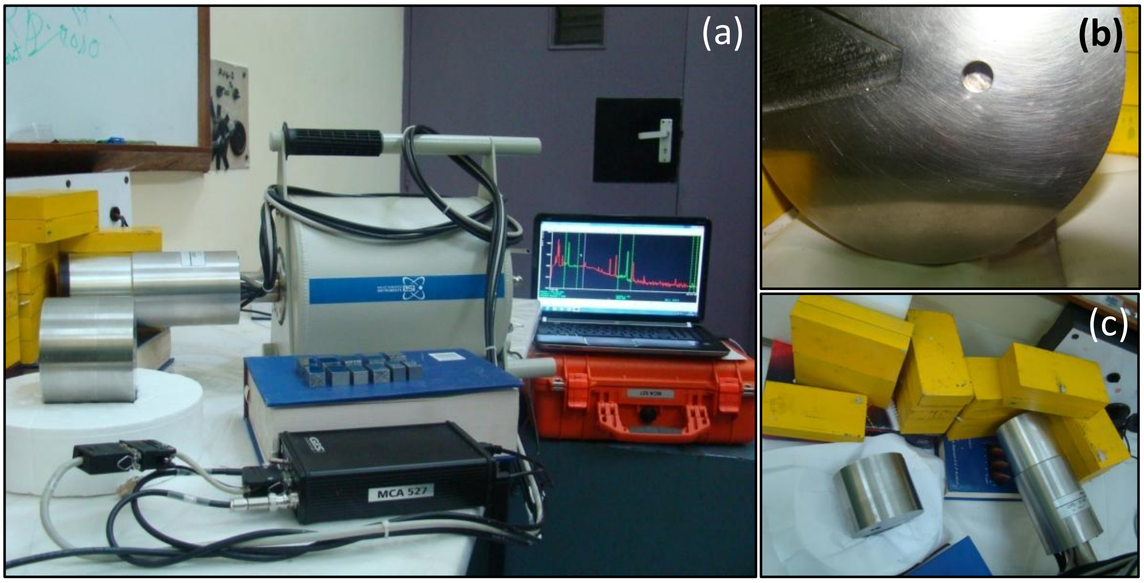

Figure-A.3: (a) Photograph of the Doppler broadening based NDE system. (b) Source inside the shield. (c) The source-shield and detector arranged in designed geometry.

The measurements are carried with a dead time around 6% to carry out shorter measurements. The extent of error between the measurements on the same sample under identical test conditions is investigated. A total count of 4 x 10^5 is accumulated between 511 ± 10 keV, for each spectrum.

A.3 RESULTS

In the present work, attaining a signal-to-background ratio of more than 1 is important. This is brought out by comparing the new setup with conventional sandwich mode. The differences between the two spectra resulted from a given differences in annihilation characteristics.

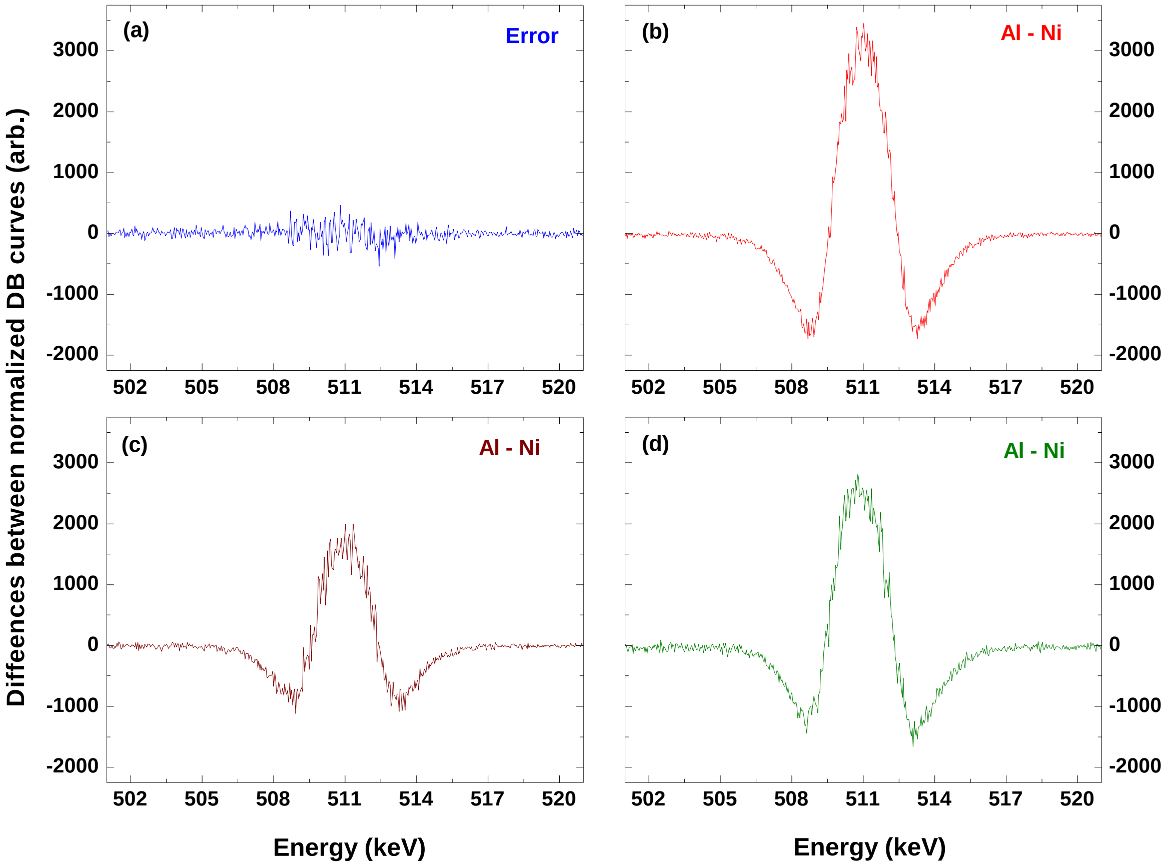

Figure-A.4: (a) Error obtained between two repeat measurements carried out on the same sample under identical test conditions, shown for reliability of results. Differences in distribution of weighted counts between annealed Al and annealed Ni samples measured using (b) conventional way with two identical test samples (c) conventional way with one test sample and one Mo sample in sandwich mode (the variation at peak is observed to be half of the previous mode (b)) and (d) designed NDE mode (the variation at peak is seen significantly better than in (c)).

The difference in weighted counts between Doppler broadening spectra of annealed Al and annealed Ni, $N_{Al}(E) – N_{Ni}(E)$, is shown in Figure-A.4 with three modes i.e. (i) Conventional sandwich mode, measured with two identical test samples. (ii) Conventional sandwich mode, but, with one test sample and a Mo sample in sandwich. Hence, the signal from actual sample will be around 0.5 fraction, with rest of the counts from Mo, which is a constant contribution in both the measurements. This is equivalent of system developed by AEA Harwell. (iii) NDE mode developed with the special geometry measurable with a single sample. As it can be observed, the NDE mode has resulted in bringing out the better variations than in the case of single sample sandwiched with a reference Mo sample. It should also be noted that by measuring the peak counts in conventional two test sample mode and measuring source contribution from lifetime measurement, one can quantify the signal fraction. By multiplying peak counts with signal fraction and comparing it with the normalized peak counts of other modes, the signal-to-background from of other modes can be quantified.

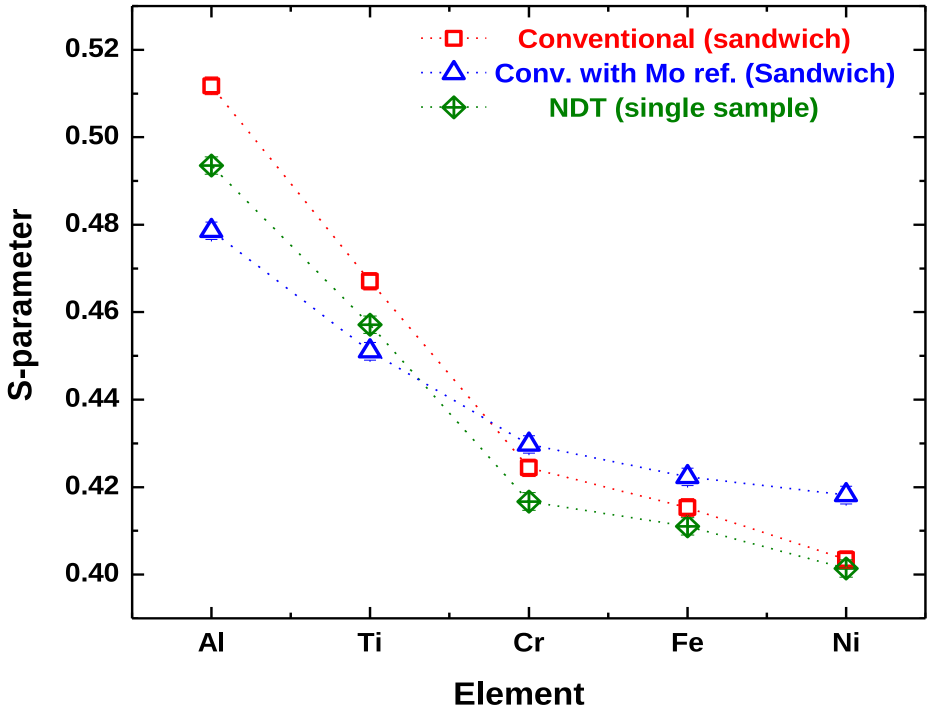

Figure-A.5: S-parameter measured in annealed pure (99.99) elements in three modes. The NDE mode is found to reproduce the results of conventional measurements. The NDE mode is found to show variation better than conventional mode with a single test sample with Mo reference.

The S-parameter variation between a few annealed pure metals in all the three modes mentioned above is presented in Figure-A.5. The dimensions of the samples are 25 x 25 x 1 mm^3. As it should be expected the best method is one which shows the optimum variation. Eventually, the conventional method with two identical test samples is superior as the difference between S-parameter of aluminium and S-parameter of nickel is larger (S_{Al} - S_{Ni} = 0.108) compared to other two modes. However, it should be noted that the new NDE mode showed larger variations (S_{Al} - S_{Ni} = 0.092) than the conventional mode with a single test sample and a Mo sample in sandwich (S_{Al} - S_{Ni} = 0.060).

Similar variation in S-parameter of cold-worked pure metals is seen in figure-A.6. This also showed NDE mode is superior after conventional two test sample mode.

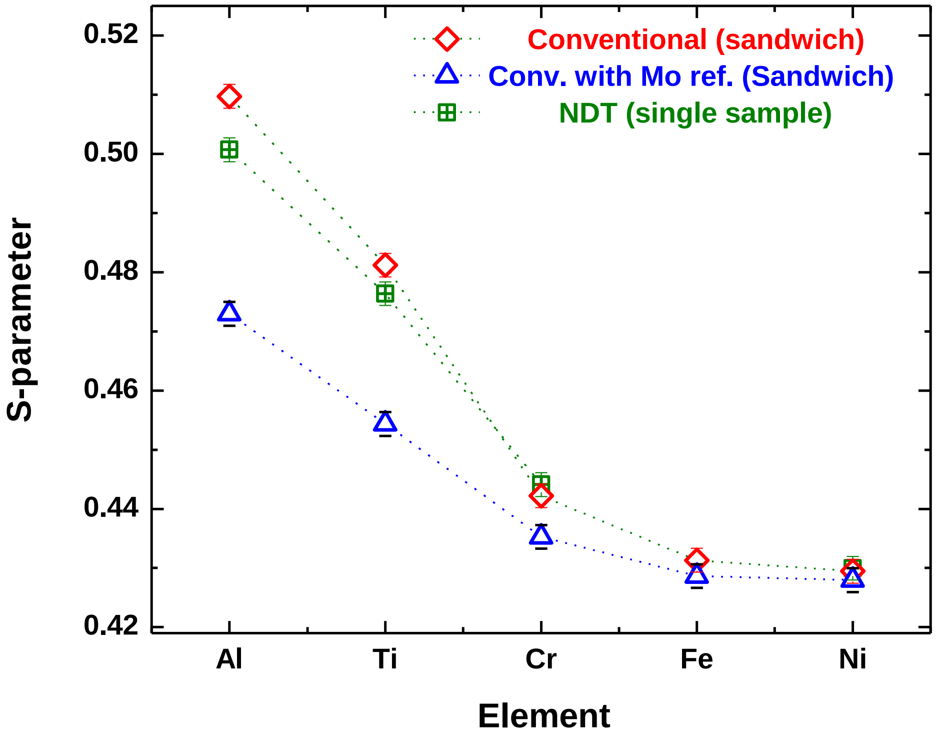

Figure-A.6: S-parameter measured in 20% cold-worked pure elements in three modes.

Figure-A.7 shows the variations in S-parameter, measured using NDE system, between annealed and cold-worked sample for the corresponding pure elements.

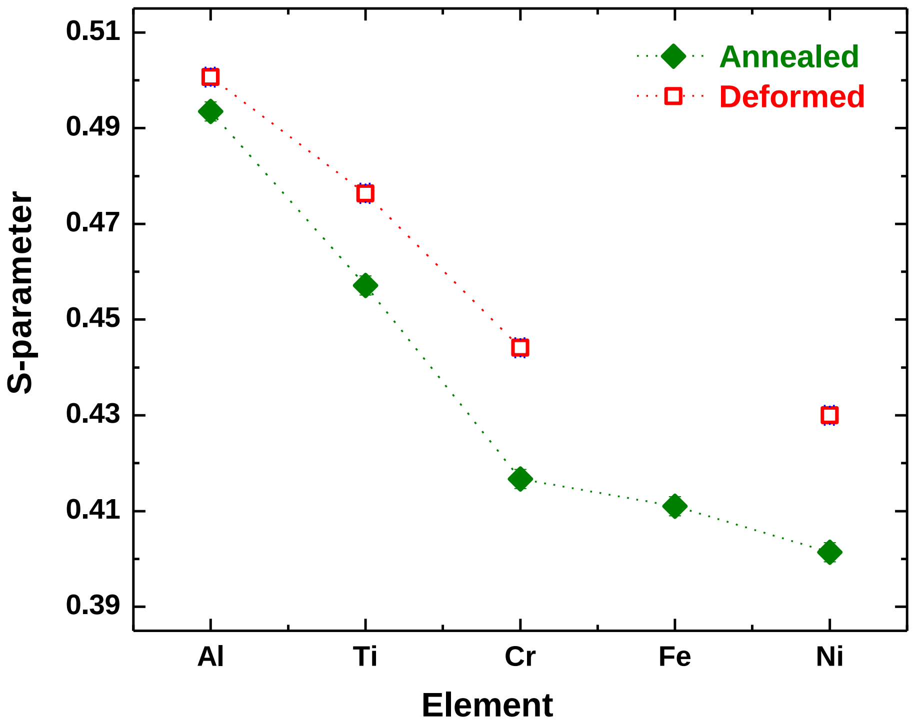

Figure-A.7: Comparison of S-parameter measured with NDE mode in annealed pure elements before and after deformation.

Figure-A.8 shows the reproducibility of NDE system. The S-parameter of annealed pure metals were measured with repeated measurements.

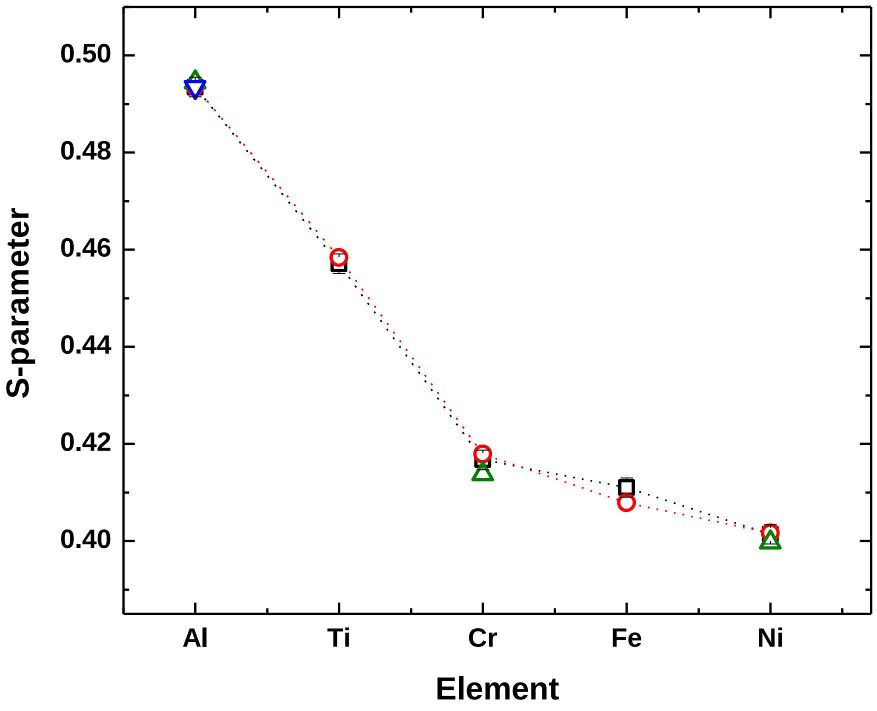

Figure-A.8: Reproducibility of S-parameter tested with repeat measurements on annealed pure elements using NDE mode. Upto four repeat measurements were carried out.

For all the data shown in Figure-A.5 to Figure-A.8, the error bars are within the data points. The error bars have a value of 0.002.

A.4 SUMMARY

- A Doppler based NDE system is developed and preliminary tests were carried out. The S-parameter variations in different pure elements are reproduced using NDE system.
- It is found that the NDE system is better in bringing out the changes in S-parameter as compared to single test sample and Mo sandwiched mode.
- The reproducibility of NDE system is checked and is satisfactory.
- It is shown that by comparing the weighted differences in virgin Doppler broadening spectra between two samples, the relatively better mode of detection can be identified. This can also quantify the signal to background ratio.
- Further work is required to use it for practical application.

A.5 REFERENCES

---

[1] C. F. Coleman, NDT Int. **10**, 227 (1977).

[2] C. F. Coleman, NDT Int. **10**, 235 (1977).

[3] M. Uchida, K. Yoshida, Y. G. Nakagawa, A. J. Allen, A. D. Whapham, Nondestr. Test. Eval. **7**, 83 (1992).

[4] B. Somieski, R. Krause-Rehberg, Fract. Engng. Mater. Struct. **24**, 267 (2001).

[5] F. A. Selim, D. P. Wells, J. F. Harmon, J. Williams, J. Appl. Phys. **97**, 113540 (2005).

---

[6] T.L. Grobstein, S. Sivashankaran, G. Welsch, N. Panigrahi, J.D. McGervey, J.W. Blue, Mater. Sci. Eng. **I38**, 191 (1991).

[7] Andrea Barbieri, Sabine Hansen-Ilzhöfer, Achim Ilzhöfer, Uwe Holzwarth, Appl. Phys. Lett. **77**, 1911 (2000).

[8] Uwe Holzwarth, Petra Schaaff, Phys. Rev. B **69**, 094110 (2004).

[9] R. S. Yu, M. Maekawa, Y. Miwa, T. Hirade, A. Nishimura, A. Kawasuso, Phys. Stat. Sol. C **4**, 3577 (2007).

[10] Uwe Holzwarth, Petra Schaaff, J. Mater. Sci. **42**, 5620 (2007).

[11] P. Eich, M.Haaks, R. Sindelar, K. Maier, Phys. Stat. Sol. C **4**, 3465 (2007).

[12] J. G. Byrne, P. Alexopoulos, F. Alex, T. D. Hadnagy, R. Waki, G. R. Miller, R.W. Ure. 4th ICPA, Helsingor, 1976, Paper E12.

[13] C. L. Snead, A. N. Goland, J. H. Kusmiss, H.C. Huang, R. Meade, Phys. Rev. B **3**, 464 (1971).

[14] G. Amarendra, B. Viswanathan, A. Bharathi, K.P. Gopinathan, Phys. Rev. B **45**, 10231 (1992).

[15] G. Amarendra, B. Viswanathan, R. Rajaraman, S. Srinivasan, K.P. Gopinathan, Phil. Mag. Lett. **65**, 77 (1992).

[16] R. Rajaraman, G. Amarendra, B. Viswanathan, K.P. Gopinathan, Phil. Mag. Lett. **68**, 257 (1993).

[17] R. Rajaraman, G. Amarendra, B. Viswanathan, C. S. Sundar, K.P. Gopinathan, J. Nucl. Mater. **231**, 55 (1996).

[18] B. Somieski, R. Krause-Rehberg, H. Salz, N. Meyendorf, J. Phys. IV, **5**, C1-127, 1995.

[19] S. Hansen, U. Holzwarth, M. Tongbhoyai, T. Wider, K. Maier, Appl. Phys. A **65**, 47 (1997).

[20] M. T. hutchings, D. J. Buttle, R. Colbrook, W. Dalzell, C.B. Scruby, J. Phys. IV, **5**, C1-111, 1995.

Publications

Included in Thesis

1 **Positron annihilation studies on 9Cr reduced activation ferritic - martensitic steels.**
*V. Ragunanthan, **S. Hari Babu**, Varghese Anto Chirayath, R. Rajaraman, G. Amarendra, S. Saroja, C. S. Sundar, Ana Alamo, Baldev Raj. Phys. Status Solidi C **6**, 2307 (2009).*

2. **Positron Annihilation Studies in Search of Fine Precipitates in Fe-9Cr alloys.**
***S. Hari Babu**, R. Rajaraman, R. Govindaraj, G. Amarendra, C.S. Sundar. AIP Conf. Proc. **1349**, 1275 (2011).*

3. **Dislocation Driven Chromium Precipitation in Fe-9Cr Binary Alloy: A Positron Lifetime Study.**
***S. Hari Babu**, R. Rajaraman, G. Amarendra, R. Govindaraj, N. P. Lalla, Arup Dasgupta, Gopal Bhalerao, C.S. Sundar, Philos. Mag. **92**, 2848 (2012).*

4. **Characterizing Microstructural Changes in Ferritic Steels by Positron Annihilation Spectroscopy: Studies on Modified 9Cr-1Mo steel.**
***S. Hari Babu,** K. V. Rajkumar, S. Hussain, G. Amarendra, C. S. Sundar, T. Jayakumar. J. Nucl. Mater. **432**, 266 (2012).*

5. **Microstructural Characterization of Ferritic/Martensitic Steels by Positron Annihilation Spectroscopy.**
***S. Hari Babu,** G. Amarendra, R. Rajaraman, C.S. Sundar, IOP Conference proceedings (2013). (Accepted).*

6. **Positron annihilation studies on modified 9Cr-1Mo steel**
***S. Hari Babu**, R. Rajaraman, G. Amarendra. Proceedings of the 54th DAE Solid State Physics Symposium, **54**, 643 (2009).*

7. **Positron annihilation studies of Eurofer-97 steels.**
***S. Hari Babu** et.al.*
(manuscript under preparation)

8. **Positron annihilation studies of isothermally treated Fe-9Cr alloy.**
***S. Hari Babu** et.al.*
(manuscript under preparation)

9. **On the nature of Cr segregation in Fe-Cr alloys: A positron annihilation study.**
***S. Hari Babu** et.al.*
(manuscript under preparation)

Not included in Thesis

1. ***Positron lifetime studies of CaSO4:Dy thermoluminescence phospors***
   *O. Annalakshmi, Varghese Anto Chirayath, **S. Hari Babu**, M. T. Jose and G. Amarendra.*
   Proceedings of ICPA-15, SINP, Kolkata. Physica Status Solidi C 6, 2516-2518(2009).

2. **Annealing Effects in Eurofer-97 Steel as Studied by Mossbauer Spectroscopy**
   *L. Herojit singh, **S. Hari Babu**, R. Govindaraj, G. Amarendra, C.S. Sundar*
   *AIP Conf. Proc. **1447**, 1321 (2012).*

Working on an interdisciplinary problem is like dealing with mother and a new wife. Apprehensions of relative importance dominate mutual cooperation.

I hope, I have negotiated to the satisfactory of both to be qualified as Doctor. Failing which should at least guarantee me a philosopher tag according to Socrates.